ISSN 1000-9620

LIBRARY

Marine Science Bulletin

Volume 2 • Number 2 2000

LIBRARY
Pacific Islands Fisheries Science Center
NOAA Fisheries
Honolulu, Hawai'i

ISSN 1000-9620
02>
9 771000 962001

NATIONAL MARINE DATA AND
INFORMATION SERVICE OF CHINA

ENCE BULLETIN

Vol.2 No.2 October 2000

CONTENTS

The Relationships Between Magnetic Susceptibility and Sedimentary Characteristics of Caofeidian Sand Bar-lagoon System in the Bohai Sea
……*Ke Xiankun* (柯贤坤) et al. (1)

The Scattering Polarimetric Response Contrast Between Wind-generated Rough Sea Surfaces
……*Dong Qing* (董 庆) et al. (14)

Analysis on Spatial and Temporal Processes of Beach Profile Variations
……*Chen Zishen* (陈子燊) (21)

Distribution of Annual Rates of Sea Level and Variation of Long-Period Constituents in China
……*Zheng Wenzhen* (郑文振) (30)

Determination and Analysis of Oceanic Heat Flux Under Sea Ice Cover in the Liaodong Bay
……*Ji Shunying* (季顺迎) et al. (41)

Study on the Genesis and Occurrence of Great Earthquakes and Their Prediction
……*Zheng Wenzhen* (郑文振) (49)

Analysis of Climate and Sea Ice Characteristic for the Bohai Sea in 1998/1999
……*Meng Shang* (孟 上) et al. (56)

Scouring and Accretion Characteristics and Their Causes in the Qiqu Archipelago Over the Past Century
……*Chen Shenliang* (陈沈良) (66)

Chemical Oceanography of Nutrient Elements in the Bohai Sea, Yellow Sea and East China Sea
…… *Liu Sumei* (刘素美) et al. (76)

Regional Geologic Tectonics of the Nansha Sea Area
……*Jin Qinghuan* (金庆焕) et al. (86)

The Relationships Between Magnetic Susceptibility and Sedimentary Characteristics of Caofeidian Sand Bar-lagoon System in the Bohai Sea

LIBRARY
APR 23 2002
National Atmospheric
U.S. Dept.

Ke Xiankun (柯贤坤)[1] Jia Yulian (贾玉连)[2] Zhou Lufu (周旅复)[1]
Li Zhanhai (李占海)[1] Wang Aijun (王爱军)[1]
(*1 E & R Division of Physical Geography, Department of Urban & Resources Science, Nanjing University, Nanjing 210093*)
(*2 Nanjing Institute of Geography & Limnology, CAS, Nanjing 210008*)

Abstract Based upon a field sampling campaign in the Caofeidian sand bar-lagoon system off the west coast of the Bohai Sea in the winter of 1996, 173 samples were collected, and subsequently analyzed for grain size, magnetic susceptibility and heavy mineral contents. The study shows that the complex sedimentary system can be divided into 4 facies, i.e., deep water area, sand bar, tidal inlet and tidal flats, each with characteristic sediment types and magnetic susceptibility levels. The study also revealed the relationships between the mean grain diameters and magnetic susceptibilities, and between various magnetic susceptibility indices, and found that the main source of the magnetic susceptibility of the sediments is the heavy metal minerals. It has been shown that the magnetic susceptibility is a powerful tool for the coastal sand bar-lagoon system in terms of classification of sedimentary facies and reconstruction of palaeosedimentary environments.

Keywords Caofeidian; sand bar-lagoon system; grain size; magnetic susceptibility; heavy metal minerals

Introduction

Since the foundation of the environmental magnetism in the 1970s (Thompson, 1975), magnetic susceptibility has become a very important environmental index and been widely applied in the various environmental studies, such as loess, lake and tidal flats (Thompson & Oldfield, 1986; Kukla et al., 1988; Zhang et al., 1991; Liu et al., 1990; 1993; Wu, 1993; Wang et al., 1996). The measurement of the index is sensitive and accurate, fast and easy, and does no damage to samples. Many studies have shown that for clastic sediments the main minerals controlling the magnetic susceptibility are magnetite and hematite (Thompson & Oldfield, 1986). The magnetic susceptibility is closely related to grain size, and can indicate sources, dynamics and subsequent changes of the sedimentary environments (Wang et al., 1996). For the marine environment, there are studies on the magnetic susceptibility of the deep-sea sediments (Johnson et al., 1975). However, there are very few reports on the application of the magnetic susceptibility in the sandy coastal environment, such as sand bar-lagoon system. The

objectives of the present study are to introduce the index to the coastal environment, and to explore the relationships among the magnetic susceptibility, grain size, and mineralogy.

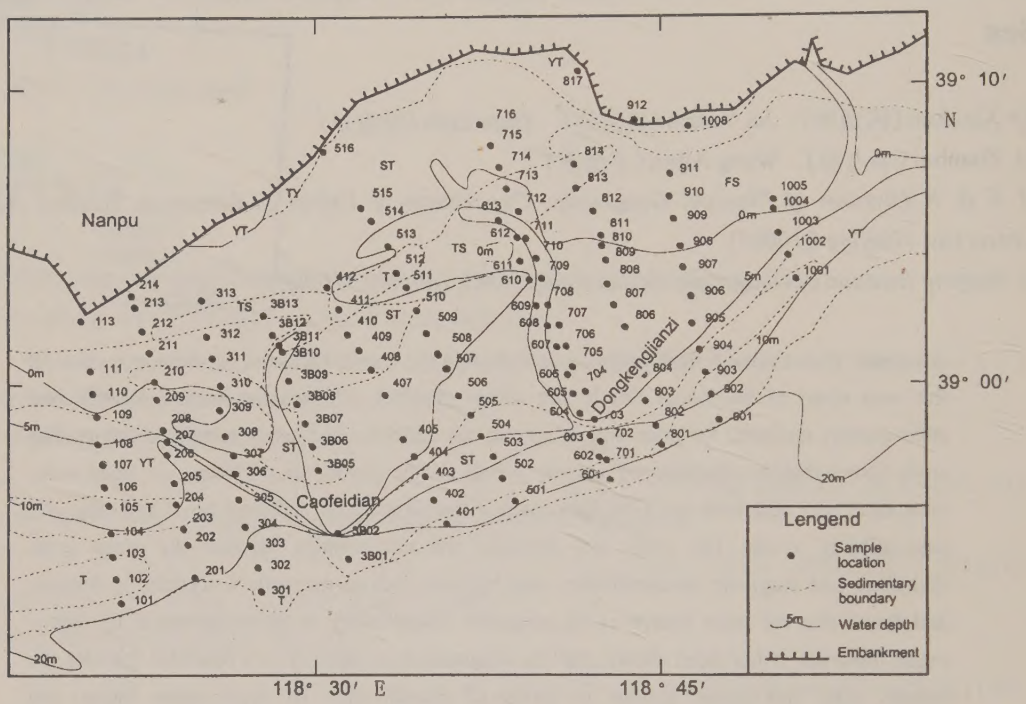

Fig. 1 Geomorphology and sediment distribution of the Caofeidian sand bar-lagoon system off the west coast of the Bohai Sea.

1 Regional Settings

The Caofeidian sand bar-lagoon is located in Hebei Province, northwest of the Bohai Sea. With a total area of 750 km^2, it is one of the largest sand bar-lagoon systems along the Bohai coastline (Fig. 1). It was built by the old Luanhe River during the middle Holocene when the Luanhe R. empitied into the Bohai Sea via Suhe R. and Xiaoqinghe R. (Gao et al., 1980; 1981; Li et al., 1982; Xu, 1988; Zhao et al., 1991; Liu, 1994; Ke, 1997).

Therefore, the Caofeidian sand bar-lagoon system is developed on the abandoned delta of the Luanhe River, and constituted by geomorphologic and sedimentary units, such as tidal flats, beach, lagoon and sand bar (Ke, 1997; Jia 1998; Jia et al., 1996; 2000; Wang, 1999; Wang et al., 1999). The lagoon is 64 km^2, with water depth of less than 5 m for most of the area, and near 10 m at nearby tidal inlets in the northwest of the area (Fig. 1). The tide over the region is rather complicated: irregular semi -diurnal tides in the northwest area, and near regular semi-diurnal tides near Nanpu. It is a typical micro -tidal coast where the mean tidal range is less than 2 m (Xu, 1988; Ke, 1997).

2 Methods

Samples were collected along 11 profiles during the period of November-December 1996, with an interval of about 1250 m between the two neighboring samples along the same profile line (Fig. 1). On the Caofeidian sand bar, samples were taken on the seaward beach along MHW line. In total, 173 samples were collected including 144 drag samples underwater and 29 spade samples on the Caofeidian sand bar. The positioning of the sample locations is achieved by GPS Model 2108 with a maximum error <100 m.

Grain size analyses are undertaken on LDY-1 System for grain size <32 μ m, with a grain size interval of 1 φ, and the smallest grade of 10 φ (mm unit of grain diameter (d) and phi unit of grain diameter (φ) have the relation of $d=2^{-\phi}$). Mechanic sieving is undertaken for grains >32 μ m. Grain size parameters including mean grain diameter (D_ϕ), and sorting (σ) are calculated following the Handbook of Oceanographic Investigation issued by SOA (1975).

A total of 126 underwater samples and 7 beach samples are undergoing measurement of magnetic susceptibility. Samples are dried under the temperature of 45 ℃ in an oven, and then grounded and mixed. Prepared samples are fed into a cubic box with a side length of 2 cm, pressed and sealed with tape . The apparatus used in measuring the magnetic susceptibility is the MS2 (Bartington, UK). Heavy minerals are selected from sediment of 2—4 φ from 50g sample using heavy liquid $CHBr_3$ (density 2.89 gml^{-1})

The indice used in the present study is Magnetic Susceptibility (χ), which represents the ratio of magnetic intensity to magnetic field intensity when the sample is exposed to the natural magnetic field. For the natural clastic sediments, their χ values are mainly controlled by their type, concentration, and grain size of the magnetic components. In practice, Low Frequency Magnetic Susceptibility (χ_{LF}) and High Frequency Magnetic Susceptibility (χ_{HF}) are measured, and Frequency Dependent Magnetic Susceptibility (χ_{fd}) is defined as :

$$\chi_{fd} = (\chi_{LF} - \chi_{HF}) / \chi_{LF} \quad (1)$$

In terms of physics, χ_{fd} is a parameter indicating the existence of magnetic minerals with the changes of grain size from stable single-domain (0.02—0.03 μ m) to super paramagnetic (<0.05 μ m), and has been extensively used in the loess studies (Yu, 1987; Liu et al., 1990; An & Ma, 1991; Liu et al., 1993).

For the Caofeidian sand bar-lagoon system, its sediment sources are mainly the old Luanhe R. (Xu, 1988). Therefore, Standard (low frequency) Magnetic Susceptibility of a given sample (χ_s (i)) is defined as the standardized mean of χ_{LF}(i) taking the region as a completed system. Its value is calculated by the flowing procedures. Let $x_i(\times 10^{-8} m^3 kg^{-1})$, $y_i(\times 10^{-8} m^3 kg^{-1})$, $z_i(\times 10^{-8} m^3 kg^{-1})$ stand for the magnetic susceptibility of sand (<4 φ), silt (4—8 φ) and clay (>8 φ) for sample i, respectively. According to the percentage of sand (S_i), silt (T_i) and clay (C_i) in, and χ_{LF}(i) of, each sample, any combination of the three samples (i, j and k) from the existing sample pool can form an equation group as shown (2), (3), and (4):

$$\chi_{LF}(i) = x_1S_i + y_1T_i + z_1C_i \quad (2)$$

$$\chi_{LF}(j) = x_1S_j + y_1T_j + z_1C_j \quad (3)$$

$$\chi_{LF}(k) = x_1S_k + y_1T_k + z_1C_k \quad (4)$$

By solving a series of equation groups, we can have the series of (x_1,y_1,z_1), (x_2,y_2,z_2), (x_3,y_3,z_3)...(x_n, y_n,z_n), where $n = (133\times32\times32)/(3\times2\times1)=378906$. Then, the mean values of magnetic susceptibility of sand (x_0), silt (y_0) and clay (z_0) of the region can be obtained by equations (5), (6) and (7):

$$nx_0 = x_1+x_2+x_3 \quad (5)$$

$$ny_0 = y_1+y_2+y_3 \quad (6)$$

$$nz_0 = z_1+z_2+z_3 \quad (7)$$

Based upon the calculation above, the values of x_0, y_0, and z_0 of the Caofeidian sand bar-lagoon system are 1.010×10^{-8} m^3kg^{-1}, 0.781×10^{-8} m^3kg^{-1} and 1.005×10^{-8} m^3kg^{-1}, respectively. Therefore, $\chi_s(i)$ can be obtained by formula (8)

$$\chi_s(i) = x_0S_i + y_0T_i + z_0C_i \quad (8)$$

Another index used in the present study is the Differentiability of Magnetic Susceptibility (D_χ (i)), which represents the difference between χ_{LF} (i) and χ_s (i) as formula (9) shows:

$$D_\chi(i) = (\chi_{LF}(i) - \chi_s(i))/\chi_s(i) \quad (9)$$

In terms of physics, $D_\chi(i)$ is a parameter which can indicate the sources and dynamic conditions for a sample after it enters a sedimentary environment. High D_χ normally implies high energy condition and active rebuilt, sorting processes while low D_χ is normally related with low energy and weak transportation.

3 Results

3.1 Grain size, sediment types and facies

Most D_ϕ over the region is between 1 ϕ and 8 ϕ, and σ between 0.25 and 3.0 (Fig. 2). The sediments of the sand bar area are mostly fine sands (D_ϕ=1—2.5 ϕ) and best sorted (σ =0.25—0.75). Tidal inlet sediments are of the same grain size similar to that of the sand bar, but not as well-sorted as the sand bar. The grain size distribution of the tidal flats sediments is rather spread, with D_ϕ=3—7 ϕ. With mean grain diameter ranging between 4 ϕ and 8 ϕ, the deep water area is of the finest and worst sorted sediment over the region. Therefore, on the whole, from sand bar to tidal inlet, tidal flats, and deep water, with the increase of D_ϕ (mean grain diameters in mm decrease), the sorting becomes worse and worse; the pattern coincides with the changes from high energy in the sand bar to the lower energy of the deep water (Fig. 2). The linear regression analysis for 171 samples shows a very good correlation between σ and D_ϕ as shown below:

$$\sigma = 0.2871D_\phi + 0.0264 \ (r=0.845, n=171) \quad (10)$$

Three sedimentary facies can be identified from the deep water to sand bar, lagoon and coastal high water line: shallow water marine facies, sand bar facies and tidal flat facies. Shallow marine facies is located in the area deeper than 10—20 m, with the finest sediments dominated by silty clay (TY) and clayey silt (YT). The sand bar facies is composed of the coarsest sediments of fine sand (FS) and

medium sand (MS). The tidal flat sediments landward of the sand bar facies become fine material again, which is dominated by silt (T) and silty sand (TS) (Fig. 1 & Fig 2). On the whole, from the sea to the land, the grain sizes of the sediments over the region change in the trend of fine-coarse-fine.

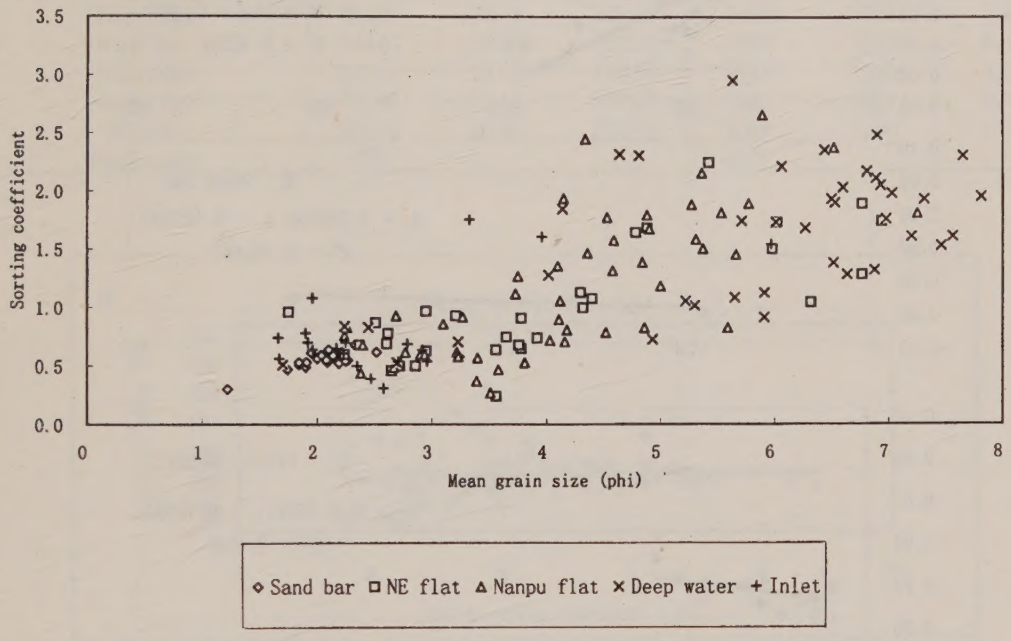

Fig. 2. The relationships between mean grain size (D_Φ) and sorting coefficient (σ) of the sediments in various sub—environments of the Caofeidian sand bar—lagoon system

On the basis of the analysis of sediment types, together with characteristics of marine geomorphology, the study area can be divided into four sub-geomorphologic and/or sedimentary units: deep water (water depth deeper than 5 m), tidal flats (shallow areas with water depth <5 m), sand bar (Caofeidian sand bar), and tidal inlet (the inlet and its adjacent areas).

3.2 The relationships between χ_{LF} and χ_{fd}

Most χ_{LF} of the region ranges between 40×10^{-8} m^3kg^{-1} and 180×10^{-8} m^3kg^{-1}, with a mean of 93.31×10^{-8} m^3kg^{-1} (Fig. 3 and Table 1). Almost all χ_{fd} are positive, with a regional mean of 0.03, and indicate $\chi_{LF}>\chi_{HF}$ overall. For different geomorphologic units, χ_{LF} and χ_{fd} exhibit different patterns of relationships (Fig. 3).

For the deep water area (Fig. 3A), the mean χ_{LF} and χ_{fd} are 96.84×10^{-8} m^3kg^{-1} and 0.05, respectively (Table 1), and of a good linear relationship with r=-0.65 (n=34). They vary between73×10^{-8}—188×10^{-8} m^3kg^{-1}.and 0.01—0.08. With a mean of 0.05, the χ_{fd} of the unit is the highest of the region; and implies a large difference between χ_{LF} and χ_{HF}.

For the sand bar area (Fig. 3B), χ_{LF} is the highest and χ_{fd} the lowest compared to those of other units. They are also of a good positive linear relationship with r=0.676 (n=7). Mean χ_{LH} and χ_{fd} of the sub-environment are 204.61×10^{-8} m^3kg^{-1} and 0.005, respectively (Table 1).

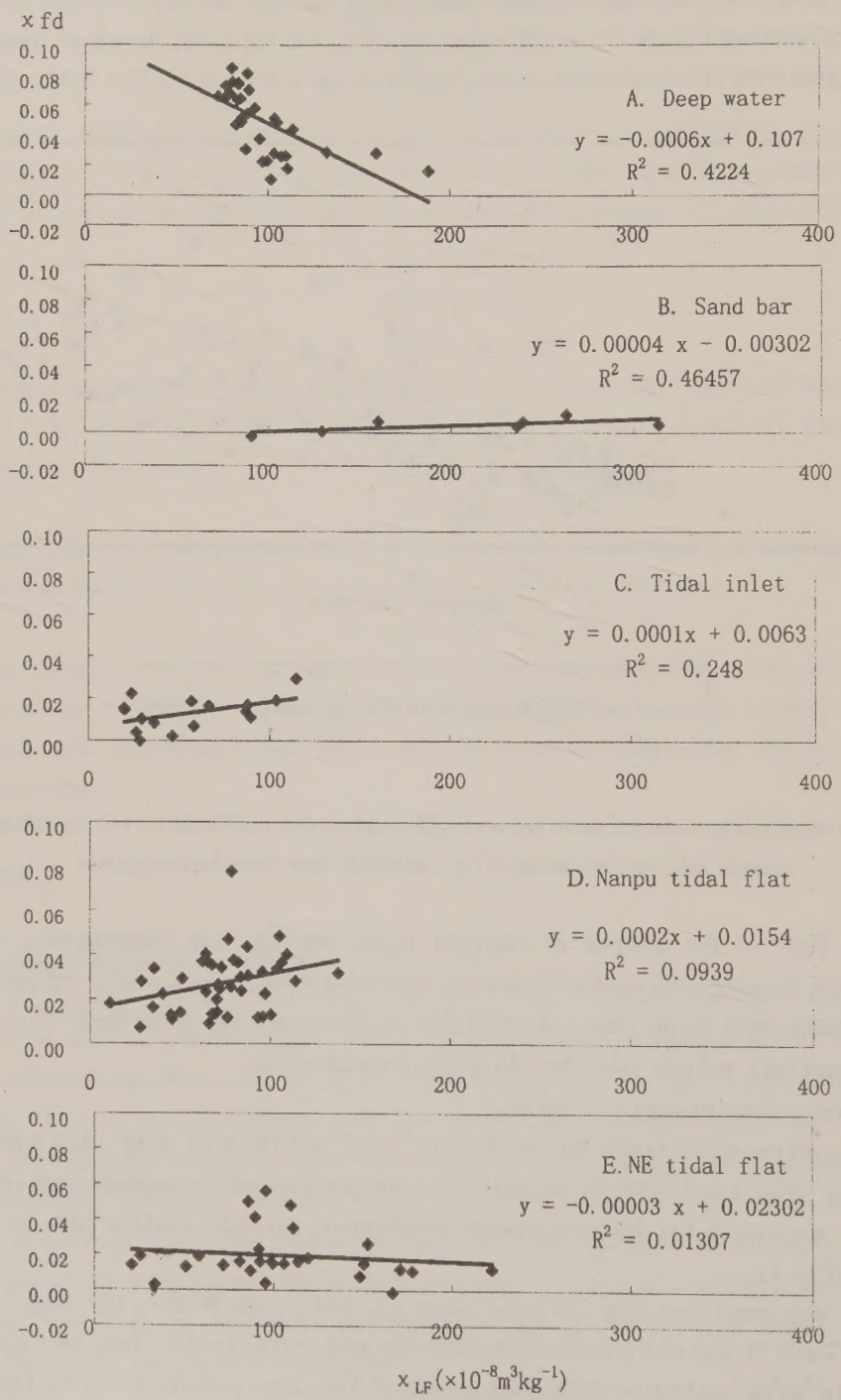

Fig. 3 The relationships between Magnetic (low frequency) Susceptibility (χ_{LF}) and Frequency Dependent Magnetic Susceptibility (χ_{fd}) of the sediments in various sub-environments of the Caofeidian sand bar-lagoon system: (A) Deep water, (B) Sand bar, (C) Tidal inlet, (D) Nanpu tidal flat, and (E) NE tidal flat.

Table 1 Mean, min. and max. values of magnetic susceptibility parameters in different sub-sedimentary environments of the Caofeidian sand bar-lagoon system.

Sub-environment	χ_{LF} ($\times 10^{-8} m^3 kg^{-1}$)			χ_{fd}		
	Mean	Min	Max	Mean	Min.	Max.
Deep water	96.84	72.90	188.40	0.05	0.01	0.08
Sand bar	204.61	90.80	313.20	0.005	0.00	0.01
Tidal inlet	55.92	19.70	114.90	0.01	0.00	0.03
Nanpu flat	73.36	11.10	138.00	0.03	0.01	0.08
NE flat	104.42	20.90	222.30	0.02	0.00	0.06
Total mean	93.31			0.03		

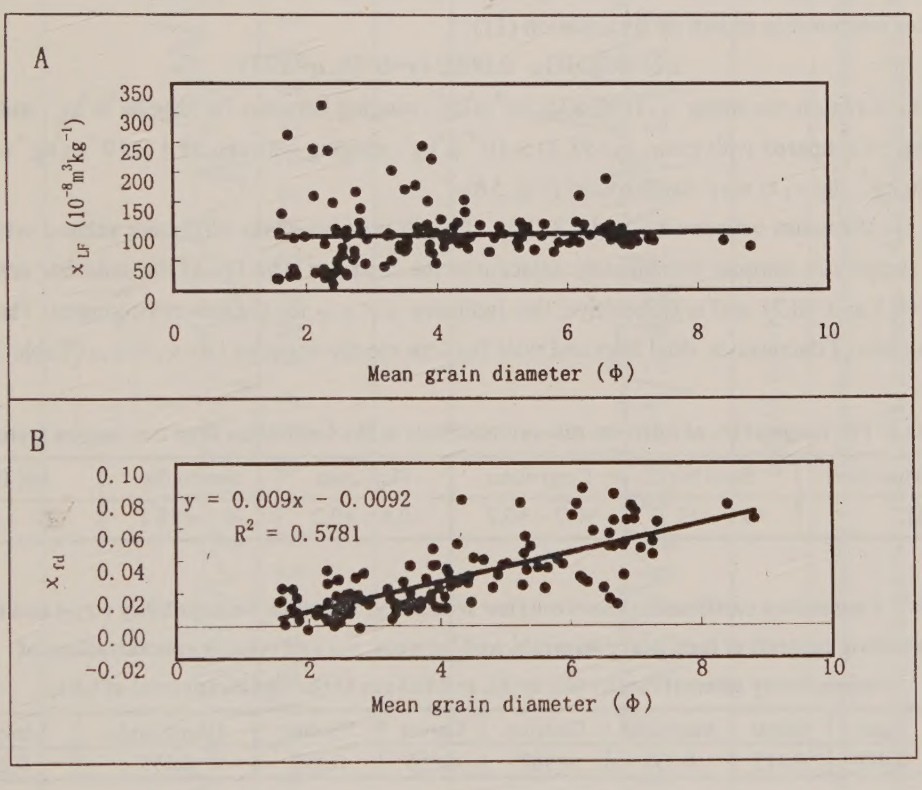

Fig. 4 The relationships between mean grain size (D_Φ) and magnetic susceptibility of the Caofeidian sand bar-lagoon system: (A) D_Φ and χ_{LF}, and (B) D_Φ and χ_{fd}.

The tidal inlet area (Fig. 3C) is of small χ_{LF} and χ_{fd}, which range between 20×10^{-8}—115×10^{-8} $m^3 kg^{-1}$ and 0—0.03, respectively, and are of a linear relationship with r=0.498 (n=16). Overall, with a mean of 55.92×10^{-8} m^3kg^{-1}, the χ_{LF} of the unit is the smallest compared to those of other units in the region (Table 1).

For the tidal flat area, χ_{LF} and χ_{fd} are rather scattered within the triangle area defined by the points of (0, 0), (79, 0.08), and (220, 0.01), and of low correlation (Fig. 3D and 3E). Mean χ_{LH} and χ_{fd} of the sub-environment are 73.36—104.42×10^{-8} m^3kg^{-1} and 0.02—0.03, respectively (Table 1).

3.3 Mean grain size (D_ϕ) and magnetic susceptibility

Over the region, χ_{LF} fluctuates around the line of $\chi_{LF}=93\times10^{-8}$ m^3kg^{-1}. With the increase of D_ϕ (decrease in mean grain diameter) from 2 ϕ to 9 ϕ, the amplitude decreases gradually. Therefore, (χ_{LF}, D_ϕ) points are scattered within the area of a horizontal trumpet opening towards the coarse grain size side (Fig. 4A). In other words, χ_{LF} converges at $\chi_{LF}=93\times10^{-8}$ m^3kg^{-1} with the increase of D_ϕ from 2 ϕ to 9 ϕ. Such a pattern may be due to the presence of one magnetic peak at 3—6 ϕ (Thompson & Oldfield, 1986), and/or measurement error caused by uneven mixing of sand particles.

The study also reveals that, on the regional scale, coarse sediments (small D_ϕ), such as those in the sand bar, are of low χ_{fd}, and fine sediments (large D_ϕ) such as those in the deep water and tidal flats units are of high χ_{fd}. Therefore, χ_{fd} increase with the increases of D_ϕ(Fig. 4B), and they have good linear relationship shown as by equation (11):

$$\chi_{fd}=0.009D_\phi \ 0.0092 \ (r=0.76, n=173) \qquad (11)$$

Over the region, the mean χ_s is $92.83\times10^{-8}m^3kg^{-1}$, ranging between $78.52\times10^{-8}m^3kg^{-1}$ and $101.00\times10^{-8}m^3kg^{-1}$. Compared with mean χ_{LF} 93.31×10^{-8} m^3kg^{-1}, ranging between 11.1×10^{-8} m^3kg^{-1} and $313.20\times10^{-8}m^3kg^{-1}$, the χ_s is very standardized (Fig. 5A)

The D_χ fluctuates between 2.1 and 0.8 (Fig. 5B). All positive peaks of D_χ are related with either sand bar samples or samples immediately adjacent to the sand bar. The D_χ of the sand bar area range between +0.5 and +0.21 and is all positive; this indicates $\chi_s<\chi_{LF}$ for the sub-environment. The D_χ of other sub-units of deep water, tidal inlet and tidal flats are mostly negative i.e. $\chi_s>\chi_{LF}$ (Table 2).

Table 2 The range of D_χ of different sub-environments in the Caofeidian sand bar-lagoon system.

Sub-environment	Sand bar	Deep water	Tidal inlet	Nanpu flat	NE flat
D_χ	+0.5 ~ +2.1	-0.2 ~ +0.2	-0.8 ~ +0.2	-0.7 ~ +0.1	-0.1 ~ +1.4

Table 3 Correlation coefficient (r) between (low frequency) Magnetic Susceptibility (χ_{LF}) and the absolute contents of total heavy minerals, and between χ_{LF} and relative concentrations of various heavy mineral species (for n=30, r>0.463 are of the significant level of 0.01)

	Total	Metal	Magnetite	Ilmenite	Garnet	Epidote	Hornblende	Limonite
R	0.478	0.613	0.731	0.567	0.455	0.432	0.405	0.238

3.4 Heavy minerals and magnetic susceptibility

The dominant heavy mineral species of the region are hornblende, garnet, amphibole, magnetite, epidote, limonite and ilmenite, with secondly minerals of zirconite, leucoxene, tourmaline and agustite, and trace minerals of tremolite, rutile, titanite, diopsite, aedelforsite etc. (Table 4); this composition is similar to that of the modern Luanhe R. sediments (Xu, 1988). Heavy mineral content varies in different sedimentary environments within the Caofeidian sand bar-lagoon system, with the highest content at the tip of Caofeidian sand bar (3—8.5%), medium content in the sub-tidal area (5.74%) and the lowest content within the lagoon area (0.09—2.94%).

Magnetic susceptibility is closely related to the contents of magnetite, heavy metal minerals (sum

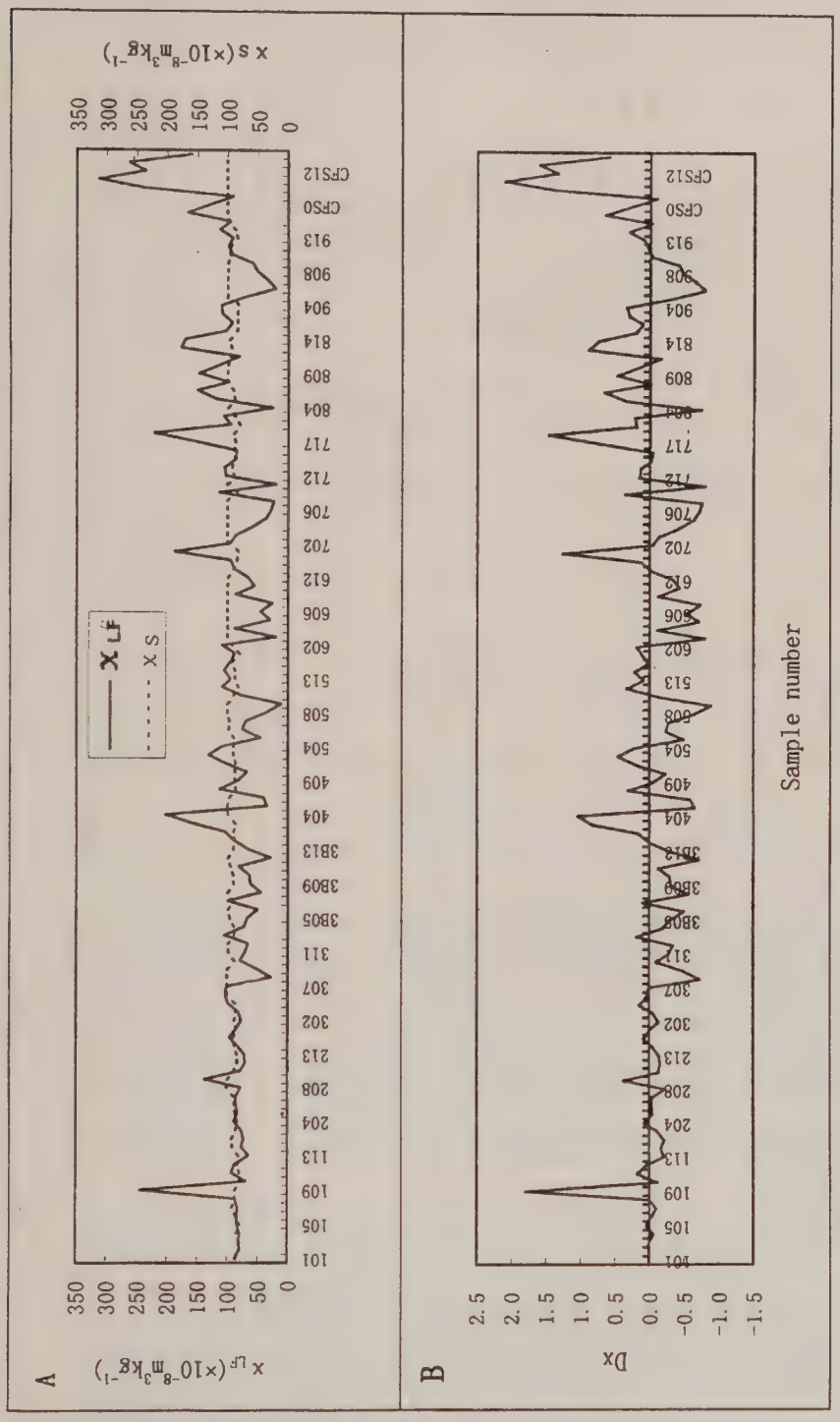

Fig. 5 Magnetic (low frequency) Susceptibility (χ LF), Standard (low frequency) Magnetic Susceptibility (χ s) and Differentiability of Magnetic Susceptibility (Dχ) of the sediments in the Caofeidian sand bar-lagoon system:

(A) χ LF and χ s, and (B) Dχ ,of all samples.

Table 4 Total heavy mineral content (%) ralative to the total sample weight and concentrations of different heavy mineral species (%) relative to the total heavy mineral weight

ample no.	Total	Magnetite	Limonite	Ilmenite	Pyrite	Epidote	Garnet	Hornblende	Amphibole	Zirconite	Leucoxene	Tourmaline	Agustite	Diopsite	Rutile	Titanite	Tremolite	Aedelforsit
307	3.09	16.52	0.76	3.24	Trace	9.78	12.3	51.82	0.39	1.94	3.24	0.21	1.00	-	-	0.21	0.07	-
3B08	2.41	2.48	0.83	8.49	Trace	22.78	14.08	35.20	1.24	2.90	8.49	0.39	5.59	-	-	2.90	-	Trace
3B13	0.37	2.45	5.45	2.59	Trace	20.47	4.16	58.93	1.63	0.27	2.59	0.07	1.23	-	0.09	-	-	-
404	4.48	2.45	0.89	3.79	Trace	20.08	13.39	43.50	0.89	2.68	3.79	0.09	1.78	-	Trace	0.45	0.09	Trace
501	0.14	12.21	3.67	3.22	2.54	3.73	18.19	43.03	9.84	0.98	3.22	-	-	Trace	Trace	Trace	Trace	-
503	1.04	0.45	-	3.50	0.10	28.78	17.27	39.81	0.08	0.43	3.50	0.51	0.57	Trace	0.03	0.39	0.09	-
505	1.36	4.48	2.30	0.90	0.38	3.80	18.07	54.83	5.74	2.73	0.90	1.32	-	Trace	trace	Trace	Trace	Trace
508	1.25	1.87	-	4.41	0.07	28.12	22.88	23.27	1.37	1.28	4.41	1.14	0.76	0.39	Trace	-	-	-
510	0.95	2.88	1.98	4.31	0.02	4.00	32.52	40.31	7.15	1.00	4.31	-	-	Trace	-	Trace	Trace	Trace
511	0.91	4.40	2.45	1.99	0.06	4.93	32.22	36.52	8.55	1.65	1.99	-	-	Trace	trace	Trace	Trace	Trace
512	0.09	35.14	0.40	2.30	0.60	2.21	34.85	7.00	8.22	1.26	2.30	0.70	-	Trace	trace	Trace	Trace	Trace
513	0.21	8.80	1.76	2.16	0.60	2.65	32.97	36.68	5.21	5.77	2.16	-	-	Trace	-	Trace	Trace	Trace
514	0.09	11.26	0.90	Trace	0.22	3.29	25.55	37.28	7.44	1.33	Trace	0.90	-	Trace	trace	Trace	-	Trace
515	0.82	5.20	2.33	1.97	0.03	3.36	24.92	50.43	5.79	3.00	1.97	-	-	Trace	-	Trace	Trace	Trace
5T1	0.50	6.84	6.78	2.00	0.02	11.91	31.45	41.28	15.34	0.98	2.00	1.29	-	Trace	Trace	Trace	Trace	Trace
605	1.29	3.27	1.79	2.05	Trace	33.46	13.62	37.35	0.78	1.17	2.05	0.78	2.33	Trace	Trace	0.33	-	Trace
609	0.77	0.06	6.68	2.54	Trace	33.13	12.94	40.90	0.00	-	2.54	0.84	0.84	Trace	-	1.42	0.14	-
705	0.95	1.27	3.17	6.50	Trace	15.33	10.04	58.14	0.85	0.85	6.50	1.27	1.69	-	Trace	1.69	-	-
803	1.37	2.92	5.26	2.77	Trace	20.46	16.07	37.68	0.06	2.63	2.77	0.18	2.12	0.18	0.06	1.39	-	-
806	0.4	5.65	2.83	2.90	0.06	13.84	7.53	61.63	0.06	0.63	2.90	Trace	0.50	0.06	-	0.31	-	-
809	2.76	1.48	Trace	0.85	Trace	22.14	10.14	41.53	1.58	0.80	0.85	0.16	1.20	-	-	0.16	0.24	-
813	1.71	15.24	3.52	Trace	Trace	4.1	8.50	59.46	0.85	1.41	Trace	0.90	0.85	-	-	0.23	Trace	-
906	0.99	3.22	2.92	4.97	Trace	27.18	11.57	49.32	1.91	-	4.97	Trace	Trace	-	-	Trace	-	-
1004	5.74	12.27	2.44	-	Trace	16.92	8.19	47.72	1.22	0.45	-	0.09	0.72	-	-	0.72	-	-
CFS1	0.73	1.65	-	5.90	Trace	29.49	0.96	43.21	0.09	0.96	5.90	-	trace	-	Trace	Trace	-	-
CFS1-1	12.24	5.59	1.72	0.69	Trace	20.27	17.57	35.55	1.72	1.76	0.69	1.47	2.53	Trace	0.19	1.55	-	-
CFS9-1	3.98	6.29	0.83	3.90	Trace	10.44	26.41	32.70	0.83	0.26	3.90	0.25	0.63	0.38	0.13	3.40	-	Trace
CFS12-1	5.64	13.74	0.76	1.95	Trace	16.85	17.74	26.61	1.15	3.81	1.95	0.18	0.89	-	0.11	1.69	-	-
CFS15-1	8.16	6.71	0.87	2.04	Trace	20.44	29.7	23.29	1.34	0.35	2.04	0.06	0.12	0.06	-	1.86	-	-
CFS16-1	2.41	2.48	0.83	8.49	Trace	22.78	14.08	35.20	1.24	2.90	8.49	0.39	5.59	-	0.21	2.90	-	Trace

of magnetite, ilmenite and limonite), and ilmenite, with r of 0.732, 0.613 and 0.567, respectively at the significant level of 0.01 (Table 3); this implies that the magnetic susceptibility of the samples of the region is mainly from the heavy metal minerals, particularly magnetite and ilmenite, of the region.

4 Discussion & Conclusions

Sediment distribution and sub-environments patterns of the Caofeidian sand bar-lagoon system are similar to that of modern Luanhe R. delta; this implies a close relationship between the study area and the old Luanhe R. delta. Although the Luanhe R. delta has moved out the Caofeidian region since the middle Holocene (Liu et al., 1989), the sedimentary patterns molded by the old river in the delta region are still kept until now.

D_ϕ of the region is of a general trend of sand bar<tidal inlet<tidal flats<deep water, and there is a good correlation between D_ϕ and σ ($\sigma = 0.2871 D_\phi + 0.0264$ ($r=0.845$, $n=171$)). Therefore, the coarse sediments are better sorted than the fine ones; this may be caused by the good wave-induced sorting process for the coarse sediments on the beach and sand bar in the form of bedload, and tidally-induced mixed suspended sediment transport for the fine sediments.

Table 5 Comparison of magnetic susceptibility levels ($\chi_{LF} \times 10^{-8} m^3 kg^{-1}$) in various environments

	Mean	Max.	Min.	Data sources
Loess (Beiyuan Profile)	-	100	10	Fang et al., 1996
Lakes core sediments:				
Qinghai Lake	6.33	17.10	4.87	Wu, 1993
Daihai Lake	96.15	120.54	83.69	
Taihu Lake	-	60	15	Yu et al., 1995
Jiangsu tidal flats:				Wang et al., 1996
Intertidal	-	273	14	
Supertidal	-	61	22	
Beach sand of China (10 samples)	69.7	362.12	0.12	Ke et al., 2000
Caofeidian sand bar~lagoon system:	93.31			The present study
Sand bar	204.61	313.2	90.8	
Deep water	96.84	188.4	72.9	
Tidal flat	88.89	222.3	11.1	
Tidal inlet	55.92	114.9	19.7	

Mean magnetic susceptibility (χ_{LF}) of the sand bar-lagoon system is $93.31 \times 10^{-8} m^3 kg^{-1}$, with different levels for different sub-environments in the order (from high to low) of sand bar ($204.61 \times 10^{-8} m^3 kg^{-1}$) > deep water area ($96.84 \times 10^{-8} m^3 kg^{-1}$) > tidal flat ($73.36 \times 10^{-8}$—$104.42 \times 10^{-8} m^3 kg^{-1}$) > tidal inlet ($55.92 \times 10^{-8} m^3 kg^{-1}$). The results of the present study are comparable with those published data in various sedimentary environments, particularly the tidal flat sediments and beach sands (Table 5). Therefore, in a dynamically matured coastal environment, the magnetic susceptibility of various sub-environments may be balanced at a certain level; this is useful for the reconstruction of palaeosedimentary environments using magnetic susceptibility.

Similarly, D_x values are in the order of sand bar (+0.5 to +2.1) > tidal flats (-0.7 to +1.4) > deep water (-02 to +0.2) > tidal inlet (-0.8 to +0.2). Different from the trend above, χ_{fd} is in the order of deep water (0.05) > tidal flats (0.02-0.03) > tidal inlet (0.01) > sand bar (0.005), with a regional mean of 0.03. Most χ_{fd} is greater than 0.0; this implies that $\chi_{LF} > \chi_{HF}$ is valid for the whole region.

χ_{LF} of the region is changeable, with larger fluctuating amplitude for smaller D_ϕ(coarser grain size). When $D_\phi > 4\,\phi$, χ_{LF} seems to be stabilized at around $93 \times 10^{-8} m^3 kg^{-1}$. χ_{fd} of the region displays a good correlation with D_ϕ (χ_{fd}=0.009D_ϕ 0.0092 (r=0.76, n=173)). These indicate that the coarse sediments of the region are changeable in χ_{LF} and of smaller χ_{fd} i.e. smaller difference between χ_{LF} and χ_{HF}, and the fine sediments are stable in χ_{LF} and of larger χ_{fd} i.e. larger difference between χ_{LF} and χ_{HF}. Therefore, for this particular marine environment, χ_{LF} is more meaningful for the fine sediments in the deep water area and χ_{fd} for the whole region. Besides, Differentiability of Magnetic Susceptibility (D_x) is another index which can be used to distinguish the sand bar as well as its adjacent environments (with D_x>0) from other sub-environments of deep water, tidal inlet and tidal flats (mostly with D_x<0).

The correlation between heavy minerals and magnetic susceptibility shows that the source of magnetic susceptibility of the sediments of the region is mainly the heavy metal minerals within the sediments, particularly the magnetite and ilmenite.

References

An, Z.S. and Ma, X.H., (1991) Preliminary study on environmental magnetism. In: Liu, D.S (ed.), Loess, Quaternary Geology and Global Changes (Vol. II). Beijing: Science Press, 143—151

Fang, X.M., Dai, X.R., Li, J.J., Cao, J.X., Guang, D.H., Hao, Y.P., Wang, J.L and Wang, J.M., (1996) Unexpectancy and unstability of the evolution of Asian monsoon: a case study on soil development in the Last Glacial Period. Science in China (Series D), 26(2):154—160

Gao, S.M., Li, Y.F., An, F.T. and Li, F.X., (1980) The formation of coastal sandy body and shoreline changes in the Luanhe River delta. Acta Oceanologica Sinica, 2(4):102—113

Gao, S.M., Xia, D.X., Wang, Y.J., Liu, F.S., Liu, C.F., (1981) Sedimentary model of the Holocene deltaic facies of the Luanhe River. Acta Geographica Sinica, 36(3):403—411

Jia, Y.L., (1998) Modern characteristics of sediments in the Caofeidian sand bar-lagoon system. Unpublished M. Sc. thesis, Department of Geography, Nanjing University, 70

Jia, Y.L., Ke, X.K., Xu, Y.H. and Wang, Yan, (1998) Sediment transport trends of the Caofeidian sand bar-lagoon system in the Bohai Sea. Marine Science, 3, 56—60

Jia, Y.L., Ke, X. K., Wang, Yan and Li, S.J., (2000) Sedimentary characteristic of Caofeidian sand bar-lagoon system. Marine Science Bulletin, 19(1): 41—50

Johson, H.P., Kinoshita, H., Merill, R.T., (1975) Rock magnetism and palaeomagnetism of some north Pacific deep sea sediments, Geo., Soc. Am. Bull., 86, 412—420

Ke, X.K., (1997) Research report on the dynamic geomorphology and sediment dynamics of the Caofeidian area of the Jingtang Port, Department of Geography, Nanjing University, 56

Ke, X.K., Li, Z.H., Zhou, L.F and Wang, A.J., (2000) The quality and radioactivity of the beach sands at the major seaside tourist resorts of China, 10

Kukla, G., Heller, F., Liu, X.N., Xu, T.C., Liu, T.S., An, Z.S., (1988) Pleistocene climates in China dated by

magnetic susceptibility. Geology, 16, 811—814

Li, C.X., Chen, G., Gao, M.N. and Zhuang, Z.Y., (1982) The development of sand bar-lagoon system. Marine Geology Research, 2(1):47—55

Liu, X.M., Liu, D.S., Heller, F. and Xu, T.C., (1990) Magnetic susceptibility of loess and changes of palaeoclimate. Quaternary Research, 1, 42—50

Liu, X.M., Liu, D.S. and Shao, J., (1993) Characteristics of magnetic minerals of loess in China. Quaternary Research, 3, 281—287

Liu, Y.X., Zhu, L.K. and Wang, L.H., (1994) Evolution and port construction at abondanded sand bar-lagoon coast of Luanhe R. delta. Acta Oceanologica Sinica, 16(5): 60—67

SOA (State Ocean Administration), (1975) Hand Book of Oceanographic Investigation (Vol. 4): Marine Geology Investigation. SOA, Beijing, 145

Thompson, R., (1975) Magnetic susceptibility of lake sediments. Limnology & Oceanography, 20(5): 687—698.

Thompson, R. and Olfield, F., (1986) Environmental magnetism. George Allen & Unwin.

Xu, S.B. (ed.), (1988) Coastal zone resources of Hebei Province (Vol. I & II). Shijiazhuang: Hebei Science & Technology Press

Yu, L.Z., (1987) Study on t. he quantitative analysis of sediment sources based upon the magnetic measurement, with the example of Rhode River drainage basin, Maryland, USA. Young Geographer, 3(3): 5—29

Yu, L.Z., Xu, Y., Xu, S.Y. and Zheng, C.S., (1995) Palaeoenvironmental implication of a magnetic measurements of sediment cores from the Taihu lake, east China. Journal of Lake Sciences, 7(2): 141—150

Wang, J., Liu, Z.S., Jiang, W.Y., Dong, L.X., Zhu, M.Z and Gao, F., (1996) The magnetic susceptibility and its relationships with grain size and mineralogy and palaeoenvironmental significance. Acta Geographica Sinica, 51(2): 155—163

Wang, Yan, (1999). Study on the Quaternary sedimentary environmental changes in the Caofeidian area. Unpublished M. Sc. thesis, Department of Geography, Nanjing University, 82

Wang, Yan, Ke, X.K., Jia, Y.L. and Zou. X.Q., (1999) Study on the coastal profile changes of the Caofeidian area in the Bohai Sea since 1983. Marine Science Bulletin, 18(1): 43—51

Wu, R.J., (1993) Magnetic susceptibility and frequency dependent susceptibility of lake sediments and their paleoclimatic implication: a case of recent sediments of Qinghai Lake and Daihai Lake. Journal of Lake Science, 5(2): 129—135

Zhao, S.L., Yang, G.F., Chang, S.X., Zhang, H.C., Huang, Q.F., (1978) Study on the marine straitigraphy and coastlines of the west coast of the Bohai Bay. Journal of Oceanology & Liminology, 9(1): 15—24

Zhang, S.F., Xiao, J.Y., Yu, L.Z. and Wu, Y.S., (1991) Mineral magnetic measurement of lake sediments and its environmental application. Scientia Geographica Sinica, 11(2): 182—193

The Scattering Polarimetric Response Contrast Between Wind-generated Rough Sea Surfaces

Dong Qing(董庆)[1,2] Guo Huadong（郭华东）[1] Wang Changlin（王长林）[1]

(*1 LARSIS, Institute of Remote Sensing Applications, Academia Sinica, Beijing* 100101)
(*2 Institute of Ocean Technology, State Oceanic Administration of China, Tianjin* 300111)

Abstract Polarimetry for SAR applications is an excellent technological method to extract more information about wind-generated rough sea surface according to the scattering mechanisms. With the ues of the scatter matrix, i.e. Mueller matrix, and Stokes vector operator, the paper describes a comparison between the polarimetric responses of two types of wind-generated sea surface offshore Baogang, Hainan Province. It gives representative results for the polarimetric response of backscattering electromagnetic field from the rough sea surface and the characteristics of Mueller matrices traces. The long wavelength sea surface and the short one can be determined by their polarimetric responses. The traces and determinant values of scattering matrices are related to the wind conditions. Some heuristic conclusions are given upon the results. And finally, it is suggested that more information of sea surface will be more directly correlated with radar scatter polarimetry.

Keywords ocean waves; backscattering; polarimetric response

Introduction

SIR-C/X-SAR has opened a new era of multiparameter synthetic aperture radar. More and more airborne and spaceborne SARs with variable incident look angles, multifrequency and multipolarization will be launched in more recent years. SIR-C/X-SAR provides simultaneously images at three microwave wavelengths, L-band quad-polarization, C- band quad-polarization and X-band with VV polarization. Obviously, polarization of radar electromagnetic wave is a very important factor of backscatter theory and application. Although radar polarimetry has been accepted as an indispensable tool, and convincing results have been obtained for some existing models and their geoscience applications, however, there still exists a large void in the utilization and handling of polarimetric information contained within multipolarization SAR data. Especially, the relationships between backscatter return from wind-generated ocean rough surface and the dependence of radar polarization have not been extensively studied by both oceanographers and microwave remote sensing researchers.

The utmost applications of radar remote sensing of ocean come down to quantitative derivation of some oceanographic parameters instead of simple interpretation of patterns on the SAR image itself

of ocean surface. Accordingly, theoretical models are needed necessarily. Since the 1950s, the electromagnetic backscattering model for rough ocean surface has been developed greatly. Basically, these models are extensive by the Rices theory. Only just differences are there on the ground of approximate approaches in solving the functions of these models. Among these models, the composite surface model[1,2] has been the standard method for computing the cross section for microwave backscattering from the ocean surface since Rices theory. Recently, this method has been used to estimate the mean Doppler spectra as well. But there exist some drawbacks of the composite model approach in the area of ocean applications. For example, the ocean wavelengths must be divided into the long wavelength part and the short part, i.e., the short waves are small compared to the microwave wavelength, vice versa. It is difficult sometimes to separate the two components from random sea surface. The Kirchhoff approximation does not yield the proper polarization sensitivity. Some authors mention the effect of polarization in the SAR imaging model of the sea surface[3~5, 10]. Unfortunately, the existing SAR models lack full consideration. More work is needed in modeling SAR image of moving rough sea surface.

Based on some backscatter theory, the present paper calculates and analyses the polarimetric signatures of two kinds of wind-generated rough sea surfaces by using of SIR-C/X-SAR data of South-China Sea. Some heuristic conclusions are drawn from the results.

1 The Pattern of SIR-C/X-SAR Image of Two Fetches

The image we used in the present paper was acquired during the mission of SIR-C/X-SAR in October 1994. It locates offshore Baogang harbor, Hainan Province, and the center of the image is 18° 18′ 25.3″ N and 109° 1′ 16.0″ E. Figure 1 shows the C-band VV intensity enhanced image. The area marked A is a fully developed sea and shown bright relatively. On the contrary, the non-fully developed sea marked B is dark. Generally, we consider that there should exist an atmospheric front between the two fetches.

2 The Contrasts of Polarimatric Signatures Between the Two Fetches

The complexity of obtaining meaningful ocean wave information from SAR images indicates that even a subtle change can result in completely different images for the same sea state and the identical SAR system parameters[6]. For oceanographic application of radar remote sensing, we prefer some quantitative derivation to qualitative interpreting SAR image itself. The theory that describes completely the SAR imaging mechanism of rough ocean wave rough surface is developing continually. We propose that the polarization of backscattering radar wave from ocean surface should be a very important factor aiming at developing this SAR imaging model on condition that the SAR systems development trends towards multi-frequency and multi-polarization. Our objective is to obtain some polarimatric signatures of different fetches using SIR-C/X-SAR polarization data (JPL 16- mode data).

2.1 Scattering matrix and polarization signatures

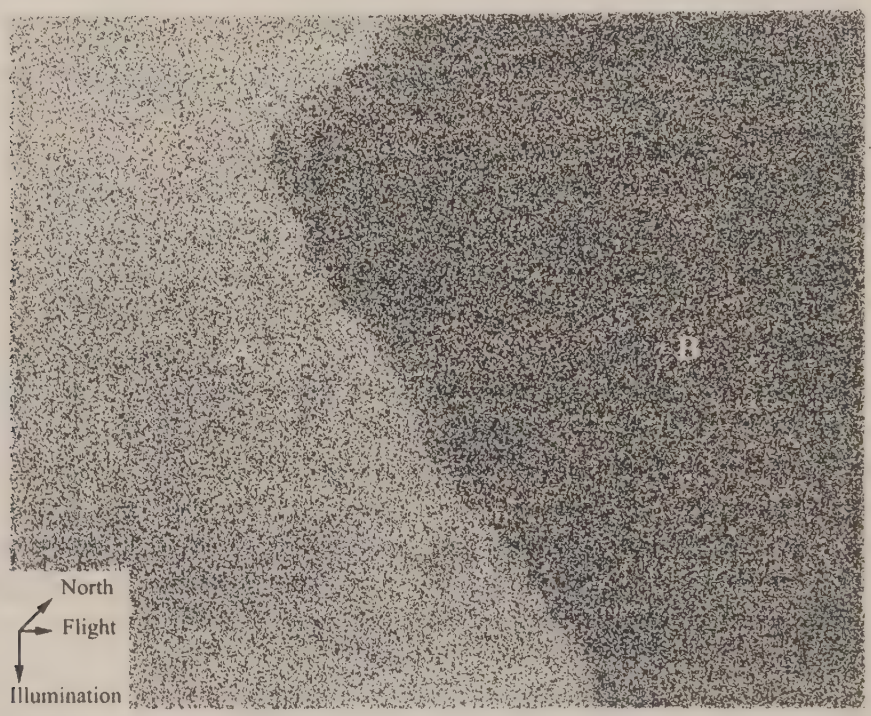

Fig.1 Gray enhanced image of C-band VV intensity offshore Baogang, Hainan Province
A: fully developed sea area, B: non-ully developed sea area

Polarimetric SAR data provides more abundant information of the moving ocean wave than the single polarization data. The 16- mode SIR-C data permits computation of the polarization scattering matrix of sea surface scatters, thus we can get full polarimetric signatures. The polarimetric scattering matrix describes completely the radar wave backscattering behaviors of ocean rough surface. Ulaby and Elachi[7] give the formula of the scattering coefficient σ^0_{rt} for a general transmitting and receiving antenna polarization as:

$$\sigma^0_{rt}(\psi_t, \tau_r; \psi_t, \tau_t) = \frac{4\pi}{A}(I_r \cdot R \cdot M \cdot I_t) \qquad (1)$$

where A is the illuminated area, I_t and I_r are transmitting and receiving Stokes vectors, respectively. And R rotates to convert the Stokes matrix into the modified Stokes scattering operator. It is a diagonal matrix given by:

$$\mathbf{R} = \begin{bmatrix} 1 & 0 & 0 & 0 \\ 0 & 1 & 0 & 0 \\ 0 & 0 & 0.5 & 0 \\ 0 & 0 & 0 & -0.5 \end{bmatrix} \qquad (2)$$

In formula (1), the Stokes vectors, I_t and I_r, are expressed in terms of the ellipicity τ and orientation

angles ψ :

$$I_r = \begin{pmatrix} 0.5(1+\cos 2\tau_r \cos 2\psi_r) \\ 0.5(1-\cos 2\tau_r \cos 2\psi_r) \\ \cos 2\tau_r \sin 2\psi_r \\ \sin 2\tau_r \end{pmatrix} \text{ and } I_r = \begin{pmatrix} 0.5(1+\cos 2\tau_t \cos 2\psi_t) \\ 0.5(1-\cos 2\tau_t \cos 2\psi_t) \\ \cos 2\tau_t \sin 2\psi_t \\ \sin 2\tau_t \end{pmatrix}$$

The subscripts, r and t, represent the received wave and transmitted wave, respectively. Scattering matrix M, Muller matrix named in some literatures, is given by[7, 8] :

$$\mathbf{M} = \begin{bmatrix} |S_{vv}|^2 & |S_{vh}|^2 & \mathrm{Re}(S_{vv}S_{vh}^*) & -\mathrm{Im}(S_{vv}S_{vh}^*) \\ |S_{hv}|^2 & |S_{hh}|^2 & \mathrm{Re}(S_{hv}S_{hh}^*) & -\mathrm{Im}(S_{hv}S_{hh}^*) \\ 2\,\mathrm{Re}(S_{vv}S_{hv}^*) & 2\,\mathrm{Re}(S_{vh}S_{hh}^*) & \mathrm{Re}(S_{vv}S_{hh}^* + S_{vh}S_{hv}^*) & -\mathrm{Im}(S_{vv}S_{hh}^* - S_{vh}S_{hv}^*) \\ 2\,\mathrm{Im}(S_{vv}S_{hv}^*) & 2\,\mathrm{Im}(S_{vv}S_{hv}^*) & \mathrm{Im}(S_{vv}S_{hh}^* + S_{vh}S_{hv}^*) & \mathrm{Re}(S_{vv}S_{hh}^* - S_{vh}S_{hv}^*) \end{bmatrix} \quad (3)$$

where, S_{qp} is radar wave intensity, and q、 $p = h$, $v$is known as horizontal polarization and vertical polarization, respectively. The symbol * denotes the complex conjugate operator. Matrix M relates to scattering vector with incident vector by formula (1). It describes the scattering process of interaction between radar wave and target, especially the moving ocean surface.

2.2 Polarimetric signatures of two fetches

The results of formula (1) calculation using SIR-C data are shown in Figure 2, where Figures 2a1 and 2a2 describe the signature for fetch A in Figure 1 while Figures 2b1 and 2b2 for fetch B. With these full polarimetric synthesis 3D-plots, one can see that the difference of the backscatter coefficients of the two different areas is within the value less than 5dB. But the polarimetric signatures are different significantly. In area A of Figure 1, polarimetric synthesis plots of both L- and C-band are not symmetric about the ellipicity angle, which shows that the wave crests are sinuous regularly in a fully developed sea area. The roughness of the sea area is dominantly controlled by the long wavelength and its distribution displays anisotropy with the wave crest. Accordingly, the backscattering coefficient depends upon the illumination direction of SAR system. By contraries, the L-band backscattering coefficient of the non-fully developed sea area B exhibits a very symmetric ellipicity angle, which shows that the most components of the sea surface waves are larger than 24cm, which is the L-band radar wave length. The roughness structure of ocean surface is isotropy with the crest of waves. But for C-band, which radar wavelength is 5.66cm, backscattering behavior occurs within optical scatter spectrum where the size of single scatter is larger than the radar wavelength. Thus, polarimetric synthesis plots of C-band are not symmetric extremely about the ellipicity angle. Also, the depolarization and multi-path effects by sea surface decrease the relation of the cross polarization. The results agree with the so-called full wave model prediction by Bahar[4,5]. But the latter model relies only on the spatial wave number and ignores multi-path effects by sea surface when separating large-scale scatters from small ones. Obviously, it is not fit for complex moving rough sea surfaces.

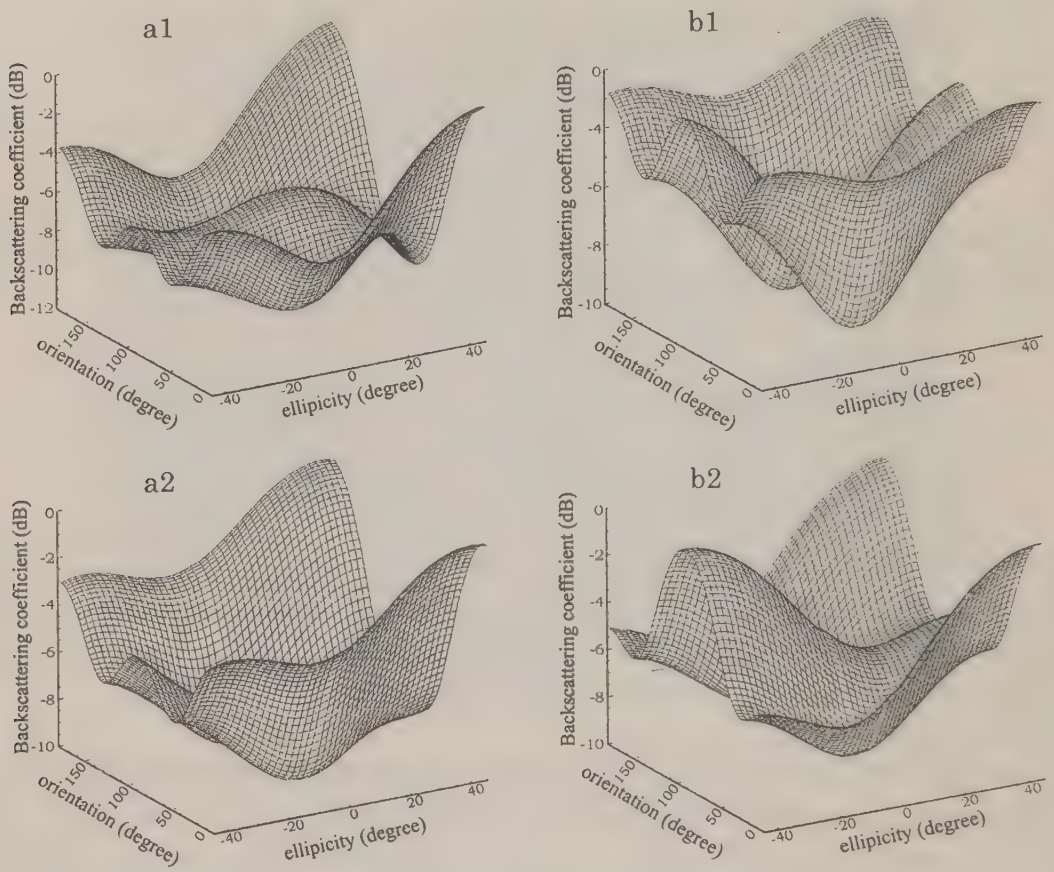

Fig 2 Backscatter coefficients respones

a1: L-band, a2: C-band of fully developed sea area

b1: L-band, b2: C-band of non-fully developed sea area

Meanwhile, we find that the vertically polarized backscattering coefficients are about 8dB greater than the horizontally polarized backscattering coefficients for both area A and area B, so that for oceanography applications the VV images are better than other polarized modes. Moreover, in the fully developed sea area, due to the larger amplitude of waves the backscatter difference between co-polarizations is decreased. Similarly, the cross-polarization difference is smaller in the same condition.

2.3 The trace values analysis of scatter matrix

The trace value is also a function of surface roughness. Figure 3 illustrates some characters of L- and C- band trace of scatter matrix of the fully developed sea area (A) and the non-fully developed area (B). One can see that trace values of L-band matrix are always greater than those of C-band for both area A and area B. Additionally, scatter matrix trace values of the fully developed sea area are always larger than those of the non-fully developed area. The peaks of the trace plots correspond to small-scale scatters.

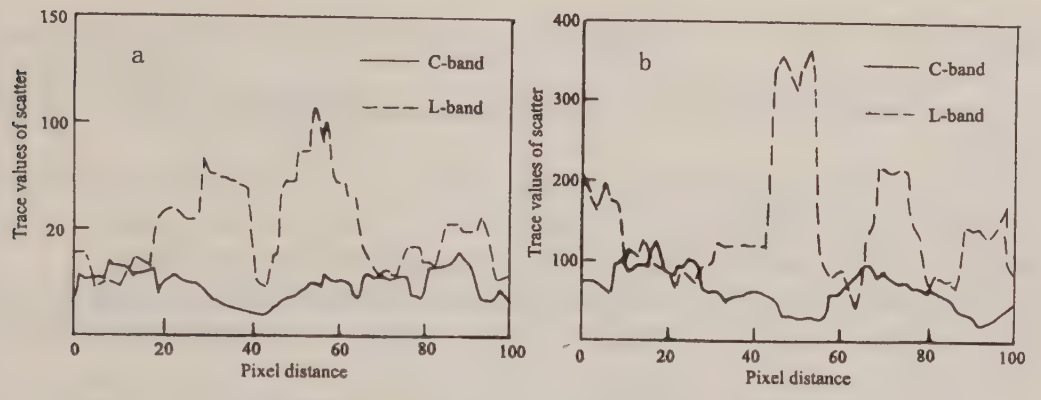

Fig.3 Scatter matrix trace values plots vs pixel distance
a: fully developed sea area b: non-fully developed sea area

3 Conclusion and Discussion

The process of sea surface backscattering is very complex due to the depolarization by the moving ocean waves. To analyze polarimetric SAR signatures is an effective approach to characterizing the polarization properties of microwave backscatters and is signifiacnt because polarimetric signatures utilize full amplitude and phase information from each actual SAR image resolution cell. Polarimetric and related polarimetric properties of microwave ocean backscatter have been analyzed for both the fully developed sea area and the non-fully sea area. Polarimetric responses of both areas are calculated using the scatter theory. The results suggest that the different polarization synthesis responses are sensitive to the wind regime. A combined interaction of radar wave backscattering and roughness components, i.e., large-scale and small-scale wavelengths, is proposed to model the SAR image mechanism of complex moving ocean surface with utility of polarimetric SAR data relating incidence, wind speed and wave propagation direction. To summarize, we have drawn some heuristic conclusions from the above results and analysis, which are: (1) the polarization responses may be used to determine the kinds of wind regime, (2) it is proposed that we separate so-called large-scale waves from sea surface by the polarization responses when the two-scale composite model is employed, (3) a full polarization backscattering model can be established by polarimetric responses, and (4) to determinate the optimum polarization of SAR system for oceanography applications.

We suggest that further research should be carried out together with some experiments. Then some *in situ* or laboratory measurements for oceanographic parameters will be analyzed with the present scatter theories.

References

1 Wright J W, (1968), A new model for sea clutter, IEEE Transactions on antennas and propagation, AP-16(2): 217—223

2 Valenzuela G R, (1978), Theories for the interaction of electromagnetic and oceanic waves -a review, Boundary Layer Meterology, 13: 61—85

3 Guo Huadong, (1999), Analysis of radar remote sensing imagery in China. Science Press, Beijing

4 Bahar E and Shi X, (1998a), The Scattering and depolarization of electromagnetic waves by random rough surfaces with different scales of roughness: new full wave solutions, Int. J. Remote Sensing, 19(11):2171—2185

5 Bahar E and Shi X, (1998b), The identification of sea swell using polarimetric radar, a new full wave approach, Int. J. Remote Sensing, 19(11): 2187—2209

6 Paris W V and Harald E K, (1995), Synthetic aperture radar imagery of ocean waves, in Oceanographic application of remote sensing, Ed. By Motoyoshi Ikeda, Frederic W. Dobson, CRC Press

7 Ulaby F T, Elachi C, (1990), Radar polarmetry for geoscience applications, Artech House

8 Ishimaru A, (1997), Wave propagation and scattering in random media, IEEE Press, New York

9 Gade M, Alpers W, Ermkov S A, Hü hnerfuss H., (1998), Wind-wave tank measurements of bound and freely propagating short gravity-capillary waves, Journal of Geophysical Research, 103(C10): 21697—21709

10 Boehmsdoff S, Essen H, Makaruschka R, (1997), Polarimetric multifrequency SAR measurements over sea at millimeterwave frequencies, SPIE, 3120: 336—345

11 Czyz Z H, Boerner W.-M., (1997), Scattering and cascading matrices of the lossless reciprocal polarimetric two-port in microwave versus millimeterwave and optical polarimetriy, SPIE, 3120: 373—384

Analysis on Spatial and Temporal Processes of Beach Profile Variations

Chen Zishen（陈子燊）
(*Institute of Estuarine and Coastal Research, Zhongshan University, Guangzhou 510275*)

Abstract Based on the repeatedly measured profile data in the middle section of the beach of the Shuidong Bay in west Guangdong, the main spatial processes of beach profiles and their temporal oscillations are analyzed with empirical orthogonal function and wavelet transform methods. The results show that the profile variations are mainly composed of three processes which account for 90% of the total variance of the original data: sub-tidal bar movement; berm progression and retrogression; and backshore erosions. Three main spatial processes indicate multi-scale oscillations in temporal and frequency domain, in which the variations of bar movements are mainly quasi-seasonal while the berm and backshore erosions exhibit the quasi-two month period. The main processes of profile changes are closely related to the typhoon actions.

Keywords beach profile; empirical eigenfunctions; wavelet analysis; profile processes and temporal oscillations

Introduction

The natural beach (referring to the sandy beach, the same below) is a dynamically sensitive zone where the land and the ocean interact and the beach variation processes are the result of the interactions between such dynamic factors as coastal wave, tide and wind, and the beach topography[1, 2] while the beach profile reflects to a certain degree the complicated processes——the major beach processes of the response system through its material composition, gradient and geomorphological structure. Some researchers have analysed the spatial and temporal variation characteristics of the beach profile by applying the decomposition method of empirical eigenfunctions for the beach profile, which is of quick convergence and being mutually orthogonal thus representing the independent beach variation processes. Therefore, the method can represent the main characteristics of the raw data field and objectively describe the topographic change and main time structure of the beach profile. It is an accurate way of predicting profile changes and, also provides a certain amount of mathematical tools for the comparison of different beach profile variation processes[3—8]. As a brand-new method of mathematical analysis evolving in the 1980s, the method of wavelet analysis is suitable for analysing the local characteristics of signals and therefore has been widely used in a number of research areas such as seismic data analysis, image processing, fractal and sampling as well as atmospheric and marine sciences[9—13]. Based on the repeatedly measured beach profile data in the field, this paper

analyses the major spatial characteristic patterns and their topographic implications with the empirical eigenfunction and then applies the wavelet tranform and energy spectrum analysis methods to their corresponding main temporal eigenfunctions so as to discuss the characteristics of the major profiles in the temporal and frequency domain.

1 Coastal Background of the Studied Area

The studied area is located in the Shuidong Bay in west Guangdong and the coast is composed of the sand barrier-lagoon-tidal channel systems. Within the area, the huge ebb delta of an accumulative headland nature and the rocky cape to the west dominate the plane morphology of the beach (Fig.1). The studied area is situated in the middle section of the beach, with the beach backshore and the low coastal frontal dune linked up, and the berm lower but broader, and in the surf-zone there exists a large-sized quasi-periodically migrating rhythmic topography—submerged bar or ridge—runnel system. The surface of the beach near the high, medium and low water levels is composed of fine sand, with average grain sizes of 2.78 Φ and 2.40 Φ, and sorting coefficients of 0.51 Φ and 0.60 Φ respectively, and that near the medium water level is composed of medium sand with an average grain size of 1.38 Φ and a sorting coefficient of 0.76 Φ.

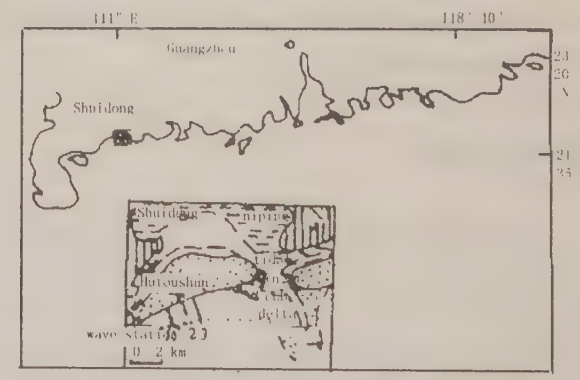

Fig.1 Location of the studied beach and the profile deployment

The tide in the sea area belongs to the irregular semidiurnal tide type with an average tidal range of 1.75m and an average spring tidal range of 2.6m. The nearshore waves are mainly dominated by wind waves with an annual average waveheight of 0.66m, the maximum waveheight of 4.42m, the average wave period of 4s measured during 1986—1987. The constant wave direction in the see area is ESE, with more SE and SSE waves in summer. The constant waves superimposed on the periodic tidal variations are the basic dynamic factor contributing to the beach profile change while the abrupt changes of short period and storm surges caused by the typhoon passing within the year are the important dynamic processes resulting in the erosion, progression and retrogression of the beach profile.

2 Profile Data and Research Methods

2.1 Collection and processing of profile data

Fixed profiles were deployed for repeated measurements in this coastal section of the beach between September, 1986 and December, 1987, each measurement made seawards to the maximum depth that may be reached. Among them, the No.2 profile was measured at an interval of 3~8d and the No.1 and 2 profiles were measured during the spring tide once very month for comparison. The profile elevation was measured jointly with the local sea level. As the data of the No.2 profile may provide more detailed information on the process of profile variations, the paper only makes analysis of the spatial and temporal variation characteristics of the No.2 profile.

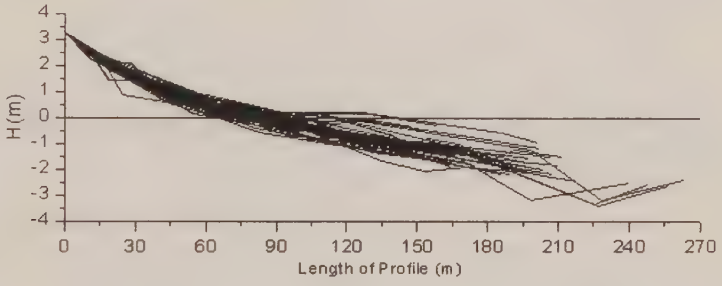

Fig. 2 Measured Process of beach profile variations

The 68 topographic profiles (Fig.2) acquired from the repeated measurement of the No.2 profile are pretreated as follows: Each profile, taking 33 points, is segmentated at an equal spacing of 5m from the backshore to the sea and then each profile point with originally unequal time step is interpolated by cubic spline with a time step of 5 d to obtain the profile data matrix and a total of 97 profiles.

2.2 Empirical orthogonal function decomposition of the beach profile variations

The empirical eigenfunction of the beach profile elevation may be expressed as :

$$h_{xt} = \sum c_{nt} e_{nx} (\lambda_n n_x n_t)^{1/2}$$

Where h_{xt} ——data matrix of profile elevation;C_{nt}——temporal eigenfunction; e_{nx}——spatial eigenfunction; n_x——number of elevation data points for each profile,n_x=33; N_e——number of profiles, N_t=97; λ_n——eigenvalues. The specific steps of calculation are: first equalize the elevation points of each profile, calculate the spatial covariance matrix and then obtain the characteristic values of this real symmetric matrix, extract from several maximum characteristic values the spatial eigenfunctions which account for 90% of the total variance of the beach profile data and the corresponding temporal eigenfunctions with other eigenfunctions regarded as pure random processes and thus not to be further discussed.

2.3 Wavelet transform and wavelet energy spectrum as well as the significance test

If a function satisfies the condition,

$$C_\psi = \int_{-\infty}^{\infty} |\hat{\psi}(\omega)|^2 |\omega|^{-1} \mathrm{d}\omega < \infty$$

then the quadratically integrable function $\psi(t)$ is a basic wavelet or a wavelet generating function, in which $\psi(\omega)$ is the Fourier transform of ψ (t).

In this paper, the Morlet complex wavelet function which is now widely applied in the wavelet analysis is taken as the generating wavelet and it is a plane wave modulated by the Gauss envelope.

$$\psi(t) = \mathrm{e}^{i\omega_0 t} \mathrm{e}^{-t^2/2}$$

Where ω_0——wave vector, generally taking ω_0=6.0. As the complex wavelet transform may give information on both the amplitude and phase of the sequential variations of data, it is more suitable for analysing the oscillating character of the sequence.

With respect to the Morlet wavelet, its dilation dimension a is corresponding to the period T in the Fourier analysis

$$T = \frac{4\pi a}{\omega_0 + \sqrt{2 + \omega_0^2}}$$

By varying wavelet scale a and translating along the localized time index b, the analytical wavelet is obtained:

$$\psi_{a,b}(t) = \frac{1}{\sqrt{a}} \psi\left(\frac{t-b}{a}\right) \qquad a, b \in R, a \neq 0$$

The wavelet transform of the function $f(t)$ is defined as

$$W(a,b) = \frac{1}{\sqrt{a}} \int_{-\infty}^{\infty} f(t) \psi^*\left(\frac{t-b}{a}\right) \mathrm{d}t$$

Where * indicates the complex conjugate.

The average wavelet variance spectrum in the entire time domain is the distribution of wavelet energies (actually also the signal energy) at various scales.

$$\overline{W}^2(a) = \frac{1}{C_\psi} \int_{-\infty}^{\infty} |W(a,b)|^2 \mathrm{d}b$$

Torrence et al.[11] derive wavelet energy spectrum of the theoretical white and red noises to test the peak significance in the wavelet energy spectrum.

The distribution of the local wavelet engergy spectrum is

$$|W(a,b)|^2 \Rightarrow \frac{1}{2} P_k \chi^2 2\sigma^2$$

Where P_k is the Fourier spectrum:

$$P_k = \frac{1-\alpha^2}{1+\alpha^2 \cos(2\pi k / N)}$$

Where k—— frequency index, k=0, ..., n/2; α —— the assumed lag-1 autocorrelation; when α =0, it is the while noise spectrum; N——time series length ; σ^2 is the wavelet variance and the distribution

of wavelet variance spectrum is :

$$\overline{W}^2(a) \Rightarrow \sigma^2 P_k \chi^2_\upsilon / \upsilon$$

Where υ is degree of freedom:

$$\upsilon = 2\sqrt{1+(\frac{Ndt}{\gamma a})^2}$$

In the actual calculation, the basic properties of Fourier transform may be used to acquire the wavelet transform of the function *f(t)*, thus greatly speeding up the calculation.

3 Analysis of Calculated Results

3.1 Major processes of profile spatial variations and their topographic implications

Three eigenfunctions with their eigenvalues which account for more than 90% of the total variance of the beach profile data have been extracted from the empirical eigenfunction decomposition results of the beach profile data matrix and are listed in Table 1. Each spatial eigenfunction represents the main spatial characteristics of the profile topographic variations while the corresponding temporal eigenfunctions indicate the variations of topography with time (Fig.3). Fig.3 a and Table 1 suggest that the first eigenfunction represents the erosion, progression and Transgression of the surf zone topography of the beach profile, which constitutes the most important one of the profile variation processes and account for 66.5% of the total variations of the profile. The first eigenfunction mainly reflects the variation oscillation of the profile caused by the process of progression and transgression with time of the submerged sand bar in the low water zone or surf zone. The related researches have pointed out that this profile is located to the west of the tidal channel mouth of the Shuidong Bay and the beach-connected position of the onshore landing of the swash bar which is resulted from the disturbance of the ebb delta sediment beyond the channel mouth by wave in its process of the westward alongshore transport, while the horizontal movement of sediment caused by the short time abrupt change of wave condition in the sea area during the typhoon is also an important factor contributing to the formation and movement of the submerged bar of the profile. Therefore, the profile topographic implications of the first spatial eigenfunction may be defined as the process of bar movement. The second spatial eigenfunction is mainly manifested in the process of berm erosion, progression and transgression and it can be seen from the distribution of the spatial characteristic vectors that it has a coupling and mutual feedback action with respect to the submerged bar movement; As it is shown in the process of profile variations, the berm scour-and-fill and the bar movement are of a direct and dynamic anti-correlation relationship and the interdynamic process of topography accounts for 18.9% of the total profile variations, and it can thus be defined as the process of berm progression and transgression. The third spatial eigenfunction occupies 7.9% of the total profile variations and the distribution of the characteristic vector values comprising the third spatial eigenfunction mainly reflect the variations of the profile topography above the mean sea level, which occupy 8% of the profile variations. The dynamic process acting on the area and the topographic variations indicated by the

measured profile reflect the counteraction of erosion between the backshore and the beach face topography, which indicates that the profile has been affected by many short-time typhoons . The rough sea and the storm surge result in the intensified uprush and backwash on the beach face to cut the backshore, which is the process of regulation where the backshore profile adapts itself to the waves and the uprush and backwash in the swash zone and is here defined as the backshore erosion process.

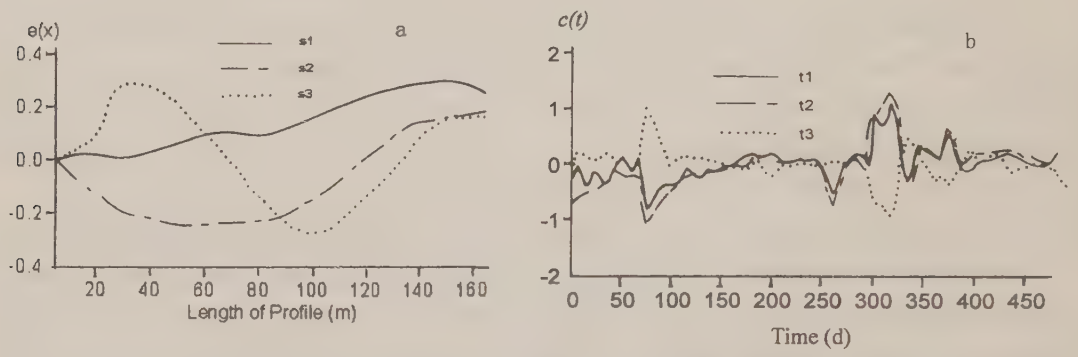

Fig. 3 Three eigenfunctions of the beach profile variation

(a) spatial eigenfunctions (b)Temporal eigenfunctions

Table 1 Three eigenvalues and variance ratios of the beach profile

	λ_1	λ_2	λ_3
Eigenvalues	110.86	31.51	13.19
Percent in	66.51	18.91	9.91

3.2 Time oscillation characteristics of the major spatial processes of profile

Wavelet transform is carried out for the above-mentioned 3 time functions, and the time averaged wavelet spectrum and the local wavelet spectrum are calculated (Figs.4 and 5). The oblique line in Fig. 4 represents the theoretical test spectrum of red noise with a confidence level of 95% and the significance scales of the time-domain average wavelet energy spectrum of the 3 main time functions are listed in Table 2. Table 2 and Fig.4 indicate that the three major spatial processes all possess multiple scale (multicycle) variability and that there exist generally quasi-two month periodic variations, but for the first time function, the most important is the quasi-seasonal (147d) scale. From the fact that the first eigenfunction occupies the most part of the total variance of the entire profile changes, it can be seen that the quasi-seasonal migration process of sand bar is the basic pattern of the beach profile variations. The periodic changes of 20d or 34d as indicated by the various time eigenfunctions may be related to the difference in the erosion action of the wave energy upon the beach under the control and regulation of the monthly periodic changes of the spring and neap tides. Fig.5 indicates the changes with time of different significance scales of the three major spatial processes. Within the period with a time scale less than 62d, all of the three major spatial processes are consistent with the typhoon action upon the beach, (See Table 3), i. e, the short-term high-energy wave condition is the main driving force of the beach variations while the transport of surf-zone bar on a quasi-five

month scale in the local wavelet spectrum of the first time function is still the most important process of seasonal change of the beach.

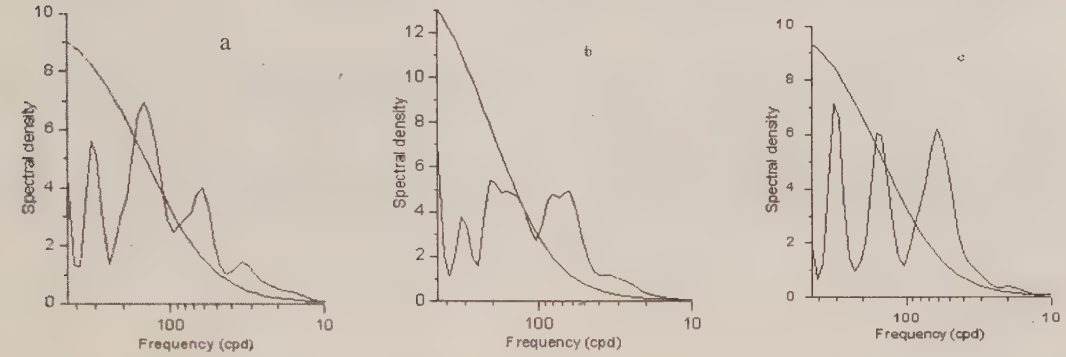

Fig.4 Average wavelet spectrum and red noise theoretical spectrum in the time domain of various time eigenfurctions

(a)The first eigenfunction (b) The second eigenfunction (c) The third eigenfunction

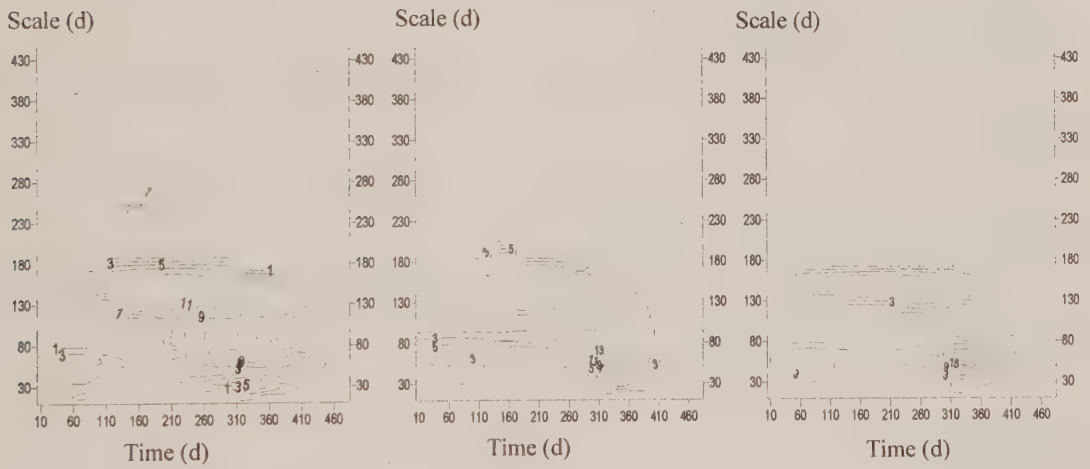

Fig. 5 Wavelet spectra for vaious temporal eigenfurctions

(The fig. only gives the wavelets spectra with confidence level greater than 95%)

(a)The furst eigenfunction (b) The first eigenfunction (c) The first eigenfunction

Table 2 Significance scales of the time-domain average wavelet energy spectrum of time eigenfunctions

Temporal eigenfunction	T 1			T 2			T 3		
Significance scale (d)	34	62	147	34	62	80	20	62	160

Table 3 Dates of typhoons affecting the beach processes

Typhoon No.	8616	8621	8708	8710
Date	1986-09-04	1986-10-13	1987-08-14	1987-08-20

The wavelet spectral analysis of each time function mentioned above reflects the fact that the same spatial process of the beach profile has different time change scales while different spatial processes may have the same period of change, which further indicates that the main spatial variation processes of the beach profile such as migration of bar and berm progression and regression are coupled with each other.

4 Conclusions

Based on the profile data measured in the middle section of the beach to the west of the Shuidong Bay, the decomposed and extracted three spatial functions indicate the major spatial variations of profiles variation with empirical orthogonal functions analysis and the multi-scale oscillation in the time and frequency domain of the three corresponding temporal eigenfunctionswith the wavelet transform. The following conclusions have been drawn from the results of analysis:

a) The transport of submerged bar in the low water zone or surf zone is the most fundamental controlling process of profile variations;

b) The berm near the high water zone and the submerged berm in the low water zone have an interdynamic relationship of erosion, which is the response process of the water profile to the nearshore actions;

c) The strength of the beach-face swash and the erosion feedback of the beach backshore give rise to the action of profile adjustment on the beach;

d) The effect of typhoon is the direct driving force resulting in the multiscale variations of the beach topography while the seasonal wave climate in the see area is a dynamic factor contributing to the quasi-seasonal variations of the beach profile.

References

1 Komar P D. Beach processes and sedimentation. Prentice-Hall, Englewood Cliff, N. J. 429

2 Chen Zishe. Analysis of the dynamic characteristics and stochastic simulation on variation on variations of beach volumes. Acta Oceanologica Sinica, 1995, 14(3): 393—403

3 Aubrey D G. Seasonal patterns of onshore/offshore sediment movement. J. Geophys. Res., 1979, 84: 6347—6354

4 Aubrey D G. The statistical prediction of beach changes in Southern California. J. Geophys. Res., 1980, 85: 3264—3276

5 Aubrey D G and Ross R M. The quantitative description beach cycles. Mar. Geol., 1985., 69:155—170

6 Bowman D. Efficiency of eigenfunctions for discriminant analysis of subaerial non-tidal beach profiles. Mar.

Geol., 1981, 39:242 —258

7 Clarke D J Eliot I G and Frew J R. Variation in subaerial beach sediment volume on a small sand beach over a monthly lunar tidal cycle. Mar. Geol., 1984, 58:319—344

8 Larson M and Kraus N C. Temporal and spatial scales of beach profile change, Duck, North Carolina. Mar. Geol., 1994, 117:75 —94

9 Lau K-M Weng H-Y. Climate signal detection using wavelet transform: How to make a time series sing. Bull. Amer. Meteor Soc., 1995, 76: 2391—2402

10 Jiang Mingshun and Zhang Aijun, Research on the Fine Temperature Structure of the Equatorial Pacific by Using Wavelet Transform, Acta Oceanologica Sinica, 1998, 20 (6): 12— 20

11 Deng Ziwang, Ling Zhenshan and Zhou Xiaolan, Multi-time scale Analysis of the Climatic Change in the City of Xian in the Past Fifty Years, Plateau Meteorology, 1997, 16(1): 81—93

12 Wu Kejian, Song Tinbao and Lou Shunli, Rise and Fall of the Local Wavelet Spectral Peak in the Wind wave, Acta Oceanologica Sinica, 1998, 79: 61—78

Distribution of Annual Rates of Sea Level and Variation of Long-Period Constituents in China

Zheng Wenzhen(郑文振)
(*National Marine Data and Information Service, Tianjin 300171*)

Abstract This paper calculates the annual rates of sea level by using the tidal data of tidal stations, plots the distribution maps of annual rates of sea level and contour lines in China and makes a discussion thereupon. It also analyses the variation of long-period constituents of China's sea level.

Keywords annual rate of sea level; contour line map of annual rates; long-period constituent

1 Analysis of the Tidal (sea level) Data of Tidal Stations

With the help of the tidal curve drawn from the record of the tidal meter, we can get the tidal level of every punctual hour and research into the variation of the comparative sea level with the data of extended continuous tidal level of every punctual hour. We can calculate daily mean sea level from every day's tidal level of every punctual hour, monthly mean sea level from every day's tidal level of every punctual hour, monthly mean sea level from every month's tidal level of every punctual hour, annual mean sea level from every year's tidal level of every punctual hour. The sea level (tidal) record has a clear regularity because of the tidal period caused by the tidal force of the moon and the sun. this can be obtained through harmonic analysis. This method is mature and reliable, which has been in use for a century; and we can deaden the effect of medium and short period tide with years' (months') mean sea level data.

Assuming that M is the mean sea level of time t, the formula can be described as:

$$M(t) = A + Bt + \sum_{i=1}^{n} R_i \cos(\sigma_i t + V_i - g_i)$$

In this formula, A——years' mean sea level; B——sea level trend change, that is, annual change rate (annual mean change rage of sea level), which is the most important element;R_i and g_i —— respectively the tidal amplitude and epoch of the long period constituent i, which are only related to place and called harmonic constant of this constituent;i——angular velocity of constituent$i$; V—— Greenwich astronomical initial facies. The periods of the four constituents applied when calculating annual rate out of annual mean sea level data are as follows:

Node tide of 18.6a is named Mn here. It is comparatively apparent among long period constituent group. We can observe its effects on natural phenomena such as ocean, weather and earthquake. The periods of the rest three constituents are 11.13 a (mean period of sunspo activity), 3.57a and 1.19a

(polar wandering period). Another two constituents should be added when analyzing annual rate out of monthly mean sea level data-Sa (solar year constituent) and Ssa (semi solar year constituent).

It should be pointed out that the variation of sea level is very complicated, and the cause of that has not been made out yet. The elements we have considered here (annual rate and period) cannot represent all the causes. For instance, mining subterranean water is a very difficult and complicated problem, especially for some coastal cities. But we can only deal with it this way due to limited data .

2 Sea Level Annual Rate of Tidal Stations in Coastal Areas of China

The author hereby analyses and calculates the sea level data of 52 long-time tidal stations in coastal areas of China. The result shows that the sea level rises in 43 stations (account for 82.7% of the total) and descends in 9 stations (account for 17.3% of the total). See Table 1.

Table 1 Distribution of annual rate of sea level along the coast of China

Sea Areas	Statue of Stations	Number of Stations	Mean Annual Rate (mm/a)	Standard Deviation (mm/a)
Bohai Sea	4 rises, 2 declines	6	2.6	4.0
Yellow Sea	4 rises, 5 declines	9	0.8	3.5
East Sea	16 rises, 1 declines	17	2.7	1.6
South Sea	19 rises. 1 declines	20	2.1	1.3
Total	43 rises, 9 declines	52	2.1	2.3

As for provinces and regions, the average annual rise rate along the coast of Liaoning Province is 0.26 cm/a. There are only two stations in Hebei Province and Tianjin city—Tanggu and Qinhuangdao. The annual rise rate in Tanggu is 0.22cm/s. (This figure should be larger. The accurate figure cannot be calculated because of subsidence corrections. Because of overmining subterranean water, the ground level in Tanggu declines too much; therefore the annual rate should be 0.6cm/s. The elucidation is found in the following paragraphs.) The annual rate in Qinhuangdao is declining, which is -0.21cm/a. There forms an ideogram of "0" (the sea level neither rises or declines) in the outer sea of Qinhangdao (starting from between Huludao and Qinhuangdao, going easwards, circling the outer sea of Qinhuangdao and going southwards, then winding westwads to the area between Qinhuangdao and Tanggu). Yangjiaogou in Shandong is the station where the sea level rises the most in China according to the available data; its annual rate is 0.93cm/s. Longkou, Yantai, Weihai, Rushankou and Qingdao in Shandong Province are regions where sea level declines (ground level rises), and the annual rate is -0. 13cm/a. There is an ideogram of "0", which is a stable area, starting from the southwest of Longkou, going southwest, passing the land of Sahndong Peninsula and going southeast to the southwest of Qingdao. In the following paragraphs there is an elucidation of the ideogram of "0" made up of the seacoast of Shandong and of Korea. The sea level of Lianyungang is dropping. Lusi has one of the largest sea level rises according to the data available, which is 0.72 cm/a, only next to that of Yangjiaogou, Shandong. In the Jiangsu estuary of Changjiang River and Shanghai City to the south of

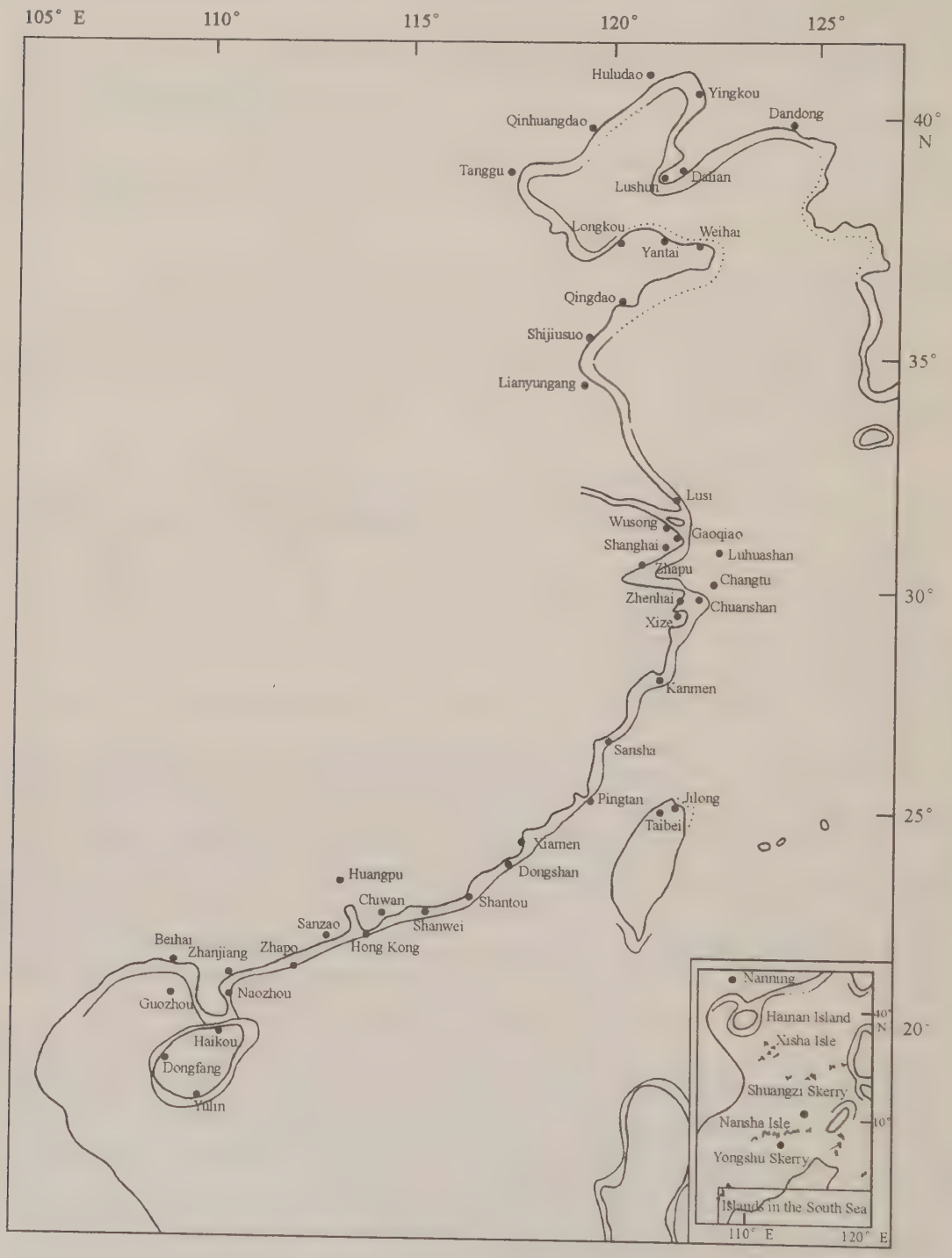

Fig. 1 Annual Rate of Sea Level in the Coastal Areas of China

———— Sea level rises

- - - - - - - - - Sea level declines

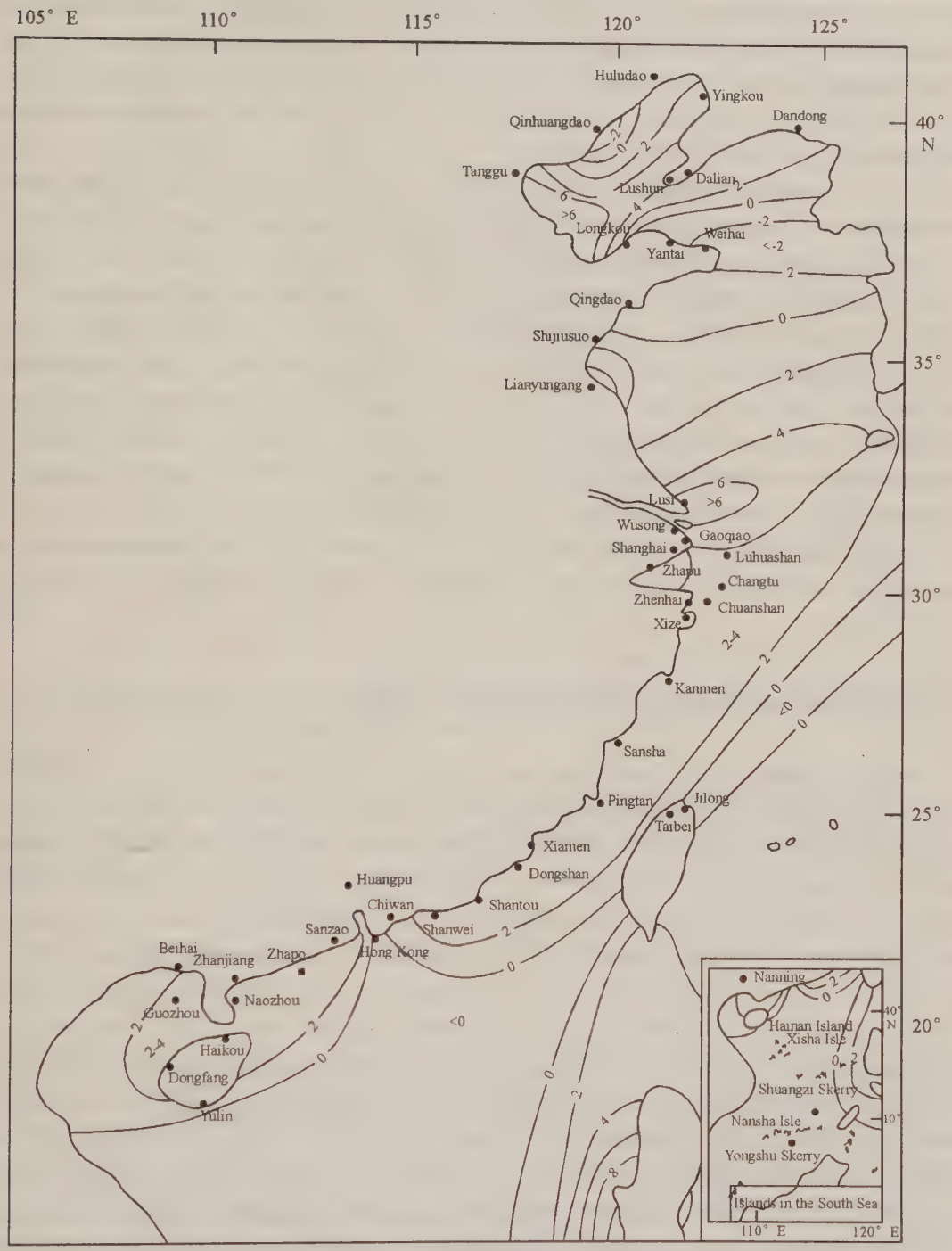

Fig. 2 Isogram of annual rates of level in China Seas unit:mm

Positive Numbers :Sea level rises

Negative Numbers : Sea level declines

Lusi, the mean annual rate is 0.45cm/a. (There is correction for subsidence in the data of Wusong and Shanghai, etc, so the actual annual rate should be larger). The average annual rates for Zhejiang, Fujian, Guangdong, Guangxi and Hainan are respectively 0.34, 0.19, 0.21, 0.28 and 0.17cm/a. As for Taiwan Province, only the data for Gaoxiong and Jilong are available. The calculation result is that the sea level rises in one city and declines in the other.

Besides extended slow rise of sea level, other causes of coastal flood are overmining groundwater , storm surge or flood, astronomical tides, low ground level and projecting terrain, etc.

Totally speaking, the distribution of the rise and decline of sea level along the coast of China has a clear regularity (See Fig. 1). The trend of China's sea level is on the rise, but the variation in the North is different from that in the South. The coastal area to the north of Changjiang River can be regarded as the boundary. The sea level at all the stations to the south of Lusi is rising (except Jilong and Hong Kong, etc), and the rise is very apparent at some stations. To the north of Lusi, the sea level rises at some stations and declines at other stations—it rises in Bohai Sea and declines in Shandong Peninsula. The mean sea level annual rate along the coast of China is 1.4—2.1mm/a. The annual rate would be larger if we added some other stations, which have larger subsidence.

As for sea areas, the mean annual rate of sea level is 2.6mm/a along the coast of Bohai Sea, 0. 8mm/a at the coast of Yellow Sea, 2.7mm/a along the coast of East Sea, and 2.1mm/a at the coast of South China Sea.

3 Distribution of the Isograms of Sea Level Annual Rates in China Seas

We can calculate the distribution of isograms of sea level annual rates in China Seas (See Fig. 2) with sea level data of the 52 stations along the coast of China and the annual rates of sea level along the coast of Korea, Japan, the Philippines, Malaysia and Vietnam. From Fig. 2, we can see that the sea level of most sea areas in Bohai Sea is rising. Among them, the annual rate at Yangjiaohou is the largest, which reaches 9.3mm/a; the second largest is at Tanggu, which is 6.0mm/a. (Since the present data of Tanggu has subsdence corrections, the result of the calculation of the present data is 2.2mm/a. Through the analysis of other data conerning sea level, the author thinks that 6.0mm/a is more reasonable). The third is at Yingkou, which is 2.4mm/a. Therefore, the sea area from Tanggu to Yangjiaogou is one of the areas where the sea level rises most in China. Sea level at Qinghuangdao is declining. Some suggest that the sea level at Qinghuangdao Station is rising, which is different from the author's calculation result and needs further investigating. The sea level is rising in most areas in Bohai to the south of Huludao and Yingkou, Liaoning Province and the east coast of Bohai Sea. The isogram of sea level annual rate larger than 6mm forms a large sea level rising area with Yangjiaohou as the center. (The annual rate at the center can reach 9mm/a). In Yellow Sea, an isogram of "0" starts from Longkou, goes eastwards via Changdao at the boundary of Yellow Sea and Bohai Sea and the outer sea of Yantai to Jiaodao Island of Korea. A central area of declining sea level (rising ground level) forms from the boundary of North and South Yellow Sea out of Chengshanjiao, Shandong Province to sea areas near Inchon, Korea. Another isogram of "0" starts from the southwest of Qingdao and goes

eastwards via the sea to sea areas near Xunwei Island, Korea. In the south of Yellow Sea, a central area of rising sea level forms with Lusi and Changjiang River Estuary as the center. The rising rate at the center is larger than 7mm/a. This is also one of the areas where sea level rises the most in China. In the East Sea and South China Sea, the sea area near Hangzhou Gulf is also one of the areas where sea level rises most. The annual rate for Zhapu is 5.2mm/a. The area from the coast of Hejiang and Fujian to Chiwan, Guangdong Province is a sea level rising area, where the annual rate of sea level is 2—4mm/a. Hong Kong belongs to the sea level declining area, and therefore a long isogram of "0" starts from the northeast of Hong Kong and goes southeast via the east coast of Taiwan, passes the west of Jilong and goes northeast via East China Sea to the Five Islands in Japan, then via Yiqi Island in Duima Strait to the north of Pusan, Korea. The offshore area of the East China Sea, Taiwan Straits and the coast of Guangdong Province in the South China Sea are sea level rising areas, where the annual rates are mostly 2—4mm/a. There is another isogram of "0" starting from the southwest of Hong Kong and going via the outer sea of Yulin to the estuary of Beibu Gulf. Offshore areas of Hainan, Guangxi and Guangdong to the north of this isogram are sea level rising areas. Among them, the annual rates of sea level near Leizhou Peninsula (The annual rate of sea level at Nandu of the east coast is the largest, which is 4.4mm/) and Zhujiang Estuary are comparatively larger. Annual rate of sea level are 2—4mm/a in most sea areas along the coasts of Guangdong (to the west of Zhujiang River), Guangxi and Hainan.

As for regions, the sea level rises the most in the following areas: Yellow River Delta (including old Yellow River and modern River Delta, that is, from Tanggu to areas near Yangjiaogou), Changjiang River Delta (including Hangzhou Gulf), the east coast of Leizhou Peninsula and Zhujiang River Delta.

Sea areas near Qingdao are where the land and oceanic isogram of "0" of annual rate of sea level passes. Therefore, it is reasonable to assume the mean sea level of Qingdao as the benchmark of ground altitude of China.

4 The Relation Between Long-Period Constituents and the Variation of China's Sea Level

The sea level cure obtained from the tide gauge record has certain periodicity, but it is not very strict. Following is the comparatively apparent periods of the variation of China's inshore sea level: (1) M_n constituent of mode tide caused by 18.6a periodic effect of the tidal force. It is comparatively apparent among the long periods. If this constituent is omitted, there may be great error in calculating annual sea level rate when the sea level data has short time series. (2) The period around 11a, which relates to the sunspot. (3) China's sea level changes regularly in accordance with the change of season. This is mainly manifests in S_a(year constituent) and S_{sa}(semi-year constituent). These elements should be carefully considered not only in the research of sea level variation, but also in tidal forecast, storm and disastrous tide forecast and harbor construction project, etc; otherwise they will cause great error and loss. (4) There are still two small constituents whose periods are respectively 1.19a and 3.57a.

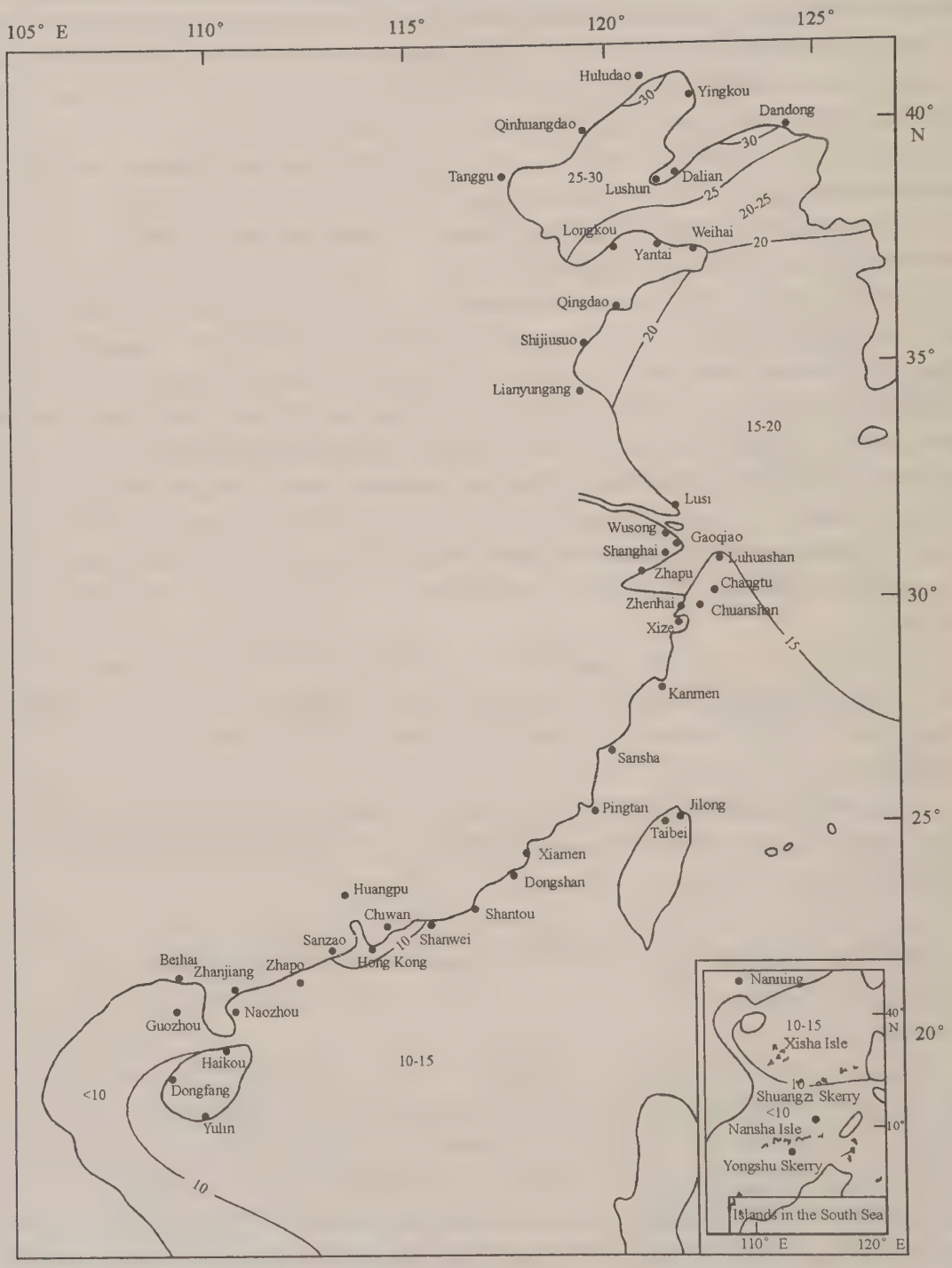

Fig. 3 Distribution of the amplitude of annual constituent Sa in China Seas(Unit:cm)

4.1 Distribution of S_a and S_{sa} constituent

S_a and S_{sa} constituents, which are most closely related to sea level variation, can be calculated from the continuous tidal data of a whole year. In this paper, the amplitude and tidal epoch of S_a are calculated from long time's continuous monthly mean sea level data. In the 6 constituents of China's costal area, the amplitude of S_a is the largest. It is much larger than thos of the rest five, and that of S_{sa} is the second largest. (See Table 2)

Table 2 The amplitude of constituents S_a and S_{sa} (cm)

Sea Area	Observatory Number	Sa (Annual Constituent)		Ssa (Semi-annual Constituent)		Ratio of mean amplitudes
		Mean Amplitude	Variation Range	Mean Amplitude	Variation Range	
Bohai Sea	6	27.9	23.8-30.7	3.5	1.8-9.2	8.0 : 1
Yellow Sea	9	22.6	17.9-25.6	2.5	1.7-3.3	9.0 : 1
East Sea	17	14.2	11.7-25.0	5.0	3.2-9.9	2.8 : 1
South Sea	20	10.9	8.5-13.9	6.0	3.7-9.2	1.8 : 1
Total	52	16.7	85-30.7	4.78	1.7-9.9	3.6 : 1

From Table 2, we can see that the average amplitude of S_a in our country is 16.7cm, and that it has a regular distribution—in Bohai Sea and Yellow Sea, the amplitude is the largest, and it decreases gradually from the north to the south. In most areas in Bohai Sea, the amplitudes of S_a are among 25—30cm. Only in a small costal area near Huludao Island, it does exceed 30cm (about 31cm); in the sea areas to the north of the central North Yellow Sea, the amplitudes of S_a are among 25—30cm; In the costal areas near and west of Dandong, they are among 31—35cm. In the sea areas to the south of the central North Yellow Sea (from Chengshantou to Inchon), they are 25—30cm; in the sea areas in the middle and east of south Yellow Sea, they are 15—20cm; from costal areas southeast of Shandong Penisula to costal areas near Lianyungang, they are 20—25cm. The amplitudes of S_a are 15—20cm from Luhua Mountain, Zhenhai, to Naha, Okinawa Island via the middle of the East China Sea in the north of the East China Sea area, 10—15cm in the sea areas north of the line from Xisha Islands and Zhongsha Islands in the South China Sea to Manila, among 10—15cm in the west costal area of Hainan, 10—15cm in the South China Sea area, 5—10cm in the sea areas in the west of Beibu Gulf, and 5—10cm in the sea areas south to Nansha Islands and Zhongsha Islands in the South China Sea. Fig. 3 is the distribution of annual amplitude of Constituent S_a in China Sea. In Fig. 4, the tidal epoch of S_a is not the isolines of angles, but the corresponding months of the highest sea level of solar annual constituent S_a, that is, the months during which monthly mean sea level is the highest. The tidal epoch of S_a (months of highest sea level) has a regular distribution. From Fig. 4, we can see that it is July in Bohai Sea, between July and August in Bohai Strait, August in Yellow Sea, August in the outer area of the East China Sea and Taiwan, September in the costal areas of Jiangsu and Zhejiang near the estuary of Changjiang River, October in the costal areas of Guangxi, Hainan, Fujian and Guangdong (except that in s small see area from Zhapo to the east shore of Guangzhou Strait, it is November). The annual constituent tide bulge flows from east to west after it enters the South China Sea via Bashi Channel. The date of highest sea level varies from August in Bashi Channel and September in the South China

Sea, to October in Hainan Island, Beibu Strait of China and the costal area of Vietnam. The date of monthly mean sea level climax is late July in Bohai Sea, and it gradually defers from the north to the south.

Compared with the distribution of S_a, the amplitude of S_{sa} is much smaller than S_a, so it only plays a supporting role in affecting sea level. Average amplitude of S_{sa} in China is 4.7cm, and following is its distribution. The amplitude is 2cm in the north of Bohai Sea and soars to 9cm in Yangjiaogou Trench in the south. The amplitudes are 2—3cm in the Bohai Strait, 5—10cm in northern costal area of North Yellow Sea, 2—3 cm in the middle of North Yellow Sea and 3—4cm in the south. In Yellow Sea, the amplitudes of S_{sa} are small and equally distributed. The average amplitude of S_{sa} is 5cm in the East China Sea, and it varies from 3.2 to 9.9cm. the average amplitude of S_{sa} in the South China Sea is 6cm, and in the costal areas of Guangdong, it varies from 4.3 to 9.2cm, mostly above 5.0cm. In the costal areas of Hainan, it varies from 5.4 to 6.3cm. In the north Sea of Guangxi and Weizhou Island, it is respectively 3.7 cm and 4.1cm. In short, the distribution of the amplitude of S_{sa} in the costal areas of China increases gradually from the north to the south.

The distribution of tidal epoch of S_{sa} also has its regularity. The amplitude of semi-annual constituent S_{sa} becomes the highest in August and February in the east of Bohai Sea, in most areas of North Yellow Sea and in the east of South Yellow Sea. As for most areas in the middle and west of Bohai Sea, in northwest costal areas of Korea, in the west of South Yellow Sea, in the outer East Sea and most sea areas to the east of Taiwan, it is in September and March. For offshore waters to the south of the estuary of Changjiang River in Jiangsu Province, costal areas of Zhejiang and Fujian (Taiwan Strait), sea areas to the south of Guangdong and Hainan (including areas in the South China Sea to the east of Beibu Gulf), it is in October and April. For the costal areas near Pingtan, Fujian Province and near Guangxi Province, sea areas in the west of Beibu Gulf and near Nansha Isle, it is in November and May. Since the amplitude of S_a is much larger than S_{sa} in the costal areas of China, S_a becomes dominant in northern ports of out country. The maximum time of the amplitude of S_a is the same as the time when the sea level is the highest. Monthly sea level of Bohai Sea and Yellow Sea becomes the highest respectively in July and August. For the juncture of Yellow Sea and East Sea, the sea level becomes highest in September and lowest in January and February. In Bohai Sea, the discrepancy between the highest and the lowest sea level is about 60cm; in Yellow Sea, it is about 30—70cm (large in the north and small in the south); furthermore, the curve of monthly mean sea level is very regular. The amplitude of S_a gradually decreases from the north to the south, while that of S_{sa} gradually increases. In the East China Sea, S_{sa} is also in effect though S_s is dominant. The highest monthly sea level occurs between September and October, which is quite apparent. The lowest sea level occurs between February and July, which is not so obvious. The discrepancy between them is about 25—35cm. In the costal areas of South Sea. The highest monthly sea level occurs between September and October, while the lowest occurs between March and July (mostly in July). The sea level curve from March to July is quite even, which is an apparent effect of S_{sa}. Even in Huangpu Port, the highest sea level occurs both in October and in June. In the north of South Sea, the discrepancy between the highest and the lowest sea levels is about 20—35cm. In Guangzhou Gulf, it is 35—45cm, which is comparatively large.

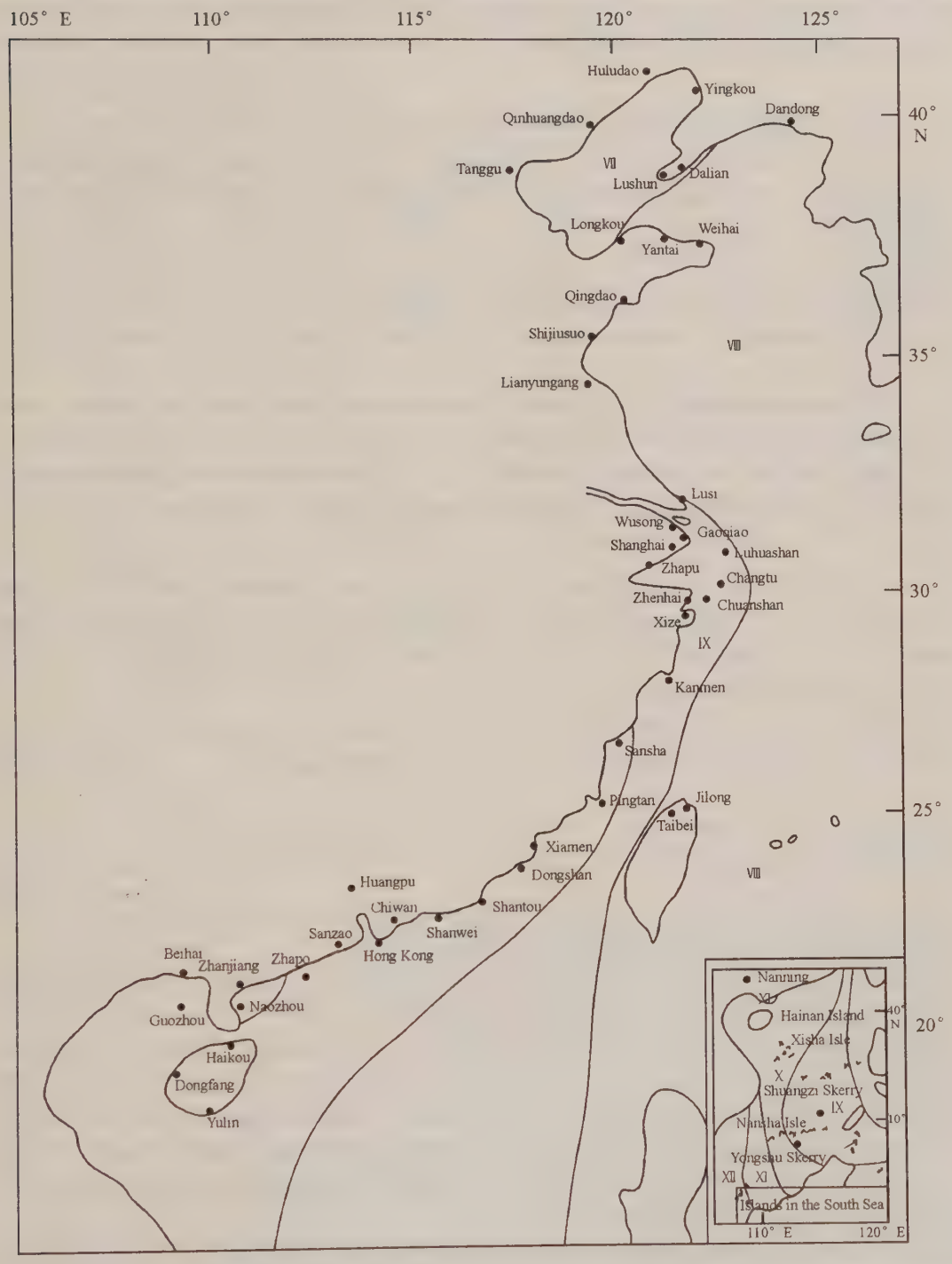

Fig. 4 Distribution of Cotidal Time Line of Annual Constituent Sa in China Seas(Numbers refer to Months)

4.2 The amplitude of four constituents in our country, including M_n and sunspot period

From the mean sea level data of 52 tidal observatories in out country, we can calculate the

average amplitude of the long period constituents 18.61a(M_n) and 11.3a in costal areas, which is respectively 2.7cm and 1.3cm. (See Table 3)

Table 3 Amplitude of sea level constituents 18.61a and 11.3a in costal areas of China (cm)

Sea Area	Obseratory Number	Mn(18.6la)		Sunspot Period(11.13a)	
		Mean Amplitude	Variation Range	Mean Amplitude	Variation Range
Bohai Sea	6	3.5	0.9-7.3	1.9	0.5-3.2
Yellow Sea	9	2.2	0.7-4.5	1.2	0.7-1.7
East Sea	17	2.5	0.7-6.8	1.5	0.4-3.3
South Sea	20	3.0	0.9-6.4	1.4	0.3-3.4
Total	52	2.7	0.7-7.3	1.4	0.3-3.4

The theoretical amplitude of M_n is about 1cm, but the analysis of actual data shows that the distribution of its amplitude is not even in sea areas in China. The amplitude of M_n is the largest in Bohai Sea (3.5cm) and the smallest in Yellow Sea (2.2cm). The distribution of the amplitude of sunspot period is similar to that of M_n—the largest in Bohai Sea (1.9cm) and the smallest in Yellow Sea (1.2cm).

The amplitude of constituent S_a is much larger than the other five periodic constituents. The next is constituent S_{sa}. The astronomical factor is the background of these two constituents, but the atmospheric effect is dominant. As for the node tide M_n and the sunspot period constituent 11.3a, the astronomical element is the main factor.

In China, the mean amplitudes of constituents 1.19a (polar wandering period) and 3.57a are respectively 1cm and 0.9cm, which are too small to be worth researching here.

Reference

1 Zhou Tianhuan, Chen Zongyong, Tain Hui et al. Research of Sea level Variation Trend in Costal Areas of China in Recent Years.Acta Oceanologica Sinica, 1992, 14(2): l—8

2 Zheng Wenzhen et al. Prediction of Sea Level at Any Point Throughout the World and in the Costal Areas of China in the 21th Century. Mrine Science Bulletin, 1996,15(6):1—7

3 Zheng Wenzhen et al. A study of long period sea level changes in the China Sea areas. Mar. Geophys. Res. 1984, 7( ): 299—306

4 Zheng Wenzhen et al. Sea level research in China, Report of International Seminar on Mean Sea Level Monitoring in Asian and Oceanian Regions. Japan Hydrographic Association, Tokyo, 1992, 59—63

5 Zheng Wenzhen et al. Annual variation rate o fglobal sea level rise and the prediction for the 21st century. Aca Oceanologica Sinica, 1996, 15(3):323—330

6 Zheng Wenzhen et al. Study on the Genesis and Occurrence of Great Earthquakes and Their Prediction, Marine Science Bulletin, 1997,16 (1):39—44

7 Zheng Wenzhen et al. The Verification and Prediction of Method for Prediction of Movement Resonance of Great Earthquakes. Marine Science Bulletin, 1999, 18 (1): 52—58

Determination and Analysis of Oceanic Heat Flux Under Sea Ice Cover in the Liaodong Bay

Ji Shunying(季顺迎) Yue Qianjin(岳前进)
(*State Key Laboratory of Structure Analysis of Industry Equipment, Dalian University of technology, Dalian* 116023)

Abstract The calculative methods of oceanic heat flux are discussed firstly, and the oceanic heat flux in the winter of 1997/1998 is calculated using the residual method based on the meteorological, dydrological data and sea ice conditions observed on the JZ20-2 oil/gas platform in the Liaodong Bay. From the results, we can see that the oceanic heat flux is more than 200 W/m^2 at the beginning of the freezing period, then it decreases continuously, and at the end of the winter, it is about 0. At last, the influences of meteorological and hydrological conditions, ice thickness and sea ice type on the oceanic heat flux are discussed. The oceanic heat flux in the Bohai Sea is calculated for the first time, and its trend in the whole winter is obtained.

Keywords sea ice; Bohai Sea; residual method; oceanic heat flux

Introduction

In the sea ice numerical model, the oceanic heat flux is important to sea ice simulation and prediction. Since the 1960s, the study on the oceanic heat flux in the ice-covered region has been a subject of concern..

In different ocean regions, a series of values of the oceanic heat flux have been determined. For instance, Hibler and Bryan (1987) found that the value was more than 350 W/m^2 in the Greenland and Norwegian Sea. Some sensitivity tests of the oceanic heat flux were dealt with in the East Greenland area using the thermodynamic part of the two-level ice model by Lu(1987), and then 350W/m^2 was adopted. In the Saroma-ko Lagoon of Japan, the oceanic heat flux ranges from 33 to 75W/m^2(Shirasaw a, 1997). Perorich et al. (1989) found that the valuc was in the range from 7 to 128W/m^2 in the MIZ. In the Bohai Sea of China, Wang (1984) chose 0, 50 and 100 Cal/(cm^2 • day)(i.e. 0, 24.19 and 48.38W/m^2) in the sensitivity simulation, and found that the boundary line of sea ice simulated was affected by the oceanic heat flux obviously. For the reasons above, we can see that the oceanic heat flux is different in different sea areas. Moreover, even in one and the same area, the oceanic heat also varies with the time and space. For example, Lu(1990) found that in the Greenland Sea area, the oceanic heat flux in summer was greater than that in winter, and the value in the north it was greater than that in the south. The values of 2 and 20—40 W/m^2 were selected to simulate the sea ice of the central Arctic and

the MIZ by Liu (1998) respectively.

The methods to determine the ocean heat flux include the eddy-correlation method (Mcphee, 1987), bulk model formulation(Polland,1983) and residual method(Shirasawa et al. 1997). The complexity of the thermal interaction between ice and water creates difficulties in studying the heat balance of floating ice. Detailed studies of the heat flux from the ocean to the ice were conducted during CEAREX (Correlated Eastern Arctic Experiment) (Wettlaufer et al., 1990; Wettlaufer et al., 1990). The oceanic heat has a close relationship with the hydrological factors (tide, current and salinity etc.), meteorological factors (air temperature, wind velocity and relative humidity etc.) and sea ice factors (thickness, type and roughness etc.). Based on the field observations, the oceanic heat flux can be determined with the eddy correlation method (Mcphee, 1987; Wettlaufer, 1991; Shirasawa, 1997). Next, based on the temperature of water and ice bottom, the oceanic heat flux can be determined with bulk model formulation (Polland,1983; Moore, 1988; Josberger, 1987). Moreover, the residual method, in which the oceanic heat flux is calculated using the heat balance at the bottom of sea ice cover, is applied widely (Omstedt, 1992; Shirasawa, 1997; Harvey, 1990). In addition, the range of the oceanic heat flux can also be determined through the sea ice sensitivity simulation (Lu, 1990; Wang, 1984)

A sea ice field observation station has been established on the JZ20-2 platform in the north Bohai Sea to measure the meteorological data, hydrological data and sea ice simultaneously. Based on the observed data, the oceanic heat flux was calculated with residual method, and its effective factors are discussed.

1 Determination Methods of Oceanic Heat Flux

In the growth of the sea ice, the interactions of turbulent moment, heat and salinity between sea ice and water are coupled together (Mcphee, 1987; Wettlaufer, 1991). Based on the Fourier law, the oceanic heat flux can be obtained by

$$\rho c\frac{\partial T_i}{\partial t}=\frac{\partial}{\partial z}\left(K\frac{\partial T_i}{\partial z}\right)+Q_{se}\gamma_i e^{-\gamma z} \tag{1}$$

where w' is the vertical flow fluctuation at the bottom of the ice cover , T' is the temperature fluctuation, and < > denotes time averaging. A relation between w' and water salinity was established by Mcphee(1987), which can be determined using salinity and temperature balance equations in the oceanic boundary layer under ice cover(Mcphee, 1987).

The oceanic heat flux can also be calculated simply with the bulk formula, in which the detailed physics of the thermal ice-ocean interaction is parameterized in terms of a heat coefficient C_h (which can also be called Stanton Number). Thus, the oceanic heat flux can be calculated by

$$F_w=\rho_w c_p C_h u_*(T_w-T_m) \tag{2}$$

where ρ_w and c_p are water density and specific heat respectively, u_* is the friction velocity, T_w and T_m are far field water temperature and freezing point, and T_m is the function of water salinity

(in the simple, T_m = -0.0544 S_w , and S_w is the salinity at the interface). Sometimes, the relative velocity between sea ice and water u_{wi} substituts for u_* , and the heat coefficient should be adjusted accordingly.

In the residual method, the ocean heat flux is calculated as the difference between vertical heat flux within the growing sea ice and the latent heat released by freezing at the ice-water interface. As the Bohai sea ice is not thick enough , the solar radiation at the sea ice bottom should be considered. At any location in the growing ice sheet, the energy balance at the ice-water interface can be described by

$$F_w = -\rho_i L_i \left(\frac{\mathrm{d}h_i}{\mathrm{d}t} \right)_0 - F_c - Q_{sb} \tag{3}$$

Where ρ_i is the sea ice density, L_i is the heat of fusion of sea ice, $\left(\frac{\mathrm{d}h_i}{\mathrm{d}t} \right)_0$ is the sea ice growth rate at the ice-water interface, F_c is the molecular heat conduction, and Q_{sb} is the solar radiation at the sea ice bottom. For the thick sea ice ($h_i > 0.5m$), Q_{sb} is not considered, but in the Bohai Sea, the ice is very thin, (usually, $h_i < 0.2m$), the sea ice growing rate is affected by the solar radiation.

2 Determination of the Oceanic Heat Flux in the Liaodong Bay

On the JZ20-2 platform in the Liaodong Bay, the meteorological, hydrological and sea ice condition were observed in the whole winter in the several past years, and on the basis of the observed data, the oceanic heat flux can be calculated with the residual method. As the oceanic heat flux is determined by using the heat balance in the sea ice growth, the thermodynamic factors should be calculated accurately, which include solar radiation, long wave radiation, sensible heat and latent heat at the ice cover surface and conductive heat in the ice cover.

2.1 Instrumentation

In order to obtain reliable sea ice information for thermodynamic calculation, the meteorological , hydrological and sea ice conditions in the whole winter should be measured in the same time. The meteorological data includes air temperature, wind velocity and relative humidity etc., the hydrological data includes tide, current, water temperature and salinity, and the sea ice information includes ice thickness, compactness, velocity and ice type. Thus, a sea ice observation station has been established on the JZ20-2 oil/gas platform in the Liaodong Bay.

An auto-weather station has been installed at the height of 3.5m above the top of the platform in order to avoid the influence of the platform, which can record the metoerolobical data per second. The current meter is at the depth of 7m under the sea ice cover, which can record the hydrological data per 15 minutes. The type, velocity and trace of the drifting sea ice floes has been observed with a radar station, and the ice thickness has been measured with a video camera, which is fixed on the platform.

In the Liaodong Bay, under the action of the wind, current and tide, the sea ice breaks up

constantly during its drifting. Therefore, the change of ice thickness is discontinuous, but it is continuous in the sea ice numerical simulation. In order to deal with the problem, the whole freezing period is divided into numbers of periods, which is about 3—5days, and the influence of dynamic action is not strong. So in each period, the simulated sea ice thickness can be modified by the observed data.

2.2 Results

In the Jz20-2 area, the ice thickness is measured four times per day, respectively at 8:00,11:00, 14: 00 and 17:00. Therefore, the oceanic heat flux can be calculated with the integral of equation (3), and obtain:

$$F_w = \left(\frac{h_{i(2)} - h_{i(1)}}{\rho_i L_i} - \int_{t_1}^{t_2} F_c(t) + Q_{sb}(t) dt \right) \Big/ (t_2 - t_1) \tag{4}$$

where $h_{i(1)}$ and $h_{i(2)}$ are the ice thickness at the time of t_1 and t_2 respectively, $F_c(t)$ and $Q_{sb}(t)$ are both the functions of the time t 。

Here, using the ice thickness measured at 8:00 and 17:00 in the three days from 1998-01-14 to 1998-01-16, the oceanic heat flux is calculated with the residual method. At the same time, solar radiation, long wave radiation, sensible heat flux, and latent heat flux at the ice-air interface and the conductive heat flux at the ice-water interface are all calculated (Shown as Fig. 1). Some results are listed in Table 1, and the mean value of the oceanic heat flux in the three days is 179.65W/m^2. Using the oceanic heat flux, the sea ice thickness in the three days is calculated, and the results are shown as Fig.2.

Table 1 The calculating process and results of oceanic heat flux in three days

Date	time	h_i (cm)	$h_{i(2)} - h_{i(1)}$ (cm)	$t_2 - t_1$ (h)	$\int_{t_1}^{t_2} F_c(t)dt$ ($\times 10^6$ J/m^2)	$\int_{t_1}^{t_2} Q_{sb}(t)dt$ ($\times 10^6$ J/m^2)	F_w (W/m^2)
1998/	08:00	8	--	--	--	--	--
1/14	17:00	6	-2.0	9	-6.519	4.287	255.31
1/15	08:00	7	1.0	15	-12.194	0.322	188.93
	17:00	6	-1.0	9	-5.501	3.949	141.11
1/16	08:00	7	1.0	15	-12.128	0.175	190.88
	17:00	6	-1.0	9	-4.831	4.193	112.91

Using the method above, the oceanic heat flux was calculated in the winter of 1997—1998, and the trend and range of the value are shown in Fig. 3. From it , we can see that, in the Liaodong Bay, there is a great difference in the whole winter. In the freezing period, the oceanic heat flux is more than 240W/m^2, then decreases continuously, ant in the melting period, the value equals to zero. Using the determined value, the sea ice thickness in the winter of 1997/1998 was simulated with sea ice thermodynamics, and the results comport with the data measured on the JZ20-2 sea ice observation station, which is shown in Fig. 3. If the sea ice dynamics was considered, the results would be more

reasonable.

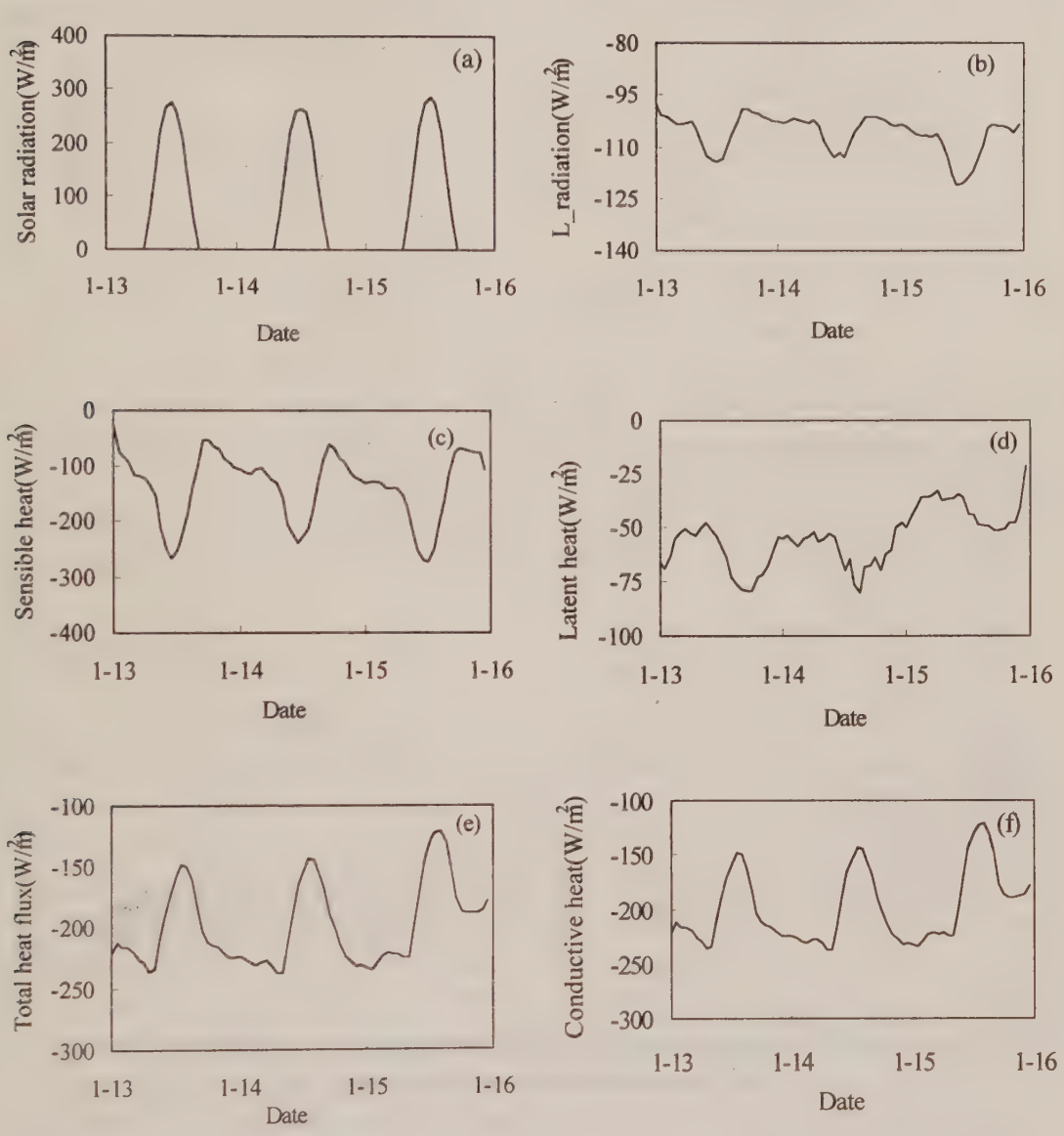

Fig.1. Sea ice thermodynamic factors calculated from 00:00 of 1998-01-14 to 23:50 of 1998-01-16

2.3 Discussion

Besides the influence of the physical mechanism of the turbulence, the oceanic heat is affected by water temperature, salinity, weather condition, ice thickness, ice type and compactness.

(1) Water temperature; In the winter of Liaodong Bay, there is a specific change process of the water temperature. At the beginning of the winter, the water temperature decreases rapidly, then keeps at -1.5℃ for several weeks, and at last increases slowly in the later winter. In the process, the ice-water interfacial temperature is still kept at the freezing point. Therefore, the change of the water temperature

affects the heat flux from the water to the bottom of the ice greatly.

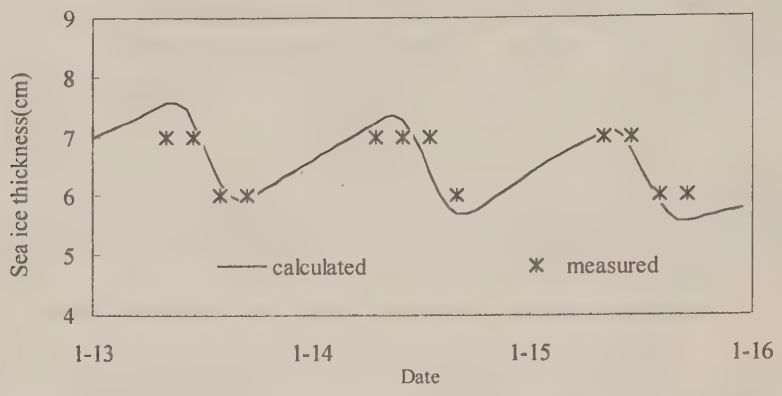

Fig.2 Calculated and measured sea ice thickness from 00:00 of 1998-01-14 to 23:50 of 1998-01-16

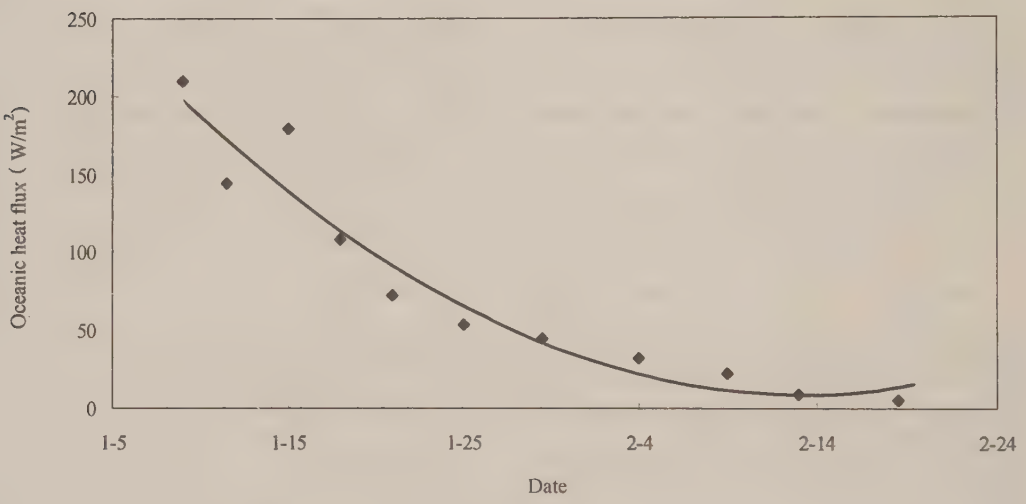

Fig.3 Calculated oceanic heat flux and its matched curve in the winter of 1997-1998 of the JZ20-2 area in Liaodong Bay

(2) Water salinity; The oceanic heat flux is the function of the difference of the water temperature and the freezing point, and the freezing point is determined by the water salinity, so the oceanic heat flux is also affected by the water salinity. The higher the water salinity, the more the oceanic heat flux is.

(3) Weather conditions; Under different weather conditions, the heat flux between air and the ice cover is different, so the temperature field in the ice cover is also different, which can also affect the oceanic heat flux magnitude.

(4) Ice thickness; Under the same meteorological and hydrological conditions, the temperature distribution in the thick ice is different from that of the thin ice, which causes the oceanic heat flux to be different. The oceanic heat flux of the thick ice cover is less than that of the thin ice cover.

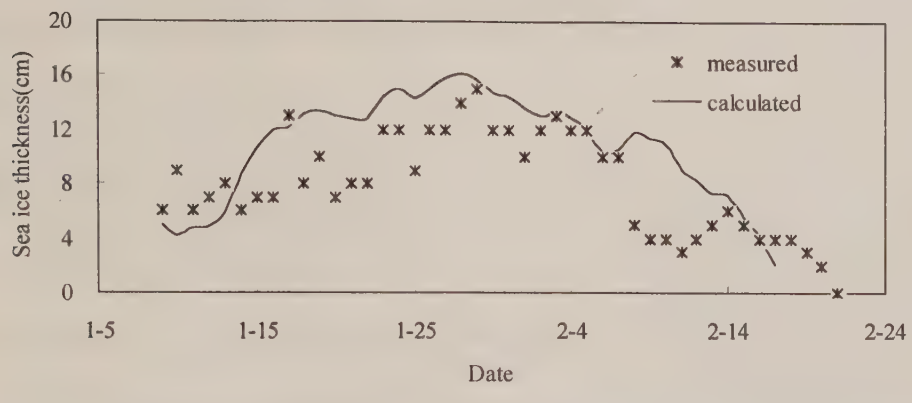

Fig.4 Measured and calculated sea ice thickness in the winter of 1997-1998 of Liaodong Bay

(5) Ice compactness and type; Because the heat flux between air and water is greater than that between air and ice, in the area of low compactness, the heat of the warm water is lost from the open water, and the heat flux under the ice cover becomes lower.

3 Conclusions

Based on the meteorological, hydrological and sea ice condition observed on the JZ20-2 platform, the oceanic heat flux of the Liaodong Bay has been calculated with the residual method. According to the Bohai sea ice feature, the solar radiation at the bottom of the ice cover is considered. From the results in the winter of 1997/1998, we can see that, the oceanic heat flux in the Liaodong Bay has an obvious trend. At the freezing period, the ocenic heat is very high, which is more than 200W/m^2, and in the melting period, the oceanic heat flux decreases to 0. The oceanic heat flux is affected by water temperature and salinity, weather, sea ice thickness and compactness etc.

The oceanic heat flux of 1997/1998 winter in the Liaodong Bay is calculated and discussed, and the range and the trend have been determined, but the result can not be directly utilized in other areas of the Bohai Sea and other winters. In the determintion of the oceanic heat flux, the coupled process of the heat, moment and salinity should be considered, which is still an open problem in the Bohai sea ice numerical simulation.

References

1 Harvey L D D, (1990) Testing alternative parameterizations of lateral melting and upward basal heat flux in a thermodynamic sea ice model. J. Geophysical Research, 95(C5):7359—7365

2 Hibler W D III and Bryan K, (1987) A diagnostic ice-ocean model. J. Physical Oceanography. 17: 987—1015

3 Josberger E G, (1987) Bottom ablation and heat transfer coefficients from the 1983 Marginal Ice Zone Experiment. J. Geophysical Research, 92(C7): 7012—7016

4 Liu Q Z, Bai S, and Wu H D, (1998) Stability of thermodynamic sea ice model on the thermodynamic forcing.

In:Ice in Surface Waters. Proceeding of the 14th inernational symposium on ice, New York, USA. 297—303

5 Lu Q M and Flemming T C, (1990) Summer Sea Ice Simulation in the east Greenland area. IAHR Ice Symposium, 251—258

6 Mcphee M G, Maykut G A and Morison J H, (1987) Dyanmics and thermodynamics of the ice/upper ocean system in the marginal ice zone of the Greenland Sea. J.of Geophysical Research. 92(C7): 7017—7031

7 Moore R M and Wallace D W R, (1988) A relationship between heat transfer to sea ice and temperature-salinity properties of Arctic ocean waters. J. Geophysical Research, 93(c1): 565—571

8 Omsted A and Wettlaufer J S, (1992) Ice growth and oceanic heat flux: Models and Measurements. J. Geophysical Research, 97(c6): 9383—9390

9 Perovich D K, Tucker III W B and Krishfield R A, (1991) Oceanic heat flux in the Fram Strait measured by a drifting buoy. Geophysical Research Letter, 16: 995—998

10 Shirasawa K and Ingram G R, (1997) Currents and turbulent fluxes under the first-year sea ice in Resolute Passage, Northwest Territories, Canada J. Marine System, 11:21—32

11 Shirasawa K, Ingram G R and Hudier E J J, (1997) Oceanic heat flux under thin sea ice in Saroma-ko Lagoon, Hokkaido, Japan. J. Marine System, 11:9—19

12 Wang R, (1984) Numerical tests of Bohai Sea ice. Acta Oceanologica Sinica, 6(4): 572—580

13 Wang Z, and Wu H, (1994) Sea ice thermal processes and simulation of their coupling with the dynamic process. Oceanologia et limnologia sinca, 25(4): 408—414.

14 Wettlaufer J S, (1991) Heat flux at the ice-ocean interface. J. Geophysical Research, 96(C4): 7215—7236

Study on the Genesis and Occurrence of Great Earthquakes and Their Prediction

Zheng Wenzhen (郑文振)
(*National Marine Data and Information Service, State Oceanic Administration, Tianjin 300171*)

Abstract The genesis and main energy source of great earthquakes are discussed, a hypothesis on the resonance of great earthquakes is proposed for solving the unsolved key and core problem in seismology, and new methods for prediction of great earthquakes are first suggested in the paper. The methods are now named "method for prediction of movement resonance of great earthquakes" and "method for correlated prediction of strong earthquakes". Great earthquakes can be estimated from the data in ten to twenty years before the earthquakes by using the method for prediction of movement resonance of great earthquakes and its principle. For example, the great Tangshan earthquakes can be calculated to occur on July 28, 1976 from the data before 1960. The calculation result is consistent with the actual occurrence date without error of one day. As a convincing argument, the author has made successful prediction of several great earthquakes occurring recently, such as Nov. 8, 1997 Mani M7.5 in Tibet, Dec. 5, 1997 Kamcatskij M7.9 in Russia and Jan. 10, 1998 Zhangbei M6.2 in north China. Development of this new hypothesis of resonance of great earthquakes and test of the new prediction methods are fairly satisfactory.

Keywords Great earthquake; Genesis and energy source; Hypothesis of resonance; earthquake prediction, methodology

Introduction

A great earthquake refers here to the one with magnitude equal to or larger than 7, and a strong earthquake to the one with magnitude of $5.0 \leqslant M \leqslant 6.9$.

Earthquake is a natural phenomenon of the earth's movement. Great earthquake is a disaster of large destructive force in the nature. Earthquake prediction together with "living forever of humans" and "treatment of cancer" are the recent three scientific challenges. I consider that "living forever of humans" is contrary to the natural law and is a problem which can not be solved. While cancer patients may die in tens of days, months, one to two or more years and those that can be cured are in the minority, so the problem of cancer is unsolved at the present.

Early in the Donghan Dynasty, more than 1800 years ago (in AD 132), great Chinese scientist Zhang Heng had made out its seismograph. Earthquakes have been studied in Italy for two hundreds or more years and in Japan and the United States about one hundred years. Some scientists discussed the relationship between earthquakes and plate motions and others explained the genesis and

occurrence of earthquakes in terms of plate motion. Several earthquakes occurred near Los Angeles and San Francisco, U.S.A. Some of the earthquakes caused enormous losses. The Los Angeles M 7 earthquake on Jan. 17, 1994 causing a catastrophic damage had not been predicted before its occurrence. The Kobe M 7.2 earthquake on Jan. 17, 1995 causing heavy casualties was not predicted prior to its occurrence. It indicates that plate tectonics theory does not help to predict earthquakes. The plastic rebound theory and the hypothesis of nuclear explosion in the earth's interior suggested by some academic authorities are not suitable for the explanation. Others considered that earthquakes are basically isolate events in the world. This consideration has deeply influenced the seismological sphere and had passive effect on seismological work for many years. Up to now, the challenge on the genesis and occurrence of great earthquakes has not yet been solved in the world.

The Xingtai-Longyao M 6.8 earthquake occurred in Hebei Province on March 8, 1966, and caused heavy casualties. Premier Zhou Enlai pointed out that we need to solve the challenge of earthquake prediction by means of multi-disciplinary collaboration; the key problem which has not been solved internationally must be solved by our efforts with creative spirit as we are fighting with the earth's catastrophes. In 1967, vice-president of the National Commission of Science and Technology Wu Heng and heads of the State Oceanological Bureau asked me to study earthquake prediction in terms of sea level change and from oceanographical aspects.

The author proposes a peculiar view and principle of genesis and occurrence of great earthquakes and hence deduces new methods for earthquake prediction, i. e. the method for prediction of movement resonance of earthquakes and method for correlated prediction of strong earthquakes. These methods will be described in detail in the following sections.

1 Genesis and Energy Source of Great Earthquakes

The key problem of earthquake prediction to be solved is involved with understanding of the genesis and occurrence of great earthquakes and the main factors affecting on the great earthquakes. This problem has not been solved in the international seismological sphere for hundreds of years.

The author suggests that earthquake is closely related with astronomical factors, such as 18.6 years ascending node of the moon, the sunspots activity, and the magnetic field variation, etc. They are the far constraints on earthquake occurrence, while the moon, the sun, and the tidal forces can trigger earthquake occurrence. In the sixth chapter of a co-authors' work Movement of Celestial Bodies and Earthquake Prediction in 1980, Zheng Wenznen suggested a hypothesis of resonant genesis of earthquakes. In order to find the main factors affecting earthquake occurrence, the author analyzed global seismic data from astronomical to terrestrial aspects and eventually found the erergy source for great earthquakes. The author concluded that the local energy accumulation for great earthquakes is secondary, but the main energy source for earthquakes comes from the outer areas. For example, since the twentieth century, five high seismic activity episodes occured in China. The first episode is represented by the August 22, 1902 Atushi M 8.5 earthquake in Xinjiang and December 23, 1906 Manasi M 8.0 earthquake in Xinjiang; The second episode is represented by the December 16, 1920

Haiyuan M 8.5 earthquake in Ningxia, the May 23, 1927 Gulang M 8 earthauake in Gansu, and the August 11, 1931, Fuyun M 8 earthquake in Xinjiang; The third episode is represented by the Autust 15, 1950 Chayu M 8.5 earthquake and the November 18, 1951 Dangxiong M 8 earthquake in Tibet; The fourth episode is represented by the July 18, 1969, Bohai M 7.4 earthquake, the July 28, 1976 Tangshan M 7.8 earthquake in Hebei, the January 5, 1970 Tonghai M 7.7 earthquake in Yunnan, and the February 6, 1973 Luhuo M 7.9 earthquake in Sichuan; The fifth episode started, as considered by some scientists, from November of 1988, but the author considers, that it started from May 18, 1987 M 7.4 earthquake on the Bengal-Burma border, through the November 6, 1988 Lancang M 7.6 earthquake, to January 5, 1991 M 7.6 earthquake on the China-Burma border.

The author suggests that most of the future great earthquakes will occur in Japan Trench including its southern tip up to the northern part of Philippines and its northern tip in juncture with Kurile Islands or in the offshore along the coast of the Far-east of Russia (this prediction was first suggested by the author in November of 1997 when he wrote to his colleague who was working in Japan) where earthquakes will occur in one and half years to come. The exact time (when will be M 7.5~8 earthquake, I knew fairly well.) and concrete site will be determined after detailed analysis of recently occurring M 6~7 earthquake. The fourth high-seismic episode in China has partially migrated to Yunnan and Burma and partially to some area which remains to be estimated and predicted after detailed analysis. The author suggests that at present China still stays in the fifth high-seismic episode and hence several $M \geqslant 7$ earthquakes will occur in the near future. The author will present prediction opinions in accordance with the seismic tendency. The time interval of the first episode from the 1902 M 8.5 earthquake in Xinjiang to 1920 M 8.5 earthquake in Ningxia lasted 18 years. The second episode from 1920 M 8.5 earthquake in Ningxia to 1950 Chayu earthquake in Tibet lasted 30 years. The time interval of the third and fourth episodes starting from 1950 M 8.5 earthquake in Tibet to 1973 Luhuo M 7.9 earthquake in Sichuan and the July 28, 1976 Tangshan M 7.8 earthquake in Hebei lasted 23 and 26 years, respectively. Thus, it may be concluded that the movement of great earthquakes in China's continent from one seismic region to another needs a period of 18 to 30 years. The similar phenomenon is also found in Taiwan region of China, Japan, Chile, the Philippines, and other regions. It can be inferred from the movement of great earthquakes that the energy for great earthquakes in the earth also moves. The energy accumulation in local areas is secondary, but its source in outer area is predominant. The energy from the outer areas can generate great earthquake and hence form a high-seismic episode. So the energy from outer areas is the main factor for great earthquakes. This is fairly different from the concept that the energy is accumulated within the local areas, as most scientists considered.

2 Occurrence and Resonance of Great Earthquakes and New Methods for Its Prediction

In 1980, the author suggested a hypothesis of resonance which refers to a resonant effect of resultant cyclic force from the force applied by celestial bodies and the sun activity on the local seismic

area and causes an earthquake to occur in the local area. Recently, the similar viewpoint was also suggested by Academician Sinyakov. Now Zheng Wenzhen's resonance concept is different from the one described above in that which refers to a resonance of energy movement within the earth's crust. When the outer energies for a great earthquake moving in two or more directions and at different velocities into a local area (site) are approximately equal and meet with each other, the resonance can occur and just at this time an earthquake occurs at this site. This new finding reveals a mystery on the disaster caused by earthquake occurring in the earth's crust. Since then, I have treated a large amount of data and hence confirmed that the great earthquake occurrence is caused by a resonance and characterized by a sudden hit, which results in large casualities and great loss of life and properties. The hypothesis of resonance provides a basis for prediction of great earthquakes and permits the author to suggest a new method for prediction of movement resonance of great earthquakes and to use it for prediction of future great earthquakes.

The energy for great earthquakes transmittes mainly from its source in outer area. According to the migration path of recent great earhquakes and from the data of great (strong) earthquakes having occurred in the outer areas or on the path, we can predict great (strong) earthquake which will occur in a local area. Accordingly, I developed a method for correlated prediction of strong earthquakes.

3 Test of the Prediction

Since the founding of New China, our state has paid great attention to seismological work and a national-wide system of seismograph networks and communication networks has been set up by the efforts of the State Seismological Bureau and Chinese seismologists under the leadership of CPC. A large amount of instrumental data on magnitudes, locations, and occurence time of strong (great) earthquakes provides a sound basis for the estimation of future great earthquakes. Using the method for prediction of movement resonance of great earthquakes and its principles, we can estimate and predict various great earthquakes from the data ten-twenty years before the earthquake. The tested prediction results are fitted with the actual data with only small errors in earthquake occurrence time. It enhanced our confidence in the prediction of great earthquakes. The predicted 20 earthquakes, such as the Aug. 15, 1950 Chayu M 8.5 earthquake, the Nov. 18, 1951 Dangxiong M 8 earthquake in Tibet, the Apr. 14, 1955 Kangding M 7.5 earthquake in Sichuan, the Mar. 1966 Xingtai M 6.8 and M 7.2 earthquakes in Hebei, the Jan. 5, 1970 Tonghai M 7.7 earthquake in Yunnan, ··· and the Feb. 3, 1996 Lijiang M 7 earthquakes in Yunnan, including the Jan. 25, 1972 M 8 earthquake in Taiwan region of China, were tested with an averaged error of ten days according to incomplete statistics. The prediction was also made on M 8~8.1 earthquakes occurring in Japan and Mongolia, and on July 16, 1990 M 8.5 earthquake in the Philippines. The results were also tested with an averaged error of 30 days. Therefore, the method can also be applied to the prediction of global great earthquakes. So we can make long-and-mid term prediction of great (strong) earthquakes and can shorten the predition time interval into one-two months, even can estimate possible earthquake occurrence date.

It is especially noted that the new prediction method was used in the estimation that the Tangshan

great earthquake was to occur at July 28, 1976 from the data fefore 1960, and in the estimation that of Lancang M 7.6 earthquake in Yunnan was to occur on April 26, 1990. The results of theoretical calculation are consistent wtih the actual occurrence time without any error and the calculation of some great earthquakes gives error of 1~3 days. It indicates that the suggested hypothesis of resonance of earthquake genesis and occurrence and the derived prediction method are reliable and correct. So the difficult problem of great earthquakes prediction can be solved.

At the Meeting of Consultation on Seismic Tendency in North China and Bohai Sea Area sponsored by the State Seimological Bureau on June 7~9, 1974, using the great earthquakes movement I had suggested that great earthquakes will occur near Bohai Sea with their magnitudes no less than 5~6, possibly larger than 7, according to the earthquake migration, but it was unknown when they will occur. Then I showed anomalous sea level curves recorded at several observation stations which attacted great attention of the heads of the State Seimological Bureau and were noted in the State Council document No. 69, but no opinion on $M \geqslant 7$ earthquake to occur were described in the document. This document was helpful for the successful prediction and prevention of February 4, 1975 Haicheng M 7.3 earthquake in Liaoning (casualties were decreasen by a hundred thousand people). At that time the author did not develop the method for prediction of movement resonance of great earthquakes. Now I can estimate a great earthquake occurring at July 28, 1976. In combination with high tide time of that day (after Mar. 8, 1966 Xingtai earthquakes several larger earthquakes occurred mostly about the high tide time in Tanggu, the author considered the high tide has its triggering effect on great earthquake occurrence), I estimated the earthquake occurrence moment to be at 3~4 hrs on July 28, 1976. This will solve the difficult problem of great earthquake occurrence moment. If at that time this method for estimation of great earthquake existed, the casualty in the Tangshan earthquake would decrease by some.

4 Practical Prediction

In order to put the method into effect, I have wrote an earthquake prediction paper on Aug. 29, 1996 and sent it to the Earthquake Analysis and Prediction Center, State Seimological Bureau. In the paper I suggested an $M \geqslant 7$ earthquake will occur in Taiwan area and a M 5.5~6.5 earthquake will occur in Yunnan (including southern Sichuan) from Sept. to Oct. 21 1996. Then an M 7.1 earthquake did occur in Lanyu of Taiwan on Sept. 6, 1996 and an M 5.7 earthquake in Lijiang area, Yunnan, on Sep. 25, 1996. Both the only two strong earthquakes merely occurring in China in September were correctly predicted. In particular, in the prediction opinion of Yunnan earthquake presented on Aug. 29, 1996 the predicted occurrence date was reduced to be a time interval of 50 days from September to October 21. This first prediction is fairly successful. On Sept. 18, 1996, in a prediction opinion presented to the Earthquake Analysis and Prediction Center, State Seismological Bureau, the author predicted an M 7.5~8.4 earthquake which could occur along or near Japan Trench in the future one and half years. But its exact occurrence time will be judged from the data of strong earthquake occurring near Japan in the past months. As a result, an M 7 earthquake occurred at 50 km east-south-east of

Miyasaki of Kyushu, Japan on Oct. 19, 1996. It enhanced the author's confidence in prediction of the M 7.5~8.4 earthquakes which will occur in Japan Trench (including the offshore along the Far East of Russia).

As a convincing argument, the author has successfully predicted several great earthquakes occurring recently, such as Nov. 8, 1997 Mani M 7.5 in Tibet, Dec. 5, 1997 Kamcatskij M 7.9 in Russia and Jan. 10, 1998 Zhangbei M 6.2 in north China.

5 Conclusions

(1) From the movement trend of high-seismic episodes we can infer the energy source for great earthquake generation. The energy mainly comes from the outer areas and its accumulation in local area is secondary. The outer energy causes great earthquake to occur in the local area and it is the predominant effecting factor.

(2) The hypothesis of resonance of great earthquake occurrence is that when energies for great earthquakes transmit from its sources in outer areas to a local area (site) at about equal velocity and meet with each other, a resonance takes place and a great earthquake occurs in the local area at this time. Accordingly, I develop the hypothesis of resonance of great earthquakes.

(3) According to the concept of movement of great earthquakes and the principle of resonance of great earhquakes, I develop a method for prediction of movement resonance of great earthquakes and a method for correlated prediction of strong earthquakes. I can estimate occurrence time of various great earthquakes from the data ten to twenty years before the great earthquakes. The occurrence time of Tangshan M 7.8 earthquake was estimated to be July 28, 1976, that of Lancang M 7.6 earthquake in Yunnan to be Nov. 6, 1998, and Gonghe M 7.0 earthquake to be April 26, 1990. The theoretical calculation of these three great earthquakes is consistent with the actual occurrence date without error of a day. It indicates that the new methods derived from the hypothesis of genesis of great earthquakes and hypothesis of resonance are correct and appropriate. The data used are those in ten to twenty years before the earthquake and the result is very difficultly obtained. In practical application of the prediction methods, I have made a prediction on Aug. 29, 1996 and, as a result, two strong (great) earthquakes occurred in China in September. The prediction is correct.

(4) Test of the prediction of 20 or more great earthquakes indicates that most of the earthquakes are related with those in adjacent countries. In order to predict future earthquakes in China, in addition to the study of movement of great earthquakes in China, we must study the data of earthquakes in adjacent countries, so that we may not miss prediction of great earthquake migration from adjacent countries and occurring in China. Since it needs to study earthquakes occurring abroad, we must also study the data of great earthquakes in the world, process a large amount of data of strong (great) earthquakes, and compile maps of global and regional distribution of earthquake epicenters on different scales, and hence new and sophisticated techniques, certain manpower, and financial resources are needed. With developing research and further making earthquake prediction, the more support (mainly financial support) and helps are needed from the parties concerned.

References

Zheng Wenzhen (1997), Study on the Genesis and Occurrence of Great Earthquakes and Their Prediction.*Marine Science Bulletin.* Vol.16, No.1, 39—44

Zheng Wenzhen (1999), Verification of the Resonance Prediction Method for Great Earthquake Motion and its Prediction. *Marine Science Bulletin*, Vol. 18, No.1, 52—57

Analysis of Climate and Sea Ice Characteristic for the Bohai Sea in 1998/1999

Meng Shang (孟 上) Li Hai (李 海)
(*National Marine Environment Forecast Center, Beijing* 100081)

Abstract The cold air processes and the climate characters of this winter in the Bohai Sea are summarized in this paper on the statistic analysis basis of the climate data and sea ice situation in the winter of 1998/1999 and combining the history data of temperature and air pressure fields. The main changing processes of sea ice are also given in this paper. Lastly, this year is determined to be the warmest year in this century in the Bohai Sea and the ice condition belongs to mild ice year.

Keywords The Bohai Sea; atmosphere current; cold air; sea ice

Introduction

Every winter the air temperature of the Bohai Sea and the sea ice caused by it are cared not only by the oceangrapher but also by the people who navigate and work on the Bohai Sea. According to the data analysis, the winter of 1998/1999 is the 13th sequential warm winter since the winter of 1986 to 1987. This winter is warmer and the sea ice is lighter compared with the warmest winter of sequential twelve warm winters before this winter, the winter of 1988 to 1989, and it is even the warmest winter since Dalian station was established in 1905. Under the abnormal warm situation encountered only once every century, it is necessary to summarize what the way of sea ice freezing up and evolving is, how long the effect time of sea ice is in the Bohai Sea, how big the extent of the effect is, and what causes the climate situation encountered only once every century.

In this paper, we try to illustrate the whole changing process of the sea ice in the Bohai Sea encountered only once every century through the evolution of atmospheric current and the climate condition.

1 Synopsis of the Climate and Cold Air Processes in the Bohai Sea in the Winter of 1998/1999

There were fourteen normal intensity cold airs, twice middle to strong cold airs, four severe cold airs and twice cold waves in the Bohai Sea from November, 1998 to February, 1999. The time and intensity of the cold airs affecting the sea area are given in table 1. Table 1 shows the most times and

the strongest cold air, including the only two cold waves in this winter which occurred in November, and this provides an advantageous situation for the formation and evolution of sea ice.

Table 1 The statistics of the time and intensity of the effect of the cold airs from November, 1998 to February, 1999*

Month	The date and intensity of the cold air														Total			
	D	I	D	I	D	I	D	I	D	I	D	I	D	I	M	L	S	C
11	4	S	6	M	8	M	15	C	21	L	27	M	30	C	3	1	1	2
12	4	L	7	M	14	M	18	M	22	M	28	S			4	1	1	
1	5	S	19	M	25	M	29	M							3		1	
2	2	M	9	M	11	M	17	S	26	L					3	1	1	

*" D" denotes date;" I" denotes intensity;" M" denotes middle;" L" denotes less strong;" S" denotes strong; "C" denotes cold wave

The total times of cold air from October to February this winter above middle intensity is more than the normal year compared with the data of the same time in history, and the anomaly is 0.9. After classified calculation , the times of cold air above middle to strong intensity are obviously less, the negative anomaly is less by -5.6. The monthly average air temperature, anomaly and the standard deviation from November to February in the winter of Dalian are given in Table 2. This table shows that all the other months have an obvious positive anomaly except that the November is a normal year with zero anomaly. It can be determined that December is high obviously, January and February are high abnormally through the relation of anomaly and standard deviation ($\triangle T \geqslant 2\sigma$ is high abnormally, $\triangle T \geqslant 1.5\sigma$ is high obviously). It is one of the reasons for the warmer climate in this year that the times of the process of strong cold air are too less and that the air temperature is high obviously in the Bohai Sea.

Table 2 The monthly average air temperature, anomaly and the standard deviation in the winter of Dalian

Month	Average air Temperature $\overline{T}$	Anomaly $\triangle T$	Standard deviation σ	Relation	Conclusion
Nov.	5.9℃	0.0℃	1.5	$-\sigma \leqslant \triangle T \leqslant \sigma$	Normal
Dec.	1.5℃	2.6℃	1.6	$\triangle T \geqslant 1.5\sigma$	High obviously
Jan.	-0.9℃	3.7℃	1.7	$\triangle T \geqslant 2\sigma$	High abnormally
Feb.	0.5℃	3.6℃	1.8	$\triangle T \geqslant 2\sigma$	High abnormally

2 The Basic Sea Ice Condition in the Winter of 1998/1999 in the Bohai Sea

For analyzing the typical process of the sea ice freezing and breaking up of this winter, the temperature of Dalian station (Fig. 1) in combination the process of cold air is taken as index. There are three times of sea ice freezing up and breaking up process in this winter through the analysis of the daily ice graph and the weather chart, occuring in the freezing up period, the severe ice period and the breaking up period respectively.

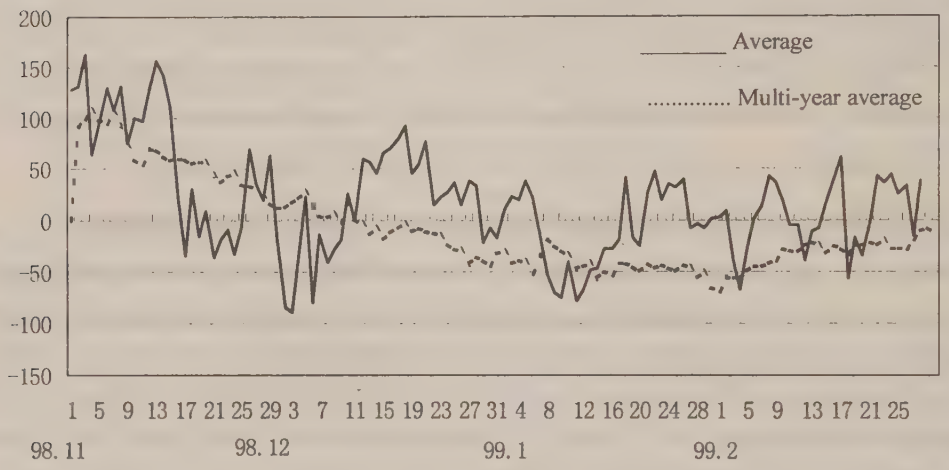

Fig. 1 The daily and multi-year average air temperature in Dalian from November 1998 to February 1999

The first process occurs in the sea ice freezing up period. Because of the effect of the cold wave process in the late middle ten days of November, there are strong winds and the air temperature drops obviously in the Bohai Sea. The air temperature of Dalian drops -13 ℃ suddenly in 24 hours on 16 November, and the range of the drop in the air temperature reaches -23 ℃ in this whole cold wave process. The average air temperature of Dalian is -3.5℃ on 17, November, the lowest air temperature reaches -7℃ on 18. It can be seen from the 500hPa chart on November 14 (Fig. 2a) that the polar eddy breaks up and the polar region is controlled by the high pressure.

The polar eddy of east Asia bursts toward south and the zonal circulation is very obvious. With the development of the ridge of high pressure to the east of Ural Mountain, the meridional circulation increases at the middle and high latitude of the Asia, and a type of one trough and one ridge forms in east Asia on November 16 (Fig. 2b). With the development of the trough of long wave, there are cold airs that move downwards to the south continually from the northeast cold eddy, thus making the air temperature keep low continually in the Bohai Sea. All of these provide the basic condition for the

forming of the sea ice in the period of the beginning of the ice. There is another Siberian cold air moving toward the east and downward to the south on November 21, so that there is another less strong intensity cold air process and there is little to middle snow, and severe snow in some parts of the area. Under the action of this situation, the average air temperature of Dalian is bellow the zero centigrade from 21 to 25, November, and the ice appears in the north of the Liaodong Bay. For example the date of the beginning of the ice is 25, November.

With the adjustment of the situation of upper-air circulation, the polar high collapses and moves downward south, new cold airs add to the northeast cold eddy constantly, and a new process of cold air is brewing. The second cold wave of this winter breaks out finally on 30, November with the continual change of the long wave. The range of the drop in the air temperature is -20℃ in this cold air process, the lowest air temperature is -11℃ in Dalian on 2 December. The average air temperature that day is -9℃ only, the highest air temperature is -6℃ only. It is the coldest day of this winter. Under this condition, ice first appears also Qinhuangdao, and at the same time the sea ice develops very fast in the Liaodong Bay.

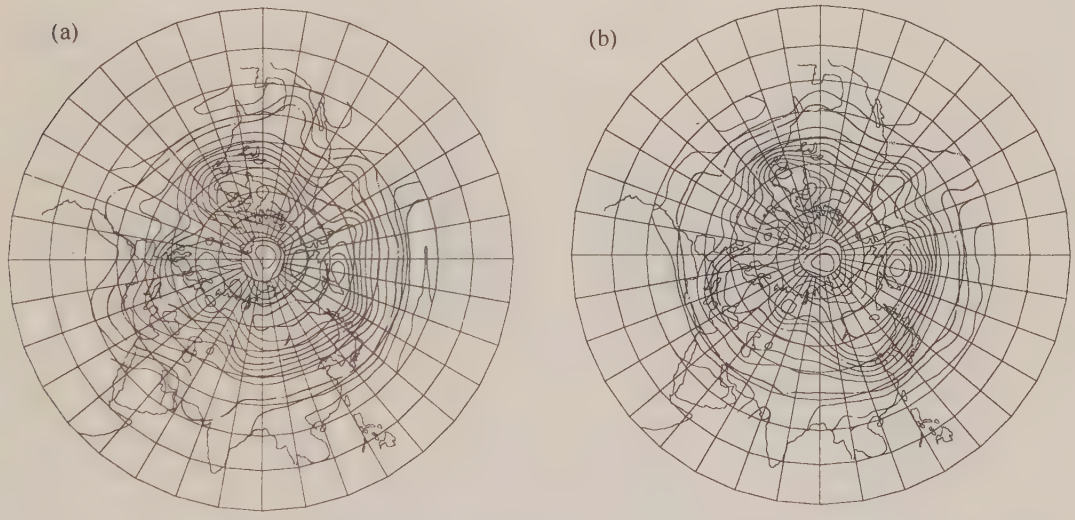

Fig. 2 (a)500hPa circulation situation graph on 14 November, 1998,
(b)500hPa circulation situation graph on 16 November, 1998

In December, the situation of upper-air circulation becomes one trough and one ridge type at the middle and high latitudes of Asia and Europe. Europe is the long wave ridge. There is a wide long wave trough from Ural mountain to east Siberia, which rotates with the axis of Europe ridge and makes the low pressure trough of the Siberian become a latitudinal trough from the northeast to the southwest. With the development of the unstable little trough of Sindi island, the latitudinal trough turns to longitudinal and makes the west cold air invade the west area of our nation. At the same time, the part behind east Siberia low trough moves downwards and makes the east cold air affect our nation. Thus the cold air becomes strong after the two cold airs combine (Fig. 3). It prevents the cold air from

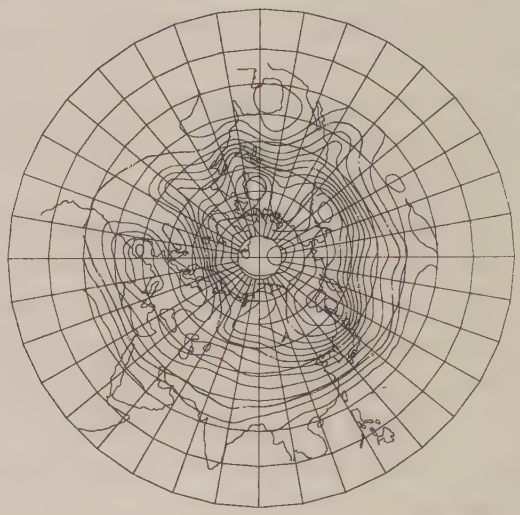

Fig. 3 500hPa current situation graph on 1 December, 1998

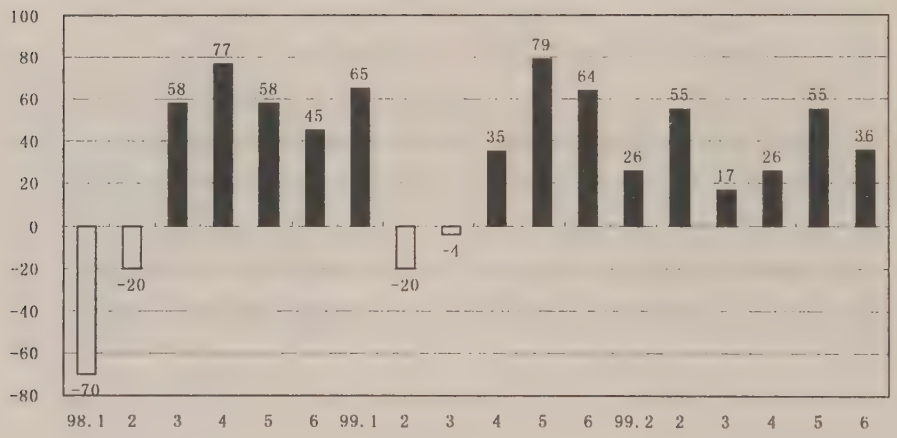

Fig. 4 The anomaly graph of five-day average air temperature of Dalian from December 1998 to February 1999

moving toward south largely due to the existance of the westerly jet at the high altitude of the 500hPa, so the air temperature drops continually through the diffusion in the middle and low layers. Affected by another less strong cold air in the area of the Bohai Sea on 4, December, the air temperature of Dalian drops 12℃ in one day. The highest air temperature is -7℃ only on 5, December, the average air temperature of this day is -8℃, which is the second lowest value of this winter. The sea ice of this winter is becoming stable under this situation. The graph of daily average air temperature of Dalian (Fig. 1) shows that the average air temperature in one day from 1 December to 12 December is below the multi-year average, and that a large negative anomaly exists. The average anomaly graph in ten

days (Fig. 4) shows that the negative anomaly reaches -7℃ in the first five days of December and -2℃ in the second five days of December. Therefore, the range of ice extends continually in this period. The maximum edge of the fast ice reaches 28nm and the maximum level ice thickness is 5cm on 5 December (Fig. 5). The ice area less than 10cm is 2592 km^2 on 5 December, it reaches 4128km^2 on 9 December, and the level ice thickness increases to 6cm. So far the sea ice in the Bohai Sea has initially been formed.

With the change of the upper-air climate situation , the intensity of cold air weakens obviously, and the air temperature increases sharply. Under this situation, the development of ice is inhibited and the extent of ice reduces. There exists a large positive value of the anomaly in sequential five five-days since the middle ten days of December (Fig. 4). The air temperature anomaly keeps above 10℃ from 15 December to 18 December, and the daily average air temperature reaches 7—9℃. This situation makes the sea ice formed in the beginning of the ice melts almost wholly. Though there is another stronger cold air at the end of December, the sea ice does not evolve obviously because of the high basic temperature.

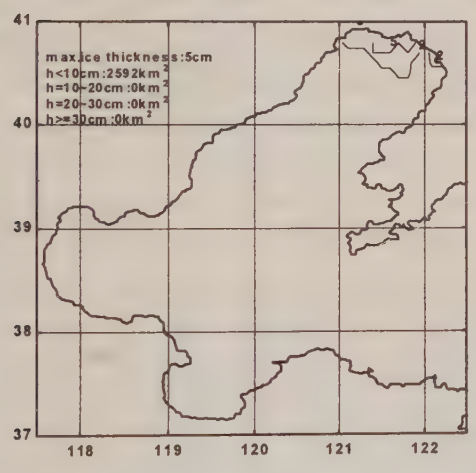

Fig. 5 Sea ice condition on 5 December, 1998

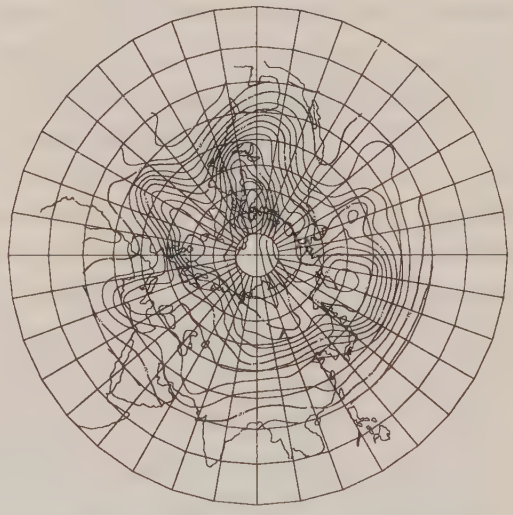

Fig. 6 Current situation graph of 500hPa on 4 January, 1999

January is the coldest period in one year and also the period of development of sea ice abruptly. From the 500hPa high altitude graph on 4 January (Fig. 6), it can be seen that the polar eddy splits again, polar high pressure has the trend to pass through and the strong cold air begins to move toward south on a large scale. The strong cold air affects the Bohai Sea on 5 January. Another northeast low eddy forms in the high altitude and the air temperature begins to drop continually from 6 January to 9 January. Though this cold air is strong, the air temperature does not reach the lowest value appearing at the beginning of last December because of the abnormally warm weather in the early days. Even so, the daily average air temperature of Dalian is bellow zero in the sequential ten days and there are six days when the anomaly is negative , and thus the sea ice develops very fast again. The maximum edge of fast

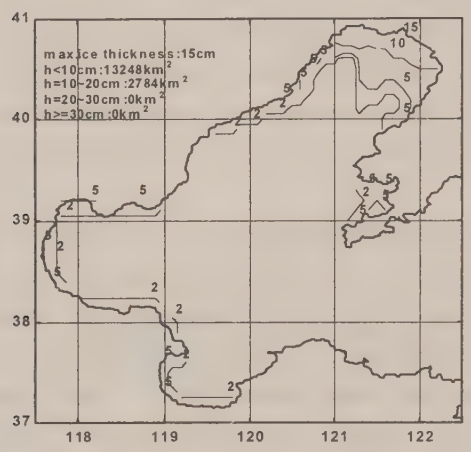

Fig. 7 Sea ice condition on 16 January, 1999

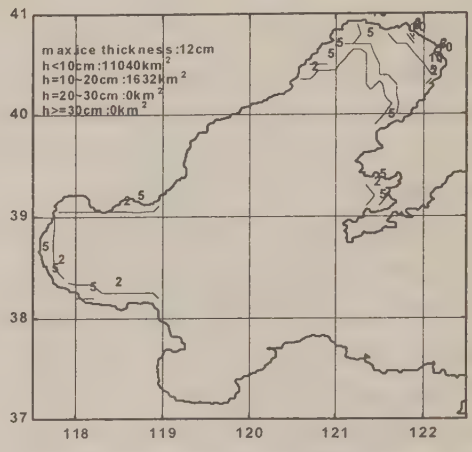

Fig. 8 Sea ice condition on 19 February, 1999

ice is 20nm or so on 5 January, the ice area with the ice thickness less than 10 cm is 3456 km^2, and the maximum ice thickness is 9cm. The edge of sea ice reaches 36 km swiftly on 6 January, 40nm on 10, January and 45nm on 11 January. The maximum level ice thickness reaches 12cm, the sea ice area that the ice thickness is less than 10cm reaches 8832km^2, the area with the ice thickness is between 10cm to 20cm is 2496km^2. The sea ice begins to appear and involve in Tanggu of Bohai Bay and in Laizhou Bay on 8 , January, but the edge of ice is less than 10nm. The ice area enlarges continually on 12 January, the maximum level ice thickness reaches 15cm on 16 January. The sea ice area with ice thickness is less than 10cm is 13248km^2, the maximum edge of ice reaches 58nm, the area that the ice thickness is between 10cm to 20cm is 2784km^2 (Fig. 7). In this period, the maximum edge, the ice area and the ice thickness all reach their maximum values, it is in the severe ice period of this winter. After 18, January, the edge of sea ice begins to recoil. There is no obvious process of cold air in about one month from the middle ten days of January to the beginning of the middle ten days of February, so the air temperature increases obviously. The ice area is only about 1728 km^2 around 26 , January, the ice thickness is 9cm, the edge of fast ice is less than 20nm. With the coming of a middle strong cold air process at the beginning of February, the sea ice develops again. The ice edge increases to 50nm, the ice thickness increases to 12cm and the ice area reaches 7392km^2. But because there is no other cold air following, the ice begins to melt soon, and the change of the edge of fast ice turns clockwise, which is a sign of the period of melting. The ice along the coast and in the west of Liaodong Bay melts soon. There is almost no any ice to the west of 121.4° E in the Liaodong Bay on 14 , February. But with the adjustment of the situation of atmospheric circulation again, the high pressure ridge of Ural mountain develops and moves toward east, which makes the big trough in east Asia deepen again. The strong cold air attacks the area of the Bohai Sea on 17, February. The air temperature of Dalian drops -14℃ abruptly, the daily average air temperature has -3℃ negative anomaly again on 18 February, reaching 5.7℃. The ice area is more than 10 thousand km^2 again on 19, reaching 11040km^2, the ice area with the ice thickness between 10cm to 20cm reaches 1632km^2 (Fig. 8). It is the second largest value of this year. Hereafter, the sea ice melts swiftly with the air temperature rising rapidly again. There is almost

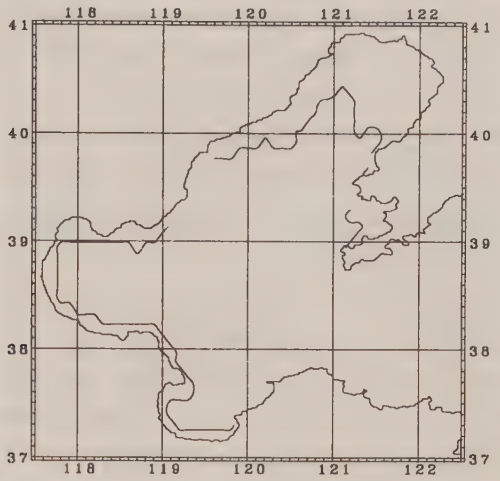

Fig. 9 The maximum ice edge in the winter of 1998/1999

no ice in the Bohai Sea till 26 February. The ice ends on 1 March in Bayuquan, indicating the end of the ice of this year. So, the refreezing phenomenon in the ice-melting period is one of the obvious ice characters this year.

Altogether, the sea ice is very mild in this winter, and the maximum ice edge leaving the bottom of the Bay is about 60nm in the most server period of sea ice (Fig. 9). The ice in other sea areas of the Bohai Sea is in the range of Grade I except that in the Liaodong Bay is between Grade I and II .

3 Discussion

A new La Nina process forms on the east equatorial Pacific since October, 1998. In general, the air temperature in China , especially in the middle and high latitude areas is lower in the period of La Nina, but the area of the Bohai Sea keeps warm in the three months of the winter of 1998/1999. Taking Dalian for an example, the monthly average anomaly of air temperature in Dalian is 2.5℃, 3.7℃ and 3.6℃ separately from December, 1998 to February, 1999. The three-month average anomaly reaches 3.3℃, 0.9℃ higher than that in the warmest year since liberation, 1988/1989 (the average anomaly is 2.4℃), and it is also the warmest year since Dalian station was established in 1905. It is an abnormal warm year that can only be met once every 100 years.

The reason that makes the climate abnormal is very complex. It is a synthetical result of all kinds of climate factors that affect each other. With the increasing discharge of CO_2 induced by human activity, the effect of greenhouse is reinforced; the effect of the solar short-wave radiation on earth is becoming severer and severer due to the destruction of the ozone. At the same time, the earth is in the ascending period of warm half cycle of the super long quasi-period change now, though Lanina phenomena is coming, the cooling effect brought by La Nina can nott counteract the warming effect caused by these super long period change mentioned above. This is the main reason why this winter is abnormal warm.

From the change of atmospheric circulation, it can be seen that the areas south of 60° N and the

middle to high latitude in Asia from 60° E to 120° E are controlled by a huge positive anomaly in the 500hPa month average altitude anomaly field of every month in this winter. The center of positive anomaly above 8 geopotential ten meters covers the area of middle Asia in December 1998 (Fig. 10). Especially the wide areas from Siberia to middle Siberia are controlled by the area of positive anomaly whose center is 20 geopotential ten meters high in February, 1999 (Fig. 11). This situation is not so obvious as that in above two months in January 1999, but the basic situation that Asia is controlled by positive anomaly does not change. This out-of-phase situation is very rare compared with the distribution of the trough and the ridge in the normal situation. Because the high pressure ridge belonging to the super long-wave exists in the continent of Asia chronically, it forces the big trough of east Asia to move from the stable area near 120° E to the high altitude over the sea of Japan. This is the direct reason that makes the air temperature in China especially that in the Bohai Sea located the middle to high latitude abnormal warm.

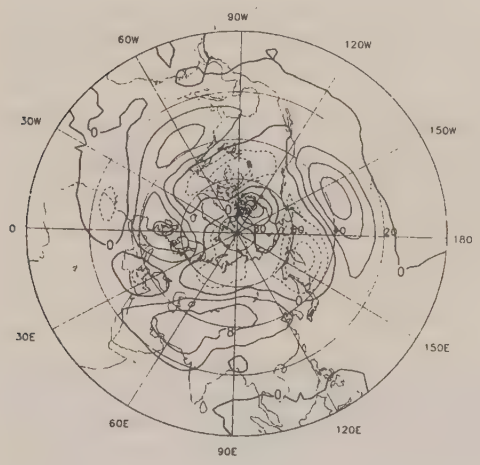

Fig. 10 500hPa monthly average anomaly of north sphere in December 1998

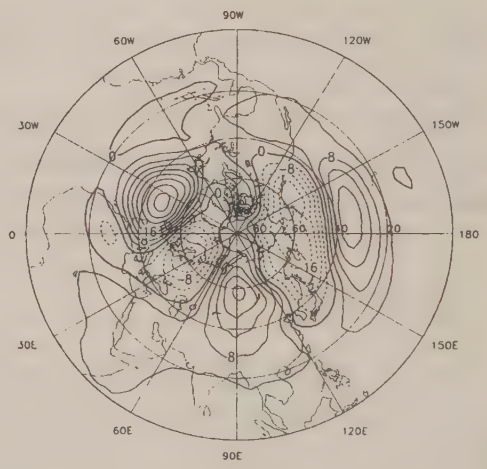

Fig. 11 500hPa monthly average anomaly of north sphere in February 1999

Under the above background of the climate, the sea ice of this winter has the characters as bellow:

1) The period of first ice is near to normal year, but the tendency of ice development is very violent in this period.

2) The period of the ending of ice is consideably in advance. Among the stations, the breaking-up date of Bayuquan is 21 days and Tanggu 28 days ahead of time.

3) The whole ice period can be divided into three major stages, and there is an obvious process of development and melting in every stage. This kind of process of development and melting conforms to the cooling and warming process of the climate in this winter. Because the cool and warm alternation is obvious and the time of warming process is longer than normal time, the sea ice of this winter can not get development enough. So not only the extent of the sea ice of this winter in the Bohai Sea is small but also the maximum level ice thickness is 15cm only. It is obviously a mild ice year .

Reference

1 Wang S W et al., (1995). The analysis on global warming in the recent one hundred years. Atmosphere Science, 19(5)

2 Tang G L et al., The air temperature series and its changing trend from 1921 to 1990 in China, Meteorological, 18(7)

Scouring and Accretion Characteristics and Their Causes in the Qiqu Archipelago Over the Past Century

Chen Shenliang (陈沈良)
(*State Key Laboratory of Estuarine and Coastal Research, East China Normal University, Shanghai 200062*)

Abstract The sea area of the Qiqu Archipelago shows accretion trends with the rate of 2.3cm/a within the last 100 years. However, different processes existed in various periods. This paper examines scouring/accretion processes based on sea charts and their causes, combined with hydrodynamics and sediment samples, as well as the river channel evolution of the Changjiang Estuary. The results suggest that the scouring/accretion processes for the entire sea area of the Qiqu Archipelago are controlled by the river channel evolution of the Changjiang Estuary. The scouring along the strait channel area is related to hydrodynamics and sediments and their strait channel effects.

Keywords scouring/accretion evolution; strait-channel effect; river channel evolution; the Qiqu Archipelago

1 Study Area

The Qiqu Archipelago is situated in the northern part of the mouth of Hangzhou Bay, and is connected with the Changjiang Estuary and its offshore area. The Archipelago is composed of the north (mainly Xiaoyangshan Island) and south (mainly Dayangshan Island) island chains (Fig.1) with 69 various sized islands and 10.72 km^2 in area, which are the islands nearest to Shanghai City. The bathygraphical condition of the sea area is good for construct the offshore deepwater harbor near Shanghai [1]. The waters between the north and south island chains forms obvious strait-channel features, and thus the scouring or accretion evolution on the sea bottom is influenced by the strait-channel topography. However, because the strait channel is composed of lots of islands, its hydrodynamics and sediments are much more complex than general strait channels, moreover it lies within the sphere of influence of Changjiang Estuary and Hangzhou Bay, being subjected especially to the effects of Changjiang diluted water. Therefore, the sediment dynamics and scour/accretion processes are much more complex and unique.

This paper analyzes the scouring/accretion evolution in the strait channel and adjacent areas and the relationship with hydrodynamics, sediments and their strait-channel effects based on sea charts over the last century and measured hydrologic and sediment data. Furthermore this paper discusses the relationship between the scouring/accretion evolution and river channel processes of the Changjiang Estuary.

The distribution of the Qiqu Archipelago islands is controlled by two groups of structural line, E-W and NWW. The north island chain is arranged in the southeast, and the south island chain line is arranged from west to east. The topography of each island undulates, ranging between 100 and 200 m in height, and only in Dayangshan Island the maximum height is 204m above MSL. The shallow stratum in the strait channel is composed of dust-colored silty clay with a thickness of 10 to15 m. The bottom materials in the strait channel are coarse due to tidal scouring and wave actions.

The main subaqueous topography of the adjacent Archipelago area is the foreslope of the Changjiang submerged delta. The area between the north and the south island chains forms a deep tidal channel due to geological boundaries and hydrodynamic actions. The strait-channel area gradually broadens from east to west from about 1 km to 6 km, and forms a trump-like mouth at the western part. Generally , the depth of Hangzhou Bay mouth is only 8 to 9 m. However, the Qiqu Archipelago and its adjacent continental shelf form a wide deep-water area. The water depth in most part of the area is over 14 meters, and in the eastern part of the strait channel the depth can reach 30—55 m. In the middle area the water depth can reach 70—80 m with the maximum of 87 m, while in the western part it decreases 20 to 10 m.

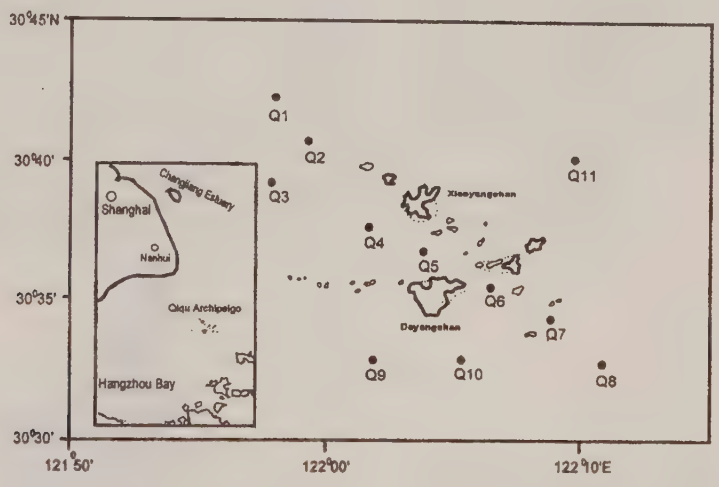

Fig.1 Location of the study area and measurement stations

2 Scouring/Accretion Processes

The contrast of sea charts over the last century was used to analyze the scouring/accretion processes for the Qiqu Archipelago area. The study area is 30° 30' —30° 45'N, 121° 50' — 122° 15' E, and the area is about 1040 km^2.

The results are shown in Table 1 and Fig.2. In the study area, scouring and accretion occur alternately, and as a whole showed accretion trends. The mean accretion rate is 2.3 cm/a over the last 100 years, in which during the first 50 years (1887—1937) the accretion rate is 3.6 cm/a, and during the second 50 years (1837—1987) the accretion rate decreases to 1.0 cm/a. But the study area in various periods showed different scour/accretion processes. During the periods of 1887—1916 and

Table 1 Scouring and accretion evolution over the past century (1887-1987)

Period	Scouring(-)/ Accretion(+) $\times 10^8$ m^3	Annual mean ($\times 10^8$m^3/a)	Rate (cm/a)
1887—1916	-3.40	-0.18	-1.7
1916—1937	+21.98	+1.05	+10.1
1937—1950	+10.22	+0.79	+7.6
1950—1960	+1.29	+0.13	+1.2
1960—1970	-8.47	-0.85	-8.2
1970—1987	+1.96	+0.12	+1.1
Former 50 yrs(1887—1937)	+18.58	+0.37	+3.6
Later 50 yrs(1937—1987)	+5.00	+0.10	+1.0
100 yrs(1887—1987)	+23.57	+0.24	+2.3

1960—1970 scouring occurred. From the 1960s to the 1970s the strongest scouring occurred at the rate of 8.2cm/a. During the period between 1887—1916 the scouring rate was the lowest with only 1.7cm/a, and therefore the sediments fill up intensively with the accretion rate of 10.1cm/a. However, the strait-channel area presented a scour state, though the entire area shows accretion (see Fig.3), which is closely related to the strait-channel effects beside the sediment diffusion path.

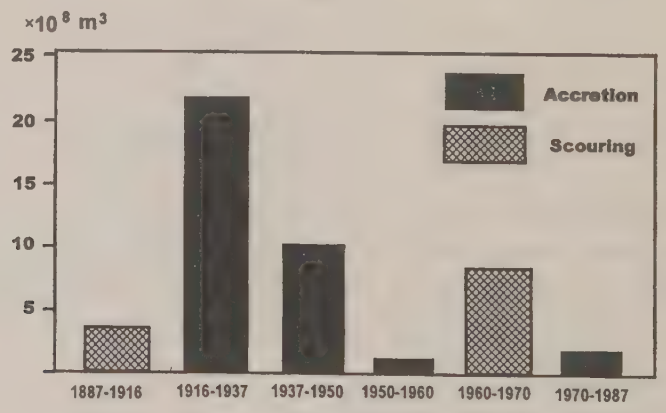

Fig.2 Scouring/accretion volume in the study area over the past century

The special geographical position of the Qiqu Archipelago indicates that its scouring/accretion evolution is related to the hydrodynamics and sediments of the local area as well as the river channel processes of Changjiang Estuary.

3 Hydrodynamics, Sediments and Strait-Channel Effects

3.1 Tidal current and residual current

The current direction in Qiqu Archipelago area is obviously restricted by its strait channel

orientation. The current directions of flood and ebb are about 295° and 115° respectively, consistent with the channel orientation. The tidal current ellipticity is only -0.05— -0.1, which indicates that tidal currents have a distinctive to-and-fro movement. The currents are also particularly strong in the strait channel, for example, the peak tidal current velocity reaches 2.5m/s at the site between the Dayangshan and Xiaoyangshan Island. On the whole, the current velocities in the strait channel gradually increase from east to west.

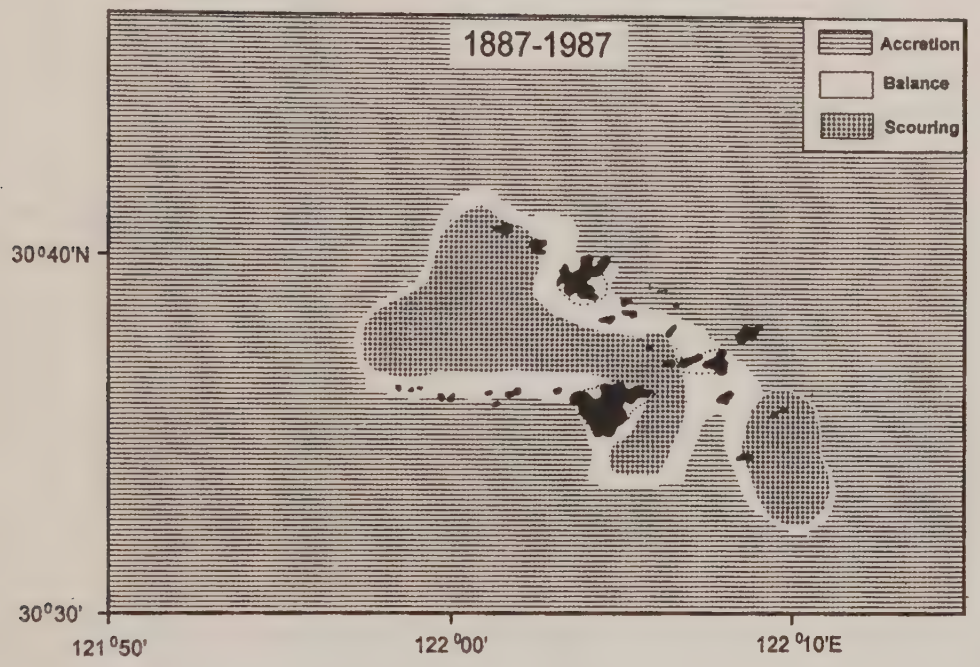

Fig.3 Scouring/accretion distribution of the study area

From the distribution of maximum velocities, the ebb currents are stronger than flood currents (Table 2), and increase in the strait channel. The ebb-flood current ratios obviously increase from the west mouth (Q4) to the east (Q6), increasing from 1.16 to 1.84, whereas from the station Q6 to the east the ratios decrease. From the vertical distribution of current velocities (Fig.4), the upper layer ebb current in the western part of the strait channel (Q4 and Q5) is greater than flood, while the down layer ebb is lower than flood. In the eastern part of the strait channel (Q6 and Q7) the current from surface to bottom is identical, with all ebb currents greater than flood currents. This distribution suggests that the currents in the strait channel are affected by strait-channel bottom topography, which causes obvious diversity of flow movement in the east and west parts.

From the distribution of the vertical mean residual currents during a tidal period (Table 2), it can be seen that the residual currents are strong, most of which are over 10 cm/s, with a maximum of 41cm/s (at Q6). The directions of residual currents in the northern part of study area (Q1, Q2 and Q11) are all southwest, and , to the strait channel and its southern part ,become southeast in a counter clockwise

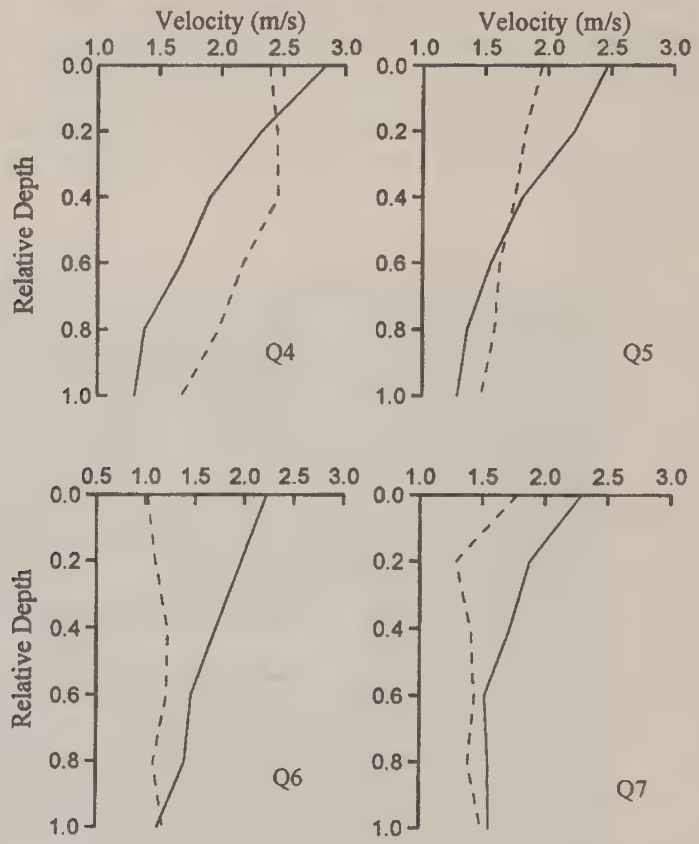

Fig.4 Vertical current distribution within the Strait channel of Qiqu Archipelago
the solid line represents ebb, and dash line represents flood

motion. This distribution characteristic indicates the flow and diffusion direction of Changjiang diluted water. The Changjiang diluted water diffuses southward, its partial water diffuses southeastward out to sea and forms a steady residual current that flows southeasterly in the strait channel and its south sea area. This residual current increases due to strait-channel topography, and it reaches the maximum value at the narrowest site (Station Q6).

Table 2 The ratio velocity of maximum flood and ebb currents and mean residual current in October 1996
Velocity in cm/s, Direction in degree

Station		Q1	Q2	Q3	Q4	Q5	Q6	Q7	Q8	Q9	Q10	Q11
Flood	V	255	228	223	246	195	121	178	229	226	229	255
	D	282	294	261	289	306	258	288	285	280	265	296
Ebb	V	267	267	267	284	247	222	229	265	248	268	309
	D	97	139	109	102	110	110	108	107	109	119	99
Ebb-flood ratio		1.05	1.17	1.20	1.15	1.27	1.84	1.29	1.16	1.10	1.17	1.21
Residual	V	8.2	8.7	10.1	11.5	10.1	41.3	12.4	2.1	11.6	12.8	10.8
	D	200	228	110	121	140	121	132	180	136	137	202

Table 3 Unit width sediment transport and direction for each station

Station	Tidal Pattern	Ebb		Flood		Tidal Period	
		Transport (t/m.d)	D(°)	Transport (t/m.d)	D(°)	Transport (t/m.d)	D(°)
Q1	Spring	1390	99	1079	293	441	60
	Middle	728	97	629	280	107	75
	Neap	123	88	114	288	41	20
Q2	Spring	1756	101	1219	290	586	82
	Middle	1072	109	932	282	181	146
	Neap	157	98	165	283	16	340
Q3	Spring	1752	106	1464	290	305	89
	Middle	1475	97	1409	281	108	47
	Neap	250	100	160	284	91	92
Q4	Spring	1926	111	1941	288	101	208
	Middle	1308	109	1474	287	177	267
	Neap	254	107	249	285	8	163
Q5	Spring	1415	115	2183	303	803	316
	Middle	1199	114	1039	296	166	99
	Neap	290	110	289	292	12	24
Q6	Spring	4218	114	1869	288	2367	118
	Middle	5480	117	1193	286	4313	119
	Neap	1184	116	506	261	821	136
Q7	Spring	2365	100	1750	262	869	137
	Middle	1535	103	2091	277	591	260
	Neap	527	96	688	275	161	274
Q8	Spring	953	102	860	277	125	142
	Middle	638	102	1186	282	548	283
	Neap	178	88	191	287	61	355
Q9	Spring	1283	105	1520	283	241	273
	Middle	1296	109	2084	278	850	260
	Neap	177	100	223	278	47	267
Q10	Spring	1523	105	1694	280	233	239
	Middle	1384	107	1911	278	578	256
	Neap	123	105	100	276	28	140
Q11	Spring	880	101	1311	291	467	309
	Middle	592	94	851	289	322	319
	Neap	112	99	145	285	36	306

3.2 Suspended sediment concentration

The suspended sediment concentration (SSC) is a strongly random variable, and it is affected by a good many factors such as different periods (i.e. wet/dry season, neap/spring tide), and current velocity,

waves, sediment source, seabed topography, etc[2]. Measured data shows that the SSC is high in the western part and low in the eastern part, and the highest SSC occurs at the west mouth of the strait channel (Fig.5). In the eastern part of the strait channel, the SSC contour shows north-south orientation, which indicates that the Changjiang diluted water diffuses northwestward under the action of northwesterly flood currents.

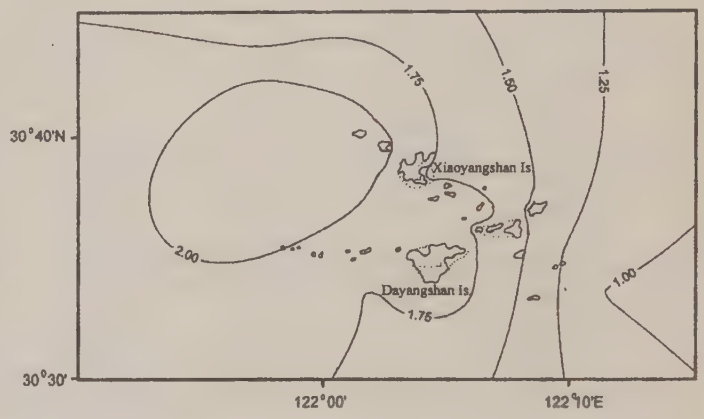

Fig.5 SSC distribution in the sea area of Qiqu Archipelago

In other words, although the SSC is high in the strait-channel area, the strait channel keeps significant water depth because of the strait-channel effects.

3.3 Sediment source and transport

The Quqi Archipelago lies within the diffusion reach of the sediments carried by Changjiang diluted water, so the sediment source is directly the diffused sediments from the Changjiang Estuary, and the sediments carried by tidal currents the latter of which also comes from the Changjiang Estuary. Because the Jiangsu-Zhejiang Coastal Current and the Taiwan Warm Current seasonally change, the result is that the diluted water from the Changjiang Estuary also presents a seasonal swing (i.e. during summer months it deflects toward the east and during winter months it disperses toward the southeast). Consequently, the sediments entering the Qiqu Archipelago area during the summer are significantly less than that during the winter. Therefore, measured SSC data during the winter and the summer suggest that the large-scale sediment distribution is due to the seasonal variation characteristics mentioned above.

According to the calculation results of unit-width sediment transport (Table 3), net sediment transport is larger during spring than during middle tide, and larger during middle tide than during neap, which indicates that the sediment transport is predominantly caused by tidal currents. The maximum sediment transports during spring, middle or neap all occur at the narrowest site of the strait channel (Station Q6), and their directions are all southeastward. During spring, sediment transports at the east and west mouth of the strait channel show obvious diversities. At the east mouth, sediments are greatly transported southeastward, and at the west mouth, a few sediments are transported westward. This reflects the strait-channel effect on the suspended sediment transport.

3.4 Bottom sediments

The sea area of Qiqu Archipelago, in fact, is the fore-slope of Changjiang submerged delta, so the

bottom sediments are fine grained. The type distribution of bottom sediments (Fig.6) shows that most are fine-grained sediments. The clays usually distribute in the area furthest from islands. These are the deposits under a relatively weak environment. The coarser sediments, such as silty sand and fine sand, occur in the areas closer to the islands, especially in the west mouth of the strait channel, in which there is a large quantity of coarse-grained sediments (which are related to strong bottom currents during flood tide). The coarse sediments transport and deposit westward under strong bottom currents.

In summary, the SSC is high in the strait channel (under the effects of unique hydrodynamics and strait-channel topography), the sediment deposits are significantly low, and the water depths stay relatively constant.

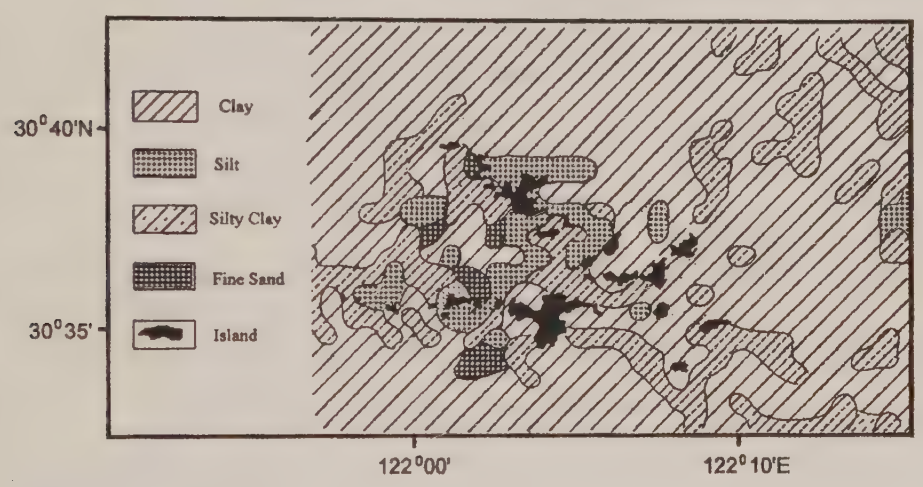

Fig. 6 Bottom sediment distribution in the study area

4 River Channel Evolution in Changjiang Estuary

As mentioned above, the suspended matter from the Changjiang Estuary represents an important source of the Qiqu Archipelago waters. Thus the scouring/accretion evolutions in the area are closely related to the river channel processes of Changjiang Estuary and the diffusion paths of the diluted water.

The diffusion reach of Changjiang diluted water is controlled by the outflow path. The outflow channel shows multi-level bifurcation channels, and its main stream changes frequently. In different channels, the water and sediment discharge and their outflow direction change frequently, which lead to scouring-accretion alternation in the Estuary and its offshore.

Since the 1840s, the main stream of the Changjiang Estuary had ever swayed between the South and North Passages[3]. For instance, in 1842 the main stream flowed out along the South Passage, and during the period of 1860 —1865, the main stream flowed out by the North Passage. In 1927, the main stream flowed by the South Passage again because the upper mouth of the North Passage was blocked,

similarly in 1958 because the upper mouth of the South Passage was blocked, the main stream flowed by the North Passage again. In the late 1940s, a new channel in the down stream of the South Passage was formed between Juduansha and Hensha Bank, and as a result, the South Passage was divided into the South Channel and the North Channel (Fig.7). Since 1960s, with the expansion of theNorth Channel , the North Channel has become a new main stream.

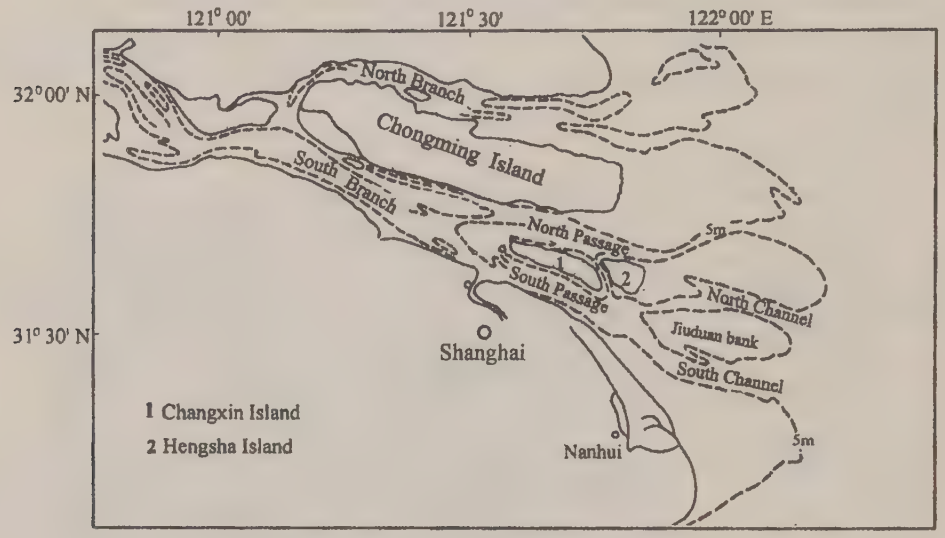

Fig. 7 The bifurcation channels of the Changjiang Estuary

The shift of the main stream resulted in a flow direction alternation. Before the 1960s, the main stream flowed out along the South Channel southeastwardly. A large quantity of sediments entered Hangzhou Bay and became the main sediment source of the study area. But after the 1960s, the main stream flowed out along the North Channel, also the outflow sediments entering Hangzhou Bay decreased. Consequently, the study area became scoured.

It can be concluded that when the main stream flowed through the South Channel, sediments from the Changjiang Estuary increased and the study area became accretion. Likewise, when the main stream flows along the North Channel, the sediment source of the study area decreased and the area became scouring. Therefore, the scouring/accretion processes in the sea area of the Qiqu Archipelago is consistent with the river channel evolution of the Changjiang Estuary, which suggests that the river channel processes and the corresponding sediment diffusion paths dominate the scouring/accretion processes of the Qiqu Archipelago area.

5 Conclusion

The water area between the south and north island chains of the Qiqu Archipelago is obviously affected by a strait channel. The hydrodynamic and sediment characteristics there are not only affected by the Changjiang Estuary, but also dominated by the local strait-channel topography. The current

structure and the distribution of SSC and bottom sediments all demonstrate obvious strait-channel effects.

As a whole, the entire study area presents accretion for the recent century, while the strait-channel area shows scouring. Under the effects of the strait channel, suspended sediments settle loosely to the bottom. Although the SSC is high, the water depth keeps well due to the strait-channel effects.

The scouring-accretion alternation in the Qiqu Archipelago area is consistent with the river channel processes of the Changjiang Estuary, which suggests that the river channel evolution and its induced sediment dispersion path have changed the scouring/accretion processes of the Qiqu Archipelago area.

In summary, the scouring in the strait channel is due to the special hydrodynamics of the strait channel, and the scouring/accretion distribution characteristics reflect the strait-channel effects, while the entire scouring/accretion changes are controlled by the river channel processes of the Changjiang Estuary.

References

1 Chen Shenliang and Wang Baocan, (1999). A primary study on the Yangshan harbor and waterway. The fifth Symposium on China Maritime Affairs, Oceanic Press, Beijing, 285—291

2 Gu Guochuan, (1987). Hydrodynamic and sediment characteristics of north coast of Hangzhou Bay. Dohai Marine Science, 5(4): 13—19

3 Chen Jiyu, Pan Ding-an, Su Fachong, et al.,(1988). An analysis of evolution of North Channel in the Changjiang Estuary. Processes of Dynamics and Geomorphology of the Changjiang Estuary. Shanghai Scientific and Technical Publishers, Shanghai. 390—403

Chemical Oceanography of Nutrient Elements in the Bohai Sea, Yellow Sea and East China Sea

Liu Sumei (刘素美)[1] Zhang Jing (张经)[1,2]
(1 College of Chemistry and Chemical Engineering, Ocean University of Qingdao, Qingdao 266003)
(2 State Key Laboratory of Estuarine and Coastal Research, East China Normal University, Shanghai 200062)

Abstract Data of nutrient elements are available from published references to allow the synthesis of nutrients characteristics in the Bohai Sea, Yellow Sea and East China Sea. The concentrations of nutrient elements and pathways via rivers, atmosphere and sediment are discussed.

Keywords Bohai Sea; Yellow Sea and East China Sea; nutrient elements; chemical oceanography

Introduction

The Bohai Sea , Yellow Sea and East China Sea are shallow continental shelf region with a total surface area of 1.2×10^6 km^2. The average water depths for the Bohai Sea, Yellow Sea and East China Sea are 18, 45 and 349 m, respectively. The complicated current system in the Bohai, Yellow Sea and East China Sea is driven by the northern branch of Kuroshio and the Yellow Sea Warm Current northward, the Yellow Sea Coast Current and the East China Sea winter Coast Current (Fig. 1) (Zheng et al., 1998). Many rivers (e.g. Huanghe, Yalujiang, Changjiang etc.) transport large amount of water and suspended matter from the continent into the Bohai Sea, Yellow Sea and East China Sea. Dust and soil particles from Northeast Asia are transported to the Bohai Sea, Yellow Sea and East China Sea via atmosphere and deposit to the sea surface. The rainfall is 1000—2000 mm in the East China Sea, 600 mm in the Bohai Sea and 600 — 800 mm in the Yellow Sea. The circulation, upwelling, riverine transport and atmospheric deposition carry nutrient elements to the surface water of the Bohai Sea, Yellow Sea and East China Sea. This paper is focused on description of the chemical oceanography of nutrient elements in the Bohai Sea, Yellow Sea and East China Sea based on previously published reference materials.

1 Distribution of Nutrient Elements in the Bohai Sea

The nutrient elements in the Bohai Sea have obvious seasonal and regional characters. The

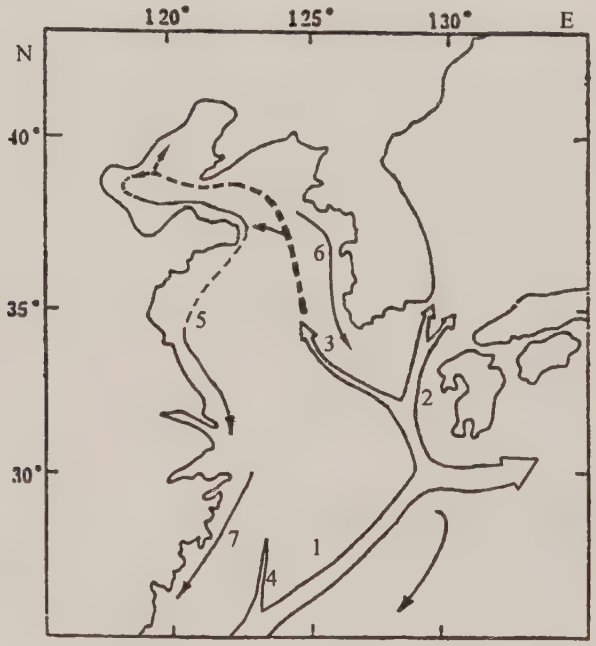

Fig. 1 The current systems in the Bohai, Yellow Sea and East China Sea
1. Kuroshio; 2. Tsushima Warm Current; 3. Yellow Sea Warm Current; 4. Taiwan Warm Current; 5. Yellow Sea Coast Current; 6. West Korea Coast Current; 7 East China Sea Coast Current

concentrations of nutrients, chlorophyll a (Chl-a) and primary production in the Bohai Sea are shown in Table 1. In spring, the distribution of nutrient elements is dominated by the blooming biomass of phytoplankton, which decreases from the north to the south, in accordance with the distribution of chlorophyll and primary production (Table 1). In summer and autumn, the concentrations of nutrient elements are higher near the coast and estuaries than in the Central Bohai Sea as a result of the input of a large amount of freshwater discharge. As the Bohai Sea is shallow, the nutrient concentrations show well-mixing distribution in late autumn, and an increase in nutrients takes place following the reduction of phytoplankton and high mixing. In winter, the nutrient concentrations are high near coast and estuaries, and decrease gradually toward the center of the Bohai Sea, which is related to the intrusion of water mass from the northern Yellow Sea with low concentrations of nutrients. The vertical distributions of nutrients are homogenous as strong mixing of waters (Office of Comprehensive Marine Investigation, 1964). The nutrients in the whole Bohai Sea show the highest level in winter, and the lowest in summer (Cui, 1994). It is shown from the average concentrations of nutrients that the phosphate concentrations in the Bohai Sea Bay are higher than that in the Laizhou Bay and Liaodong Bay (Table 1). The nitrate concentrations are the highest in the Laizhou Bay, followed by those in the Bohai Sea Bay, Laodong Bay. This demonstrates that the Huanghe has an important influence in transporting nutrients to the Bohai Sea, especially for nitrate (Cui et al., 1992).

Among the dissolved inorganic nitrogen species, nitrate accounts for 0.1%—61 %, ammonium represents for 34%—98 %, and nitrite for 1 %—5 % in the Bohai Sea (Diao et al., 1985). The DIN/P ratios are high in winter (DIN/P=10.8—11.6), and low in summer (DIN/P=3.5—5.8). The nutrient ratios have a strong relation with the distribution of phytoplankton (Diao et al., 1985).

Both concentration and relative proportion of nutrients have changed dramatically over the last 20

years. The increase of nitrogen and decrease of phosphate and silicate have led to a higher N/P ratio and a lower Si/N ratio in the Bohai Sea. The situation of nitrogen limiting of primary production in the Central Bohai Sea is gradually changing to limitation of phosphate and silicate. This may be related in part to the decrease of Huanghe discharge. The change in nutrient regimes may limit the growth of diatom and thus promote the development of dinoflagellates, which could be the reason of dinoflagellates red tide occurring in the Bohai Sea (Yu et al., 1999).

Table 1 The concentrations of nutrients (mol/L), Chl a (mg/m^3) and primary production ($mg.C.m^{-2}.d^{-1}$) in the Bohai Sea, Yellow Sea and East China Sea

	Chl a	Primary Production	NO^{3-}	NO^{2-}	NH^{4+}	SiO_3^{2-}	PO_4^{3-}	References
Liaodong Bay	0.5-1.2 (1.0)	55-674 (270)					0.15	Fee et al, 1988a,b; Li et al, 1992; Diao et al, 1985; Cui et al, 1994
Bohai Bay	0.88	50-324 (136)					0.2-7.4	Fee et al, 1988b; Li et al, 1992; Diao et al, 1985; Zou et al., 1985
Laizhou Bay	0.5-3.4 (1.6)	58-840 (394)					0.12	Fee et al, 1988a,b; Li et al, 1992; Diao et al, 1985; Cui et al, 1994
Central Bohai Sea	1.3	98-770 (366)	3.55	0.63	0.82	6.6	0.31	Fee et al, 1988b; Li et al, 1992; Diao et al, 1985; Cui et al,1994; Yu et al., 1999
Whole Bohai Sea	0.2-8.0	90-624 (308)	0.4-3.46 (1.99)	0.06 -0.33	0.4-1.14	8.2-15.4	0.26-1.51 (1.0)	Fee et al, 1988a,b; Diao et al, 1986; Cui et al, 1992
Yellow Sea			0.01-12.8	0.18	0.91	0.05-24.9	0.01-2.17	Chung et al., 1999; Liu et al., 1999
East China Sea		68-1500	6.61	0.19	1.08	15.4	0.11	Bai et al., 1995; Hama et al., 1997

2 Distribution of Nutrient Elements in the Yellow Sea

The nutrient concentrations in the Yellow Sea are shown in Table 1. In spring, the nutrient

concentrations are high in the South Yellow Sea and off the southwestern Korea Peninsula, and decrease rapidly from the south to the northeast and northwest as influence from the Changjiang effluent, front waters of Taiwan Warm Current and the surface runoff of the Korea Peninsula reduce. The nutrient concentrations in the Chengshan Cape are also high due to effluent off the Bohai Sea. The nutrient concentrations in other parts of the Yellow Sea are relatively low owing to the consumption by phytoplankton. Waters with low concentrations of nutrients are transported to the southeast by the Yellow Sea Coast Current in the western Yellow Sea. Vertically, the nutrients in coastal and shallow water areas (depth < 40m) show well-mixing distribution, while stratification takes place in deep waters, with higher levels at near-bottom waters than at surface (Liu et al., 1999; Wang et al., 1998 a, b).

In summer, the Changjiang diluted water turns left and goes northward , the nutrients are transported to the southern part of South Yellow Sea, affecting the southwest coast region, and reach to the Cheju Island. The nutrients in the South Yellow Sea at near-bottom can be affected by Taiwan Warm Current. The lowest nutrient levels in the South Yellow Sea are stretched eastward. The nutrient concentrations to the northwest of Cheju Island are also low. Like in spring, the low nutrient waters are continually transported to the southeast by the Yellow Sea Coast Current. The nutrients accumulate at near-bottom waters to form an important reservoir in the central Yellow Sea (Wang et al., 1998b).

In autumn, the nutrients are the highest in the western part of the South Yellow Sea, and decrease from the south to the north and northeast, followed by the Korea Peninsula, and the northwest of the South Yellow Sea. The distribution of nutrients in horizontal dimension in autumn is similar to that in summer, but the effects from the Changjiang diluted are much weaker than that in summer (Wang et al., 1998b).

In winter, the nutrient concentrations in the southwest of the Yellow Sea are still high (NO_3^- and SiO_3^{2-} may reach 9.3 and 19.1 mol $.L^{-1}$, respectively). The low nutrient levels to the west of the Cheju Island (the concentrations of NO_3^- and SiO_3^{2-} are less than 4 and 6 mol $.L^{-1}$, respectively), are still slightly higher than in the west of the Yellow Sea. This demonstrates the effect of the Yellow Sea Warm Current which is characterized by high temperature, high salinity, low oxygen, high pH and low concentrations of nutrients, as the west of the Cheju Island is the entrance of oceanic water into the Yellow Sea. The nutrient concentrations in the central South Yellow Sea and southwest of the Korea Peninsula are high (the concentrations of NO_3^- and SiO_3^{2-} are higher than 5 and 8 mol $.L^{-1}$, respectively), and the high concentrations stretch northwestward. This illustrates that the nutrients accumulating at near-bottom of the Huanghai cold water are transported to the upper layers as a result of strong mixing and the transport of West Korea Coast Current with high concentrations of nutrients. The nutrient concentrations are relatively high off the Chengshan Cape, and low concentrations are along the west coast. The N/P ratios are 8—22, close to the Redfield ratio. The vertical distributions of nutrients show a pattern of well mixing. The influences of the Yellow Sea Warm Current on the distribution and transport are not obvious in this region (Wang et al., 1998 a, b).

The nutrient concentrations of the Yellow Sea increased from 1985 to 1995, the inorganic nitrogen increased by 657 %, while the inorganic phosphorus have somewhat increased .

3 Distribution of Nutrient Elements in the East China Sea

The concentrations of nutrients and primary production of the East China Sea are shown in Table 1. In spring, coastal cold waters rich in nutrients in the central north of the shelf form and produce a obvious nutrient front as a result of the reduction of the Kuroshio invasion on the shelf. Kuroshio subsurface waters rich in nutrients to the north of Taiwan ascends up to 30m, stretching horizontally on the shelf to the 100m isobath (Lu et al., 1996). Due to the stratification, nutrient concentrations are higher at near-bottom than at surface waters. The Taiwan Warm Current rich in nutrients (the concentrations of NO_3^-, PO_4^{3-} and SiO_3^{2-} are 8, 0.7 and 10 mol $.L^{-1}$, respectively) stretches toward northwest along the shelf to the Changjiang Estuary and mixes with the Changjiang diluted water (Zhang W; 1996).

In summer, two centers with higher concentrations of nutrients are formed, as the Changjiang diluted water stretches toward the east and Kuroshio moves in to the shelf in the north of Taiwan. Waters of the Taiwan Warm Current stretch extensively toward the north, hindering the connection of the northern part with the southern part of the East China Sea. The nutrient fronts occur off Taiwan in the south and the Changjiang Estuary in the north. The nutrients show stratification, that is, land-source nutrients transport at surface, and the Kuroshio subsurface waters rich in nutrients ascend to the 100—200m isobath on the shelf, up to 30 m (Lu et al., 1996).

In autumn, the influence of coastal waters reduces on the shelf. The nutrient concentrations decrease obviously as compared with summer. The nutrient fronts weaken and reduce to the 50—100 m isobath. Low nutrient waters occupy almost all the shelf. Kuroshio subsurface waters moves northward further into the interior of the shelf, but the ascending height decreases (Lu et al., 1996). The vertical distribution of nutrients start to be well mixed, and Kuroshio bottom waters rich in nutrients at near-bottom of the shelf slope ascend (Zhang W., 1996).

In winter, Kuroshio waters reach the farthest end of intrusion into the shelf. The Kuroshio subsurface waters only ascend to the shelf break. Waters on the shelf are vertically well mixed with a well mixed nutrient profile, but horizontally decrease from the coast to the ocean along with the salinity gradient (Lu et al. 1996).

The Taiwan Strait is an important channel of water exchange between the East China Sea and the South China Sea, where two water systems converge. The distributions of nutrients in this region are affected by the coastal water of Zhejiang and Fujian Provinces, warm waters of strait and biological activities (Ji et al., 1990). The Fujian coastal upwelling is an important factor affecting the nutrient distributions in the northern part of the Taiwan Straits. The coastal upwelling is the main nutrient source in this region in summer. The nitrogen and phosphorus transported by the coastal upwelling are 73% and 86%, respectively, of what is required by phytoplankton growth there (Chen et al., 1996)

4 The Nutrient Sources

4.1 River input

Rivers emptying into the Bohai Sea, Yellow Sea and East China Sea are summarized in Table 2. The concentrations of nutrients in river/estuaries emptying into the Bohai Sea, Yellow Sea and East China Sea are shown in Table 3. The concentrations of nutrients in the Huanghe Estuary are much higher than those in the Bohai Sea (Chen et al., 1991). The discharge of Haihe changes seasonally. The pollution in the Haihe Estuary is mainly from organic pollution with frequent HABs (Gu et al., 1988). The Changjiang diluted water deflects to left in summer, to Cheju Island. As a result, the concentrations of nutrients in the southern part of the Yellow Sea increase (Yuan et al., 1993). The phosphate is the main limiting factor for the *Skeletonema costaum* red tide in the Changjiang Estuary in June 1990 (Hong et al., 1994). The Oujiang is enriched in nutrients; the concentrations of phosphorus and silica are much higher than those in the Changjiang and Qiantangjiang River. The Changjiang diluted water affects the nutrients concentrations in the Hangzhou Bay, where the concentration of nutrients are lower than those in the Oujiang Estuary (Zhang, W., 1996). The Yalujiang Estuary has characteristics of high nitrogen and low phosphorus. The dissolved silicon shows conservative distribution. The NO_3^- is mainly affected by freshwater discharge and the source of particles. The PO_4^{3-} and NH_4+ show the highest value in the maximum turbidity zone of the estuary, which is the main source of nutrients for the Yellow Sea (Zhang et al., 1998).

Table 2 The drainage area, discharge and suspended particle matter (SPM) content in the main rivers emptying into the the Bohai Sea, Yellow Sea and East China Sea (Zhang et al., 1994; Hong et al., 1995). K and C mean Korea and China, respectively

River	Sea area	Country	Drainage area (km^2)	Water discharge ($\times 10^9 m^3 y^{-1}$)	SPM ($\times 10^6$ t. y^{-1})
Han	Yellow Sea	K		19.0	18.25
Keum	Yellow Sea	K		7.0	6
Yeongsan	Yellow Sea	K		1.6	
Yalujiang	Yellow Sea	K and C	62630	32.8	1.1
Daliaohe	Yellow Sea	C	27334	9.4	110
Shuangtaizihe	Yellow Sea	C	57104	5.1	9.1
Haihe	Bohai	C	264617		
Luanhe	Bohai	C	54412	4.2	20
Huanghe	Bohai	C	752443	41.0	1100
Changjiang	East China Sea	C	1808500	928.2	500

The concentrations of nutrients in the main Chinese rivers are higher than those in the unpolluted rivers (e.g. Amazon, Zaire, Orinoco), but comparable to the polluted and eutrophic rivers in Europe and North America. This is related to the discharge of domestic sewage and the extensive usage of chemical fertilizer in agriculture over drainage basins (Zhang, 1996).

4.2 Atmospheric deposition

The rainwater rich in nutrients could induce bloom (Paerl, 1985). It is demonstrated that the effect of nutrients from atmospheric deposition on the marine primary production is affected directly by human activities (Zhang, 1994). Two *Chattonella marina* blooms occurred in the north of the Yellow Sea in the middle ten days of August 1993 and 1995. The main reason of these HABs may be that it was raining heavily in all the northern part of the North Yellow Sea at that time, the salinity in the surface water decreased temporarily with the input of rainwater and a large amount of nutrients by the Biliu River, Yalujiang etc (Jiao et al., 1996). The average concentrations of NO_3^-, NO_2^-, NH_4^+, PO_4^{3-} and SiO_3^{2-} in the western part of the Yellow Sea are 0.3—85, 0.11—0.28, 0.5—140, 0.01—10, 3.6—6.0 mol $.L^{-1}$, respectively (Zhang et al., 1998, 1999b), with deposition fluxes of 26.9, 0.57, 79.6, 1.28 and 7.79 mol $m^{-2}d^{-1}$, respectively (Zhang, 1994). The average concentrations of NO_3^-, NH_4^+, PO_4^{3-} and SiO_3^{2-} in the eastern part of the Yellow Sea are 20.5, 55.2, 0.53 and 0.65 mol $.L^{-1}$, respectively, the deposition of atmosphere are 64.9, 179, 1.62 and 2.11mol $m^{-2}d^{-1}$, respectively (Chung et al, 1998). Compared with the river input, the atmospheric deposition can be the main source of nutrients in the Yellow Sea, and the rainwater had higher concentrations of nitrogen and N/P ratio, which is very important for primary production and the biogeochemical cycling of nutrients (Zhang et al., 1999b; Chung et al., 1999). The concentrations of NO_3^-, soluble inorganic and organic phosphorus in aerosol in the East China Sea are 1.6—3.2, 0.32—1.4 and 0.39—1.3mol $.L^{-1}$, which had obvious seasonal variation, and the fluxes into the ocean deposition are 1.56—2.84, 0.29—1.23 and 0.32—1.16 mol $m^{-2}d^{-1}$ (Chen et al., 1992).

Table 3 The nutrient concentrations in the main river/estuary systems emptying into the Bohai Sea, Yellow Sea and East China Sea (mol $.L^{-1}$)

	NO_3^-	NO_2^-	NH_4^+	PO_4^{3-}	SiO_3^{2-}	References
Han	57.9		73.7	10.5	15.8	Hong et al., 1995
Keum	42.9		10			Hong et al., 1995
Yeongsan	43.8		6.25			Hong et al., 1995
Huanghe/	0-149	<0.8		<1.4	1-296	Zhang, 1996;
Yalujiang	310	0.79	8	0.04	168	Zhang, 1996, 1997
Daliaohe	7.5	4.4	12.5	1.71	29.3	Zhang, 1996
Shuangtaizihe	181	0.03	2.1	0.35	109	Zhang et al., 1997,1999a
Haihe Estuary	<113	<79	141	0.65-6.5		Gu et al., 1988
Luanhe	74.2	0.2		0.51	87.2	Zhang, 1996
Changjiang	32.9	0.6	14.6	0.57	95	Zhang, 1996

4.3 The exchange of nutrients between sediment and water

The nutrient regeneration in sediment plays an important role in the budget and dynamics of nutrients in the water column. The regenerated nutrients can be very important for supporting primary production (Friedl et al., 1998; Zabel et al., 1998; Giblin, 1997; Treguer et al., 1995). The benthic fluxes of NH_4^+, NO_3^-, $Si(OH)_4$ in the Changjiang Estuary by *in situ* incubation are -2.6—3.4, -1.4—3.2, 0.13—13.2 103mol $m^{-2}d^{-1}$ (Aller et al, 1985). The exchange fluxes of NH_4^+ and NO_3^- in the

Laizhou Bay, Bohai Sea are $(0.038—3.65)\times10^3$ and$(0.96—2.52)\times10^3$ mol $m^{-2}d^{-1}$ (Liu et al., 1999). The exchange fluxes of NH_4^+, PO_4^{3-}, SiO_3^{2-} by pore water gradient calculations are -3.3—0.19, -1.20—0.1, -325—100 mol $m^{-2}d^{-1}$ in the South Yellow Sea, -34.1—14.2, -0.27—1.9, -20—149mol $m^{-2}d^{-1}$ in the East China Sea, respectively (Song, 1996).

5 The Remaining Questions

A number of scientific researches have been done with focus on sea nutrient concentrations, forms, temporal and spatial distribution, seasonal variation etc in the Bohai Sea, Yellow Sea and East China Sea. However, these studies emphasize the distribution characteristics of nutrients. It should be focused on the processes of nutrient pathways and mechanisms regulating nutrient removal and regeneration, including the exchange at interface (e.g. between the atmosphere and sea, the sediment and water etc.). Only after careful examination of the processes , can the dynamics of nutrients in the Bohai Sea, Yellow Sea and East China Sea be simulated with mathematic and/or numerical models.

References

Aller R C, Mackin J E , Ullman W J and Wang C H et al,(1985) Early chemical diagenesis, sediment-water solute exchange, and storage of reactive organic matter near the mouth of the Changjiang, East China Sea. Continental Shelf Research,4 (1/2): 227—251

Bai H., He M and Hu D et al.,(1995) Cruise/Data Report. F9310 (Oct. 15—28, 1993), F9404 (Apr. 8—30, 1994), F9410 (Oct. 18—Nov. 13, 1994). Program on Material Flux in the East China Sea (MFLECS) Funded by National Natural Science Foundation of China (NSFC), March

Chen L, Yang X and Tang R. ,(1992) The chemical characteristics of aerosols over the Kuroshio area. Essays on the investigation of Kuroshio 4, 295—302

Chen S., W. Ruan..(1996) The chemical features of nitrogen, phosphorus and silica in upwelling area and estimate of transport fluxes in the Taiwan Strait. Acta oceanologica Sinica, 18 (3) : 36—44

Chen S., Gu Y and Liu M et al..(1991) Nutrient distribution at the Huanghe River estuary. Journal of Ocean University of Qingdao,21 (1) : 34—42

Chung C S, Hong G H and Kim S H et al..(1998) Shore based observation on wet deposition of inorganic nutrients in the Korean Yellow Sea coast. The Yellow Sea, 4: 30—39

Chung C. S., G. H. Hong, S. H. Kim, J. K. Park, Y. I. Kim, D. S. Moon, I. K. Bang, B. D. Wang, G. Y. Wang and D. B. Yang. The distributional characteristics and budget of dissolved inorganic nutrients in the Yellow Sea. In: biogeochemical processes in the Bohai Sea and Yellow Sea (G. H. Hong, J. Zhang and C. S. Chung eds.). The Dongjin Publication Association, Seoul, 1999, 41—68

Cui Y., Y. Song, Q. Yang and H. Yu.(1992) A preliminary study on the relationship between phytoplankton and physicochemical factors in Bohai Sea Sea. Marine Environmental Science, 1 (3): 56—59

Cui Y., Q. Yang and Y. Song. (1994) Distribution of phosphate and dissolved oxygen and their relation in the Bohai Sea Sea in summer. Marine Environmental Science, 13 (4): 31—35

Dai M., C. Zhou, T. Gu and X. Xu. (1988)The characteristics of distribution of phosphorus in the Haihe River estuary of the Bohai Sea Bay. Studia Marina Sinica, 29: 57—64

Diao H.(1986) The environmental assessment of temperature, phosphate and silicate on phytoplankton in Bohai Sea Sea water. Transactions of Oceanology and Limnology, 4: 35—39

Diao, H., Z. Shen, X. Liu and J. Lu. (1985)The distribution of inorganic nitrogen in the Bohai Sea Sea. Studia Marina Sinica, 25: 53—63

Fei Z L., X H. Mao, M Y Zhu et al. (1988a)A study on primary production in the Bohai Sea. I. The distribution characteristic and seasonal variation of Chl a. Acta Oceanologica Sinica,10 (1) : 99—106

Fei Z-L., X-H. Mao, M-Y. Zhu, B. Li, B-H. Li, Y-H. Guan, X-S. Zhang, R-H. Lu. (1988b)A study on primary production in the Bohai Sea. II. The primary production and estimate the potential catch availability. Acta Oceanologica Sinica, 10 (4) : 481—489

Friedl G, C Dinkel and B Wehrli.(1998) Benthic fluxes of nutrients in the northwestern Black Sea. Marine Chemistry, 62: 77—88

Giblin A E. (1997)Benthic metabolism and nutrient cycling in Boston Harbor, Massachusetts. Estuaries, 20 (2): 346—364

Gu T., X. Xu, M. Dai and C. Zhou. (1988)Nitrogen migration in the Haihe River mouth area of the Bohai Sea Bay. Studia Marina Sinica, 29: 45—55

Hama T, K H Shin, N Handa. (1997)Spatial variability in the primary productivity in the East China Sea and its adjacent waters. J Oceanogr,53 (1): 41—51

Hong, G. H., S. H. Kim, C. S. Chung and S. J. Pae. (1995)The role of the anthropogenic nutrient input in the carbon fixation of the coastal ocean Yellow Sea: a preliminary study. In: Direct Ocean Disposal of Carbon dioxide, edited by N. Handa and T. Ohsumi, 13—22

Hong, J., X. Huang, X. Jiang and G. Wang.(1994) Analysis of environmental factors during occurrence of*Skeleto nema costaum* red tide in Changjiang River estuary-the nutrient state. Oceanologia et Limnologia Sinica, 25 (2) : 179—184

Ji W., S. Huang. (1990)The variation features of nutrients in the western of the Taiwan Strait. III. Statistical analysis of the phopshate concentrations influenced by the water system mixing and phytoplankton assimilation. Acta Oceanologica Sinica, 12 (4) : 447-454

Jiao X. and H. Guo. (1996)Twice *Chattonella marina* red tide occurred in the north of the Yellow Sea of China. Marine Environmental Science, 15 (3) : 41—45

Li B. And M. Zhu. (1992)The pigment species and distribution characteristics of phytoplankton in autumn in Bohai Sea Sea. Journal of Oceanography of Huanghai &Bohai Sea Seas, 10 (3) : 32—37

Liu, S. M., J. Zhang, Z. G. Yu, H. T. Chen and Q. Z. Yao. (1999) Benthic fluxes of dissolved inorganic nitrogen in the Laizhou Bay, Bohai Sea Sea. Environmental Science,20 (2): 12—16

Liu S. M., H. T. Chen, Q. M. Wu, S. Z. Chen, J. Zhang and G. H. Hong.(1999) N, P and Si compounds in the South Yellow Sea. In: biogeochemical processes in the Bohai Sea and Yellow Sea (G. H. Hong, J. Zhang and C. S. Chung eds.). The Dongjin Publication Association, Seoul, 21—40

Lu S., R. Ge and L. Liu. (1996)The seasonal variation and physical transport of nutrients in the shelf of East China Sea. Acta Oceanologica Sinica,18 (5) : 41—51

Lu X., Zhu C., Zhang, A. and Shi Z. (1985) The characteristics of nutrient distribution in the southwest Bohai Sea Sea and Huanghe River Estuary in summer. Journal of Shandong College of Oceanology.15 (1): 146—158

Office of Comprehensive Marine Investigation, Marine Group, Committee of Science and Technology, P. R. China (ed.). (1964)The distribution of dissolved oxygen, phosphate, silicate and Alk in Chinese coast ocean. The national comprehensive investigation report, VI (Sep. 1958-June, 1960), 96

Paerl, H W. (1985)Enhancement of marine primary production by nitrogen enriched acid rain. Nature, 315: 747—

749

Song, J. (1996)Interface Chemistry between sediment and sea water in Chinese coast ocean.. The Ocean Press, Beijing

Treguer P, D M Nelson, A J Van Bennekom, D J DeMaster, A Leynaert, B Queguiner.(1995) The silica balance in the world ocean: A re-estimate. Science, 268: 375—379

Wang, B. G. Wang and F. Liu. (1998a)Distribution features of the Chemical parameters in the Southern Yellow Sea in spring. Marine Environmental Science,17 (3) : 45—50

Wang B., G. Wang, C. Chung and D. Liang. (1998 b) The horizontal distribution and transport of nutrients in the South Yellow Sea. In: 98 Youth marine symposium-proceedings of marine sustainable development. The Ocean Press, Beijing, 170—175

Wang B., G. Wang, C. S. Chung and D. B. Yang. (1999)Distribution features of bioactive elements in seawater in the Southern Yellow Sea in winter. Journal of Oceanography of Huanghai &Bohai Sea Seas, 17 (1) : 40—45

Yu, Z., J. Zhang, Q. Yao and T. Mi. (1999)Nutrients in the Bohai Sea Sea. In: Biogeochemical processes in the Bohai Sea and Yellow Sea, edited by G. H. Hong, J. Zhang and C. S. Chung. The Dongjin Publication Association, Seoul, 11—20

Yuan, Y., B. Guo and X. Sun.(1993) Physical oceanography in Pan-Yellow Sea region. Journal of Oceanography of Huanghai & Bohai Sea Seas, 11 (3) :1—6

Zabel M, A (1998)Dahmke and H D Schulz. Regional distribution of diffusive phosphate and silicate fluxes through the sediment-water interface: the eastern south Atlantic. Deep-Sea Research, I (45): 277—300

Zhang J. (1994) Atmospheric wet deposition of nutrient elements: correlation with harmful biological blooms in Northwest Pacific coastal zones. AMBIO,23 (8): 464—468

Zhang J., W. W. Huang, M. G. Liu and J. Z. Cui. (1994)Eco-social impact and chemical regimes of large Chinese rivers-a short discussion. Water Research, 28: 609—617

Zhang J, (1996)Nutrient elements in large Chinese estuaries. Continental Shelf Research, 16 (8): 1023—1045

Zhang J., Z. G. Yu, S. M. Liu, H. Xu, M. G. Liu. (1997)Dynamics of nutrient elements in three estuaries of North China: the Luanhe, Shuangtaizihe, and Yalujiang. Estuaries, 20 (1): 110—123

Zhang J, Z G Yu, S Z Chen, H Xiong, H T Chen, B Li, Q Z Yao, Q M Wu and J Xu.(1998) Processes affecting nutrient dynamics in the Yalujiang and its estuary (1994—1996), North China. In: Health of the Yellow Sea, edited by G H Hong, J Zhang and B K Park, The Earth Love Publication Association, Seoul.149—189

Zhang J., J. Xu, S. M. Liu, H. Xu, Z. G. Yu and D. Q. Xue.(1999a) Nutrient element distributions in the mesotidal Shuangtaizihe Estuary from North China. Journal of Coastal Research, 15 (2): 526—536

Zhang J, S Z Chen, Z G Yu, C S Wang and Q M Wu.(1999b) Factors influencing changes in rainwater composition from urban versus remote regions of the Yellow Sea. Journal of Geophysical Research,104 (D1): 1631—1644

Zhang W. (1996) Nutrients in the East China Sea and the ecosystem dynamic model of Jiaozhou Bay sediment. Masters thesis,

Zheng J. and J. G. (1998)Quinn. Analytical procedures to classify organic pollutants in natural waters, sediments and benthic organisms. Acta Oceanologica Sinica, 7: 226—236

Zou J., Dong, L. and Qin B. (1985) Preliminary studies on eutrophication and red tide problems in Bohai Sea Bay. Hydrobiologia, 127: 27—30

Regional Geologic Tectonics of the Nansha Sea Area

Jin Qinghuan（金庆焕） Li Tanggen（李唐根）
(*Guangzhou Marine Geological Survey, MLNR, Guangzhou* 510075)

Abstract Based on the data from multi-year comprehensive marine geological-geophysical investigations made in the Nansha sea area, the regional geophysical-field features, deep structures of the crust, basement nature and faulting tectonics are analysed and studied in the paper, and the faulting tectonics are divided into the three systems of normal fault, obduction fault and strike-slip fault, and there are 3 large regional massifs and 6 blocks. The 13 main large and medium-sized Cenozoic sedimentary basins superimposing on the crust of different types and basements or in different tectonic locations are characterized by large sediment thickness, multiple types and large scale, made up of several primary basins and serve as very important places for oil and gas accumulations.

Keywords geologic tectonics; Cenozoic sedimentary basins; geophysical field; Nansha sea area

Located in the south of the South China Sea at 3° 25′ — 12° 10′ N, 108° 15′ — 119° 00′ E, the Nansha Islands and its adjacent sea area are 937km wide from south to north and 1195 km long from east to west, covering an area of $61 \times 10^4 km^2$ within its traditional marine boundary lines and to the south of the deep-sea basin. Within its limits are scattered a total of 186 islands, sandbars, reefs, beeches and shoals which have been named, of which the 11 named islands cover an area of $1.591 km^2$. The island with the largest area of 0.43 km^2 is Taiping Dao and those with an area larger than 0.1 km^2 each also include Zhongye Dao, Xiyue Dao, Nanwei Dao, Nanzi Daoand Beizi Dao, and Hongxiu Dao has the highest elevation of 6.2m. The Nansha sea area is complex in topography and geomorphology, with abyssal plains and wide continental shelves as well as continental slopes on which stand large numbers of islands and reefs, and long and narrow troughs.

1 Geophysical Field Features

1.1 Gravity field features

The spatial gravity anomaly in the Nansha sea area and its adjacent area have an obvious character of zoning and may be divided into 4 anomalous zones (Fig. 1).

(1) Low-value anomalous zone of the northern deep-sea basin with an anomalous value of (0---20) $\times 10^{-5} ms^{-2}$

At Changlong Haitian in the middle of the southwest deep sea basin there is a negative anomaly and it overlaps with the spreading axis of the southwest sea basin, which indicates lesser density of the

crust here and also coincides with the gravity anomaly of the spreading mid-ocean ridge.

(2) Anomalous zone of island and reef change

As the main body of the Nansha sea area, the anomaly trends generally in the NE direction but locally in the NW and near EW directions, with an anomalous value of $(0—29)\times10^{-5}ms^{-2}$. In some places such as Liyue Tan and Yongshu Jiao there exist local gravity highs with an anomalous value of $(60—100)\times10^{-5}ms^{-2}$, from which it may be inferred that there exist high-density ancient blocks. At the juncture of the sea basin and the continental slope, there form two negative anomaly zones on the south and north sides, which is especially conspicuous to the north of Liyue Tan where there are a gravity high on the side of continental slope and an accompanying gravity low on the side of sea basin. Such anomaly is referred to as "gravity marginal effect", which is a common anomalous type due to the different crust-type zones at the continental margin.

Fig. 1 Air gravity anomaly of the Nansha sea area

(3) Negative anomaly zone of the Nansha trough

Situated to the north of North Borneo and Palawan I., the anomaly trends NE with an anomalous value of $(0—40)\times10^{-5}ms^{-2}$, and locally $-60\times10^{-5}ms^{-2}$. Such an anomaly is in keeping with the geological background here. On the south side of the zone there has developed an overthrust nappe obducting northwestwards since the Cenozoic era, which weighs down the crust. In addition, it is also a Cenozoic sedimentary zone of high density materials with a thickness up to over 6km.

(4) Normal anomaly zone of southwest continental shelf

Located in the Indo-China and Sunda continental shelf area in the southwest, the anomaly trends indistinctly, with an anomalous value of $(0—40)\times10^{-5}ms^{-2}$. This zone has Cenozoic sedimentary basins developed but no obvious gravity anomalies except in local sections where there are gravity lows less than $0\times10^{-5}ms^{-2}$. Such an anomalous freature indicates the presence of high-density compositions in the basement structure of the zone.

At the margins and intersection belts of various anomaly zones are scattered cascade zones of spatial gravity anomaly, among which the most distinct ones are those on both sides of the Nansha

trough, and those of the Central and Southwest Basin as well as the contact zone of the Nansha island reef area. These cascade zones may be the manifestations of the large and deep fracture zones in the crust and even the lithosphere. In the Nansha island reef zone, there also exist anomaly zones separating different gravity anomaly types, which trend NW, corresponding to the Balabac and Tingjar faults. The offshore area of Mindoro-Palawan-Northeast Kalimantan is a high-value zone of spatial gravity anomaly, with a general anomalous value of (20—60) $\times 10^{-5}ms^{-2}$ and the maximum of up to $100 \times 10^{-5}ms^{-2}$ in the middle of Palawan I.. Except topographic factors, these anomalies are mainly attributable to the high-density rocks of an ultrabasic mixtite belt formed in the late Jurassic period—early Cretaceous period.

1.2 Magnetic anomaly features

The Nansha sea area lies in the low latitude region with the geomagnetic dip between 10° and -10° and the magnetic equator at about 8° of geographic latitude. Therefore, the magnetic anomalies measured under normal oblique magnetization are mainly negative values, generally 10 — -200nT with accompanying anomalies of -50 — 100nT locally. The anomaly rises from the Zengmu Ansha region in the southwest to the north and northeast, and increases from -100nT in the southwest to 100nT in the south of Liyue Tan in the northeast (Fig. 2).

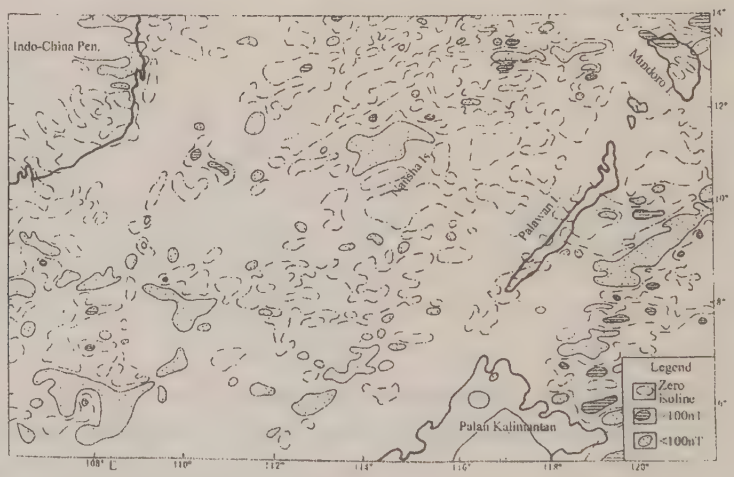

Fig. 2 Isomagnetic line of the Nansha sea area (△T)

The bulk geomagnetic anomaly trends mainly NE and near-EW, locally NW and near-SN. The magnetic anomaly may be divided into five anomaly zones:

(1) High-value anomaly zone in the central north islands and reefs

Located in the central north sea area of Nansha Islands, the anomaly trends NE-NEE with anomalous values varying between -50 and -100nT. Further up 30km around the Yinqing-Zhenghe reefs there is a positive anomaly zone (South China Sea Institute of Oceanology, Academia Sinica, 1996). According to analysis, the magnetic anomaly in this area is mainly an upwelling area of magnetic basement—a manifestation of the ancient metamorphic basement, which was complicated by the magmatite in the middle Cenozoic era.

(2) Magnetic variation anomaly zone on the Indo-China continental shelf

Located on the continental shelf north of 7° , the anomaly trends generally NNE, and locally NW,

with an anomalous value of -50—50nT, and a local anomaly up to -150—50nT on the south side. Around Palau Natuna, there is an anomaly zone of high-value variations with an anomalous value of 200—100nT, which trends near SN. Regional data indicate that the metamorphic basement of the Mesozoic era—late-Paleozoic era was complicated by the moderate acidic magmatic rocks of the Mesozoic era and that the high-value variation magnetic anomaly around Palau Natuna may be a manifestation of the ophiolite suite of the late Mesozonic era.

(3) Zengmu low-value tranquil anomaly zone

Located to the west of Beikang Ansha and to the south of Nanwei Tan and Wan'an Tan, it is a low-value tranquil anomaly zone with the anomaly trending indistinctly and generally with an anomalous value of -50—100nT. The magnetic basement of this zone is buried deep, generally over 6—8 km.

(4) Island-arc magnetic variation anomaly zone

Mainly distributed in Palawan I. and on its southern and northern sides, it is a changeable skipping anomaly zone with an anomalous value of 50—100nT. By inference, it may have been connected with the meso-basic and ultrabasic rocks of the late Mesozoic era.

(5) Deep basin magnetic band anomaly zone

Located in the deep basin on the north side, the zone is demarcated by Zhongnanshan Mountain into the eastern and western parts. The eastern Central Basin magnetic band trends near EW and the western Southwest Basin magnetic band NE.

1.3 Features of geothermal flow field

According to the analysis of the 249 measured data of geothermal flow collected from the Nansha sea area, the geothermal field of the Nansha sea area has the following characteristics:

(1) High-value heat flow field

The heat flow value is (80.8 ± 24.8) mW/m^2 on the average, slightly higher than the mean value (77.4 ± 22.7)mW/m^2 in the South China Sea and second only to that in deep sea basins.

(2) Distinct zonation of heat flow values

This has obvious correlation with the crustal structure and the heat flow values in the sections with thin crust are higher. The areas with higher heat flow values in the Nansha sea area include: the southern Xiya upwarping zone with a heat flow value of 80—130mW/m^2, while the geothermal heat flow values at the southwestern tip of the Nansha Trench are lower, generally 50—70mW/m^2 and only 27mW/m^2 at the lowest[1].

1.4 Seismic surface wave (Vs) tomography and deep-seated structure

By applying the natural seismic surface wave tomography and choosing 55 long-period natural earthquakes of over magnitude 5 recorded by the digital seismic stations of Qiongzhong and Taibei of China, Chiang Mai of Thailand and Lumbang of Indonesia, the Rayleign wave groups are calculated with the method of TEAN-DEF from which the dispersion curves within 10-100s with good resolution ratio are choosen to carry out three-dimensional tomographic inversion and obtain a series of horizontal sections and vertical Vs sections of the surface wave propagating speed at different depths in the South China Sea including the Nansha sea area. It has been found that the upper mantle has distinct layering vertically with respect to the speed (Vs) structure of the Nansha sea area and block features horizontally. Vertically above 30 km is a low-speed layer, within 30—70km, there exists a high-speed

layer with Vs of 4.7 — 4.8km/s, 70 — 100km is the low-speed layer with 4.5km/s (possibly corresponding to asthenosphere) and below 100km the speed gradually increases.

The horizontal blocks of Vs are clearly manifested on the horizontal slices for different depths. Centring around the central north island reef area in the Nansha Island and on the horizontal slices for the depths of 15,30,50 and 90km, this zone is a high-speed zone of Vs while the northwest and southwest parts are a low-speed zone of Vs. By inference, an ancient high-density rigid mass may have existed in the central north of Nansha, which might have been a Proterozoic or older metamorphic mass.

2 Regional Tectonics

2.1 Crustal types and basement structure

2.1.1 Crustal thickness and types of the Nansha sea area

The depth of the Mohorovicic discontinuity of the Nansha sea area and its adjacent region increases from the north sea basins to the island reef zone, i. e., from 9 km to 20—26 km; The Mohorovicic discontinuity of the Nansha trough is 19—22km deep and that near the Sunda continental shelf zone and Palau Natuna, 20—22km[2].

The crust of the Nansha sea area may be divided into three types: continental crust, ocean crust and transitional crust. The continental crust is mainly located in the Indo-China and Sunda continental shelf zone, generally with a crustal thickness of 25—28 km; The ocean crust is mainly found in the northern deep basin zone, generally with a crustal thickness of 5—8km, which has been confirmed on the velocity structure profile of the sonobuoy; the transitional crust is the primary crustal type of the Nansha sea area, generally with a crustal thickness of 18—26 km.

The crustal structure of the northern Zengmu Basin is complicated. According to calculation, the crustal thickness is 18—20 km while the thickness of the Cenozoic epidermis may reach 10—14 km, the maximum thickness up to 16km. Therefore, the consolidated crustal thickness is only 6—8 km. According to the findings of the sonobuoy stations 270V36 and 271V36 to the west of Beikang Ansha, the velocity of 6.7—6.8km/s is found below the depth of 10—11km (Houtz etal, 1984) and this high-speed layer is considered to be the velocity structure of the standard oceanic layer 3. This phenomenon may be attributable to the following: (1) In the course of subduction of the ancient South China Sea, the ancient oceanic crust was retained in local sections due to complex dynamic factors such as the collision and stylolitization of crustal masses; (2) New oceanic crust was formed due to inhomogeneity of infracrustal erosion (emplacement of mantle-derived material).

2.1.2 Basement structure of the Nansha sea area

The basement referred to here includes the Cenozoic sedimentary basement and the magnetic basement. The Cenozoic deposit in the west of the Nansha sea area is immensely thick and the Cenozoic erathems in North Zengmu Wan'an Basin reach 12km and 16km respectively at the thickest, where the Cenozoic sedimentary basement coincides with the magnetic basement. In the island reef zone of the central north of Nansha, (to the east of Nanwei Tan), the Cenozoic deposit is thinner,

Table 1 Main faults and faulting systems of the Nansha sea area

Type	Direction	No.	Name of fault	Order of fault	Remarks
Obduction fault system	NW	(1)	Lupar line	First	Stylolite
	EW	(2)	Mersing line	First	Collision zone
	SN-NE	(3)	Longalan fault	First	
	NE	(4)	Southeast fault of Nansha trough	First	Neosubduction line
	NE	(5)	West Palawan fault	First	
	NW	(6)	Manila Trench fault	First	
Normal fault system	NE	(7)	Northwest fault of Nansha Trough	Second	
	NE	(8)	Meiji fault	Second	
	NW	(9)	Balingian fault	Second	
	NW	(10)	Lanai East fault	Second	
	NE	(11)	South fault of the North col of Wan'an	Second	
	SN	(12)	Kunlun fault	Second	
Strike-ship fault system	NW	(13)	Ulugen fault	First	
	SN	(14)	Zhongnan-Liyue fault	First	
	SN	(15)	West marginal fault of the South China Sea	First	
	SN	(16)	Wan'an fault	First	
	NW	(17)	Tingjar fault	First	
	NW	(18)	Balabac fault	First	
	SN	(19)	Molis fault	Second	
	NW	(20)	Manganu fault	Second	
	NE	(21)	Molu fault	Second	
	NE	(22)	Klavite fault	Second	
	NW	(23)	Mukan fault	Second	
	NW	(24)	Southwest Wanan fault	Second	

generally only 1—3km while in individual areas such as Liyue Basin, the Cenozoic erathem may be as thick as 6km. But it can be seen from the depth chart of magnetic basement that the island reef area in the central east of Nansha is characterized by blocks from east to west and zones from south to north. The blocks from east to west include the west (Yongshu Jiao—Andu Tan) depression, the central (Taiping Dao — west of Balabac I.) rise and the east (to the west of Liyue Tan) depression. The noncoincidence between the Cenozoic sedimentary basement and the magnetic basement in the central-eastern island reef area of Nansha indicates that there may be in this area thick Mesozoic or Paleozoic group deposits underlying the Cenozoic erathem. The zonation from south to north refers to the zonal structure from northwest to southeast with two rises and two depressions, i. e., Yingqing Rise, Nanwei Basin, Andu Rise and Nansha Trough Basin.

2.2 Fault structure

2.2.1 Division of faulting systems

The fault structure is highly developed in the Nansha sea area. According to the statistics of the data available, there are over 180 faults each with a length of over 20 km. In the light of the mechanical properties of the fault, the faults in the Nansha sea area may be divided into three major systems, i. e.,

normal fault, obduction fault and strike-slip fault systems (Table 1) .(See Fig. 4 for the fault numbers and locations in Table 1).

(1) Obduction fault system: It is main located within the Natuna-Borneo-Palawan accreted belt of folded strata and on its both sides or the land mass margin, such as Lupar zone, Sibu zone, southeast margin of Nansha Trough, etc.

The obduction fault on the southwest margin of Nansha Trough is huge in scale and of great importance to the tectonic formation and evolution of the southern Nansha sea area. In plane distribution, it trends mainly NE and near EW, spreading in rows or zones and extending far, and in section, it is plow-shaped with the upper part sharp and the lower part gentle. The second-order fault is largely the decollement of cover, often converging deep into a certain decollement surface and thus forming a series of imbricated obduction assemblages. The first-order fault is the basement involution type (mainly referring to the stylolite). The first and second-order thrust faults tend to become the basin controlling faults such as the southeast margin fault of the Nansha trough, west Palawan fault, etc. (Fig. 3)

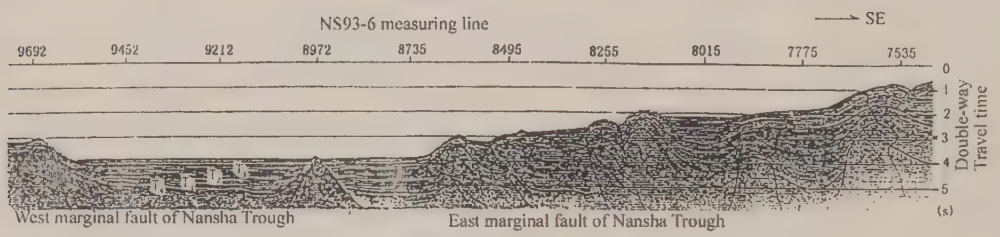

Fig. 3 Seismic section of Sabah near sea—— Nansha Trough area

T_1 ——Q bottom; T_2 ——N_2 bottom; T_3—— N_1^3 bottom; T4—— N_1^2 bottom

(2) Normal fault system:The system is mainly located in the central north of the Nansha sea area with the first- and second-order faults controlling the basin boundary or the upwarped and down-warped units boundary and the third-order fault controlling the local tectonics. Except the northwest fault of the Nansha trough, all the faults are small in scale, extending generally less than 200 km in different directions of dip. In plane, they are mainly in the directions of NE and NW. The NE-trending faults are larger in size and the NW-trending normal faults are primarily scattered on the southwest part of the Zengmu Basin. In addition, there are a small number of SN-trending faults.

(3) Strike-slip fault system: Widely distributed in the whole Nansha sea area, it is composed of mainly the NW- and SN-trending faults, such as Tingjar fault, Wan'an fault, etc and secondly the NE-trending faults such as the ones within the Wanan Basin and Brunei-Sabah Basin.

The faults of this system are large in scale. Extending up to over 500km, the first-order faults not only become the basin controlling faults but also constitute the boundaries between different blocks, such as Tingjar fault, Balabac fault, etc.

2.2.2 Main stages of fault activity

The fault activity is mainly divided into three stages in the Nansha sea area:

(1) First stage (late Cretaceous epoch—Eocene epoch) The faults are mainly distributed in the south and west of the Nansha sea area and represented by Lupar line、Mersing line and the western marginal basin of the South China Sea. Besides, within the basin there are secondary faults accompanying this stage of fault activity.

(2) Second stage (Oligocene epoch—early Miocene epoch). Widely distributed, the faults either inherit the first-stage ones or occur due to the southward movement and under thrust—collision of the Nansha mass along with the spreading of the Central Basin and Southwest Basin of the South China Sea. The representative faults of this stage include Zhongnan—Liyue fault, Wanan fault, Tingjar fault, etc.

(3) Third stage (late Miocene epoch—Quaternary period). The faults are mainly the NE-trending obduction fault zones on the southern edge of the Nansha trough (accompanied by the obduction formation to the northeast of Palau Kalimantan) and the NW-trending obduction fault zone in the Manila Trench, which are vast in scale and wide in its region of influence.

Apart from the fact that the above-mentioned faults are often compatible in mechanical properties, along with the evolution of time, the fault properties may be inverted and the strike-slip direction may change.

2.2.3 Features of tectonic stress field

The faults of different properties and directions as well as their combination relations do not occur voluntarily, but are formed under a given stress system, so they have a unified tectonic stress field.

The southern part of the South China Sea is located where the Eurasian, Pacific and India-Australia plates meet. Analysis of the history of movement of these three major plates indicates that the Eurasian plate has undergone no great change in latitude since 100Ma, but only small clockwise rotations, so it may be regarded as basically stationary. Before 42Ma, the subduction direction of the Pacific plate was NNW, but has changed into NW since 42Ma. In the early Cenozoic era, the Indian and Australian plates subducted northwards successively, but since 32Ma, they have continued to move in the NNE direction as a unified plate. Therefore, during the Cenozoic era, the southern part of the South China Sea was mainly subjected to the compression from the south and its eastern part was also pushed to the NWW, which is the reason why the southern margin of the South China Sea has become the collision and subduction edge and the direction of the collision and subduction zone gradually deviates northwards from west to east, turning from near EW to NE. The near EW trending spreading centres in the Central Basin, Sulu Basin and Sulawesi Basin in the South China Sea and the SN-trending strike-slip fault of the western margin of the South China Sea may be regarded as the product of this SN-trending extrusion stress.

2.3 Division of major land blocks

In regional tectonics, the Nansha sea area belongs to the southeast margin of the Eurasian plate. Synthesizing the above-mentioned geophysical fields, crustal properties and fault features, it may be divided into three major masses and 6 land blocks, namely, from west to east, the Indo-China mass including Kunsong and Zengmu land blocks; Nansha mass including Yongshu-Taiping block, Liyue block, and north Palawan block; Burma-Thailand-Malaysia mass: only Sunda block occurs in this area. They have different basement properties and histories of development, and have the strike-slips as

boundaries between each other. Except the Kunsong block and the Yongshu—Taiping block which are ancient continental blocks, the blocks like the north Palawan block and the Sunda block may be the land masses formed only after the Indo-China — Yenshan movement. There are no crystalline basements of the uniform times in the Nansha sea area. The level of cratonization is very low for most blocks, which were formed in the later times (Fig. 4).

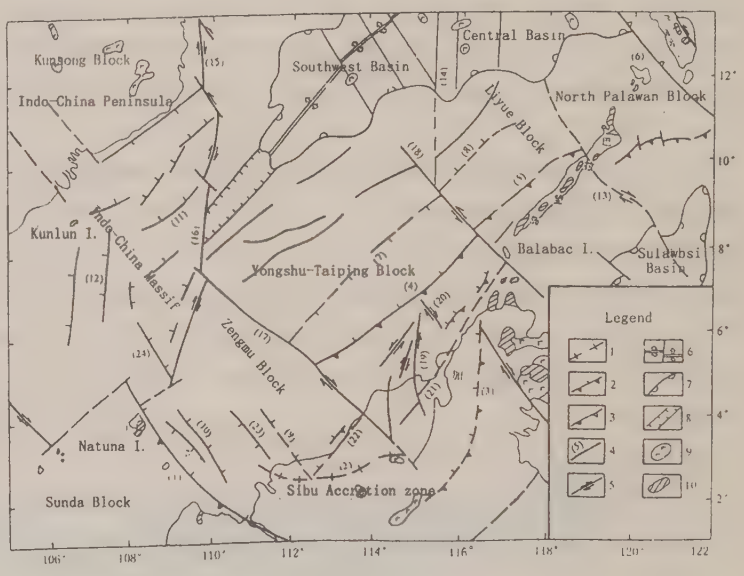

Fig. 4 Division of blocks of Nansha sea area and adjacent regions

1. Collision zone; 2. Obduction zone; 3. Unactive subduction zone; 4. Fault and number; 5. Strike-slip fault zone; 6. Spreading ridge and transform fault; 7. Sea basin boundary; 8. Rife valley; 9. Cenozoic volcanic rock; 10. Mesozoic-Cenozoic ophiolite

3 Distribution and Types of Cenozoic Basin

In the Cenozoic era, there developed a series of sedimentary basins, which, having superimposed on different crustal types and basements or on different locations of different land masses, fall into many and varied basin types.

3.1 Distribution of Cenozoic sedimentary basins

In the Nansha sea area, the Cenozoic deposit is highly developed and distributed all over it except in some seamounts. With an average thickness of over 3 km, the deposit is found mainly in the following sea areas: (1) The western and southern sea areas of Nansha, i. e., the vast sea area west of the line from the northern tip of Palau Kalimantan to the Kim Ranh Bay of Vietnam. This sea area has gigantically thick Cenozoic deposit. The area encircled by a 3 km isopach amounts 40×10^4 km^2, the thickness of sedimentary layer is generally 5— 8 km with a maximum of 15 km. This area includes a series of large- and medium-sized Cenozoic basins. (2) The area ranging from Palawan I. to Liyue Tan with a Cenozoic deposit thickness of 3-8 km. (3) The sea area near the central north island reef zone, where the thickness of sedimentary layer is generally 1—3 km and the basins are small and scattered[4].

In the Nansha sea area, a total of 13 main large- and and medium-sized Cenozoic sedimentary basins may be identified, those of which belonging to the Nansha sea area are: from east to west, North Palawan Basin, West Palawan Basin, Liyue Basin, Brunei-Sabah Basin, Nansha Trough Basin, Beikang Basin, Zengmu Basin, Nanwei Basin and North Wan'an Basin while the Wan'an Basin and

Kunlun Basin, West Natuna Basin and Mekong Basin do not belong to the Nansha sea area (Fig. 5).

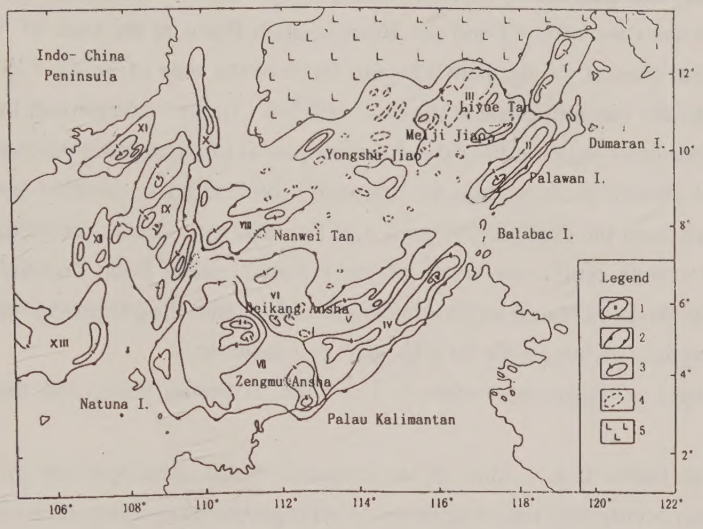

Fig. 5 Distribution of Cenozoic sedimentary basins in the Nansha sea area

1. Cenozoic basins and Nos; 2. Oceanic boundary; 3. Cenozoic isopach line (km); 4. Island reef and shoals; 5. Oceanic crust; Ⅰ. North Palawan Basin; Ⅱ. West Palawan basin; Ⅲ. Liyue Basin; Ⅳ. Brunei— Sabah Basin; Ⅴ. Nansha Trough Basin; Ⅵ. Beikang Basin; Ⅶ. Zengmu Basin; Ⅷ. Nansha Basin; Ⅸ. Wanan Basin; Ⅹ. Wanan Basin; Ⅺ. Mekong Basin; Ⅻ. Kunlun Basin; ⅩⅢ. West Natuna Basin

In the early Cenozoic era, the island reef area of the central north of Nonsha sea area may have been a rise region. In the late Cenozoic era, this area evolved into a local fault depression with a sedimentary layer of 1—3 km thick, but as it is small in area and sedimentary thickness, it was named a basin. It should be noted, however, that the magnetic basement of this area has a buried depth of 3—8 km with a maximum depth of 15km. From this it may be calculated that underlying the Cenozoic group there are often non-magnetic strata with considerable thickness, which may be the Menozoic group and the palaeoid strata.

3.2 Preliminary division of Cenozoic basin types

As some large- and medium-sized sedimentary basins in the Nansha sea area are located in different masses and have undergone different periods of tectonic evolution, they each have different basin prototypes and sedimentary tectonics characteristics. Therefore, principles for dividing the basin types in the following four fields are proposed: (1) the plate tectonics environment or the geotectonic position where the basin lies; (2) crustal type; (3) the geodynamic background and genetic mechanism when the basin prototype is formed; (4) the form of structure and its features in different periods of evolution; According to the principles of basin classification[5] and the definition on basin prototypes, and summing up the basin characteristics and the history of basin formation in the Nansha sea area, the major Cenozoic large-and medium-sized sedimentary basins in this region are preliminarily divided into 6 basin prototypes in 3 categories.

3.2.1 Basin type associated with compression

There are three kinds of compressive-type basin prototypes, i. e., forearc basin (FAB), remnant oceanic-crust basin and peripherial foreland basin (PFB). (1) Forearc basin: for instance, the West Palawan Basin at the time of N_2-Q and the Brunei-Sabah Basin at the time of N_1^2-Q. (2) Ramnent oceanic-crust basin: such as the northern Zengmu Basin at the time of N_1^2-Q. (3) Peripheral foreland basin: for example, the Zengmu Basin at the time of E_2^3-N_1^1. In the same period, there often developed the ramnent oceanic-crust basin on the side of the peripheral foreland basin while the ramnent oceanic-crust basin would ultimately evolve into the peripheral foreland basin. In other words, the time before collision may have been the evolutionary period of the ramment oceanic-crust basin; With the raising of the degree of stylolitization, the scope of the ramment ocean basin diminished and that of the peripheral foreland basin increased so that finally all evolved into the peripheral foreland basin.

3.2.2 Basin prototype associated with the pull-apart environment

Here two types of basin are involved, i. e., the extension basin and the intracratonic fault depression basin.

(1) Extension basin: It is a kind of intracratonic basins developed on the basis of the early extension and often occurs with the semigraben or horst graben alternating, such as the Wanan Basin in the early and middle Eocene epoch. (2) Intracratonic fault depression basin: It is a kind of intracratonic basins developed on the basis of the early extension. The lower part of the basin is a dustpan-shaped fault depression and the central-upper part is a depression. This kind of basins are widely distributed in the northern area of the Nansha sea area block, such as Liyue Basin, North Palawan Basin, etc.

3.2.3 Basin prototype associated with the strike-slip

This kind of basins are those formed by the two masses along the strike-slip fault or the pull-apart in the early stage or the strike-slip pull-apart in the later stage, i. e., the shear pull-apart basin. This kind of basins generally have a two-layer structure of fault and depression with rift structure developed in the early stage and folded flexure developed well in the late stage, such as Wan'an Basin (E_3-Q).

References

1 Zeng Weijun, Upper Mantle Activities and Indo-China Mantle Plume in the South China Sea Area, South China Sea Geological Research (9). Wuhan; China University of Geology Press, 1997

2 Xu Dongyu, Li Xiqing, Zhang Xunhua, Li Tanggen and Chen Bangyan, China Offshore Geology, Beijing, Geological Publishing House, 1997

3 Jin Qinghuan, South China Sea Geology, and Oil and Gas Resources, Beijing: Geological Publishing House, 1989

4 Fontaine H. et al, The Jurassic in Southeast Asia. CCOP Tech Bull., 1983, 16

5 Zhang Yuchang, Analysis of China's Oil- and Gas-Bearing Basin Prototypes, Nanjing, Nanjing University Press, 1997

6 Xia Kanyuan, Geology, Geophysics, and Oil and Gas Resources in the Nansha Islands and Their Ajacent Sea Areas, Beijing: Science Press, 1996

7 Bai Zhilin and Zeng Xianghui, Special Volume on the Comprehensive Research of Geology and Geophysics in the Southeast of the Nansha Sea Area, Wuhan: China University of Geology Press, 1996

Marine Science Bulletin

Marine Science Bulletin publishes papers on marine science and technology including physical oceanography, chemical oceanography, marine biology, marine geology, environmental oceanography, estuarine & coastal sciences, marine technology, digital ocean, coastal zone management, ocean engineering, marine economics, etc., and aims to promote international academic exchange.

Editor-in-Chief: Hou Wenfeng (侯文峰)
Deputy Editor-in-Chief: Lin Baofa (林宝法) Yang Ying (杨 鹰)
Executive Editor: Zhou Hongjun (周洪军) Lu Mingsheng (卢明生)

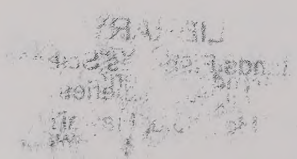

Marine Science Bulletin (Vol.2 No.2 October 2000)

Responsible Institution:
State Oceanic Administration of China
Edited and Published Semi-annually by:
National Marine Data and Information Service
Address: 93 Liuwei Road, Hedong District, Tianjin 300171, China
E-mail: hytb@mail.nmdis.gov.cn

ISSN1000-9620
CN12-1271/N
Price: $30.00 per year